COMPUTER SIMULATIONS OF THE STATISTICAL BEHAVIOUR OF ACTIVE PARTICLES

Dissertation

zur Erlangung des Grades
„Doktor der Naturwissenschaften“
am Fachbereich Physik, Mathematik und Informatik
der Johannes Gutenberg-Universität Mainz

vorgelegt von
Benjamin Trefz

JOHANNES GUTENBERG
UNIVERSITÄT MAINZ

Dedicated to my wife Manuela,
and my parents Andrea & Dieter.

ABSTRACT

We introduce a new model of activity to study the structural and dynamical properties of mixtures of active and passive particles with molecular dynamics simulations. The limit of no activity corresponds to the passive continuous Asakura-Oosawa model. This model, which has an entropy-driven phase separation, consists of two particle types: colloids and polymers. In this thesis the colloids are made self-propelled by introducing an active force, which acts in the direction of mean velocity of the surrounding colloids, similar to the well-known Vicsek model. The addition of activity is shown to facilitate phase separation. Different thermostats are applied to study their influence on the active non-equilibrium system. Using an integral equation theory approach, a mapping of the active onto a passive model is performed. The resulting potential is studied via molecular dynamics simulations and facilitates phase separation as well.

The active model exhibits a second order phase transition from a disordered phase to an ordered state in which most of the colloids align. We apply the subbox method to determine the critical point of the system from simulations in the canonical ensemble, using an order parameter that depends on fluctuations of the particle number. This approach is shown to work with an equilibrium model. Extensive simulations are performed to determine the critical point of the active model. This is done by assuming initially that the law of rectilinear diameter still applies in a non-equilibrium system. The first determination of the critical point is then improved iteratively. The critical point of our active system with an active force $f_A = 10$ is $\eta_{col}^{crit} = 0.103(4)$ and $\eta_{pol}^{crit} = 0.264(10)$. We show that the law of rectilinear diameter is not followed close to the critical point and provide a simulation approach to account for this. An explanation of how the activity could influence the position of the critical point is given by using an order parameter known from the Vicsek model.

With the knowledge of the critical point two critical exponents of the active system are calculated. From the phase diagram we determine the critical exponent of the magnetisation $\beta = 0.30(3)$, which is in good agreement with the 3D Ising universality of the underlying passive system. However, the critical exponent of the correlation length $\nu = 0.82$ differs somewhat from the corresponding exponent in the 3D Ising universality class.

ZUSAMMENFASSUNG

Ein neues Modell für Aktivität wird eingeführt, um mit Hilfe von Molekulardynamik-Simulationen deren Einfluss auf Struktur und Dynamik einer Mischung von aktiven und passiven Teilchen zu untersuchen. Der Grenzfall keiner Aktivität entspricht dem passiven kontinuierlichen Asakura-Oosawa-Modell. Dieses Modell besteht aus zwei Teilchensorten: Kolloiden und Polymeren und kann, bedingt durch entropische Entmischung, in zwei Phasen separieren. In dieser Arbeit werden die Kolloide mit einer aktiven Kraft, welche in Richtung der durchschnittlichen Geschwindigkeit benachbarter Kolloide zeigt und vergleichbar mit dem Vicsek-Modell ist, versehen. Dies erleichtert die Phasentrennung der Mischung. Verschiedene Thermostate werden verwendet und deren Einfluss auf das aktive Modell untersucht. Das aktive Modell wird durch einen Integralgleichungsansatz auf ein passives abgebildet, welches mit Molekulardynamik-Simulationen untersucht wird und ebenfalls die Phasentrennung erleichtert.

Das aktive Modell hat einen Phasenübergang zweiter Ordnung von einer homogenen Mischung zu zwei separierten Phasen, wobei sich die Kolloide dann überwiegend in dieselbe Richtung bewegen. Um den kritischen Punkt eines Systems im kanonischen Ensemble zu bestimmen, das einen von der Teilchenzahlfluktuation abhängigen Ordnungsparameter hat, wird die Unterboxmethode verwendet. Es wird gezeigt, dass diese Methode für ein Modell im Gleichgewicht funktioniert. Um den kritischen Punkt des aktiven Systems zu bestimmen, werden umfangreiche Simulation durchgeführt. Dazu wird zunächst angenommen, dass das Nichtgleichgewichtssystem dem Gesetz des geradlinigen Durchmessers folgt. Der somit bestimmte kritische Punkt wird anschließend iterativ verbessert. Der kritische Punkt des aktiven Systems mit einer aktiven Kraft von $f_A = 10$ ist gegeben durch $\eta_{col}^{crit} = 0.103(4)$ und $\eta_{pol}^{crit} = 0.264(10)$. Es wird gezeigt, dass das System nahe dem kritischen Punkt dem Gesetz des geradlinigen Durchmessers nicht folgt. Außerdem wird eine mögliche Erklärung gegeben, wie die Aktivität die Position des kritischen Punktes beeinflusst. Dazu wird der Ordnungsparameter des Vicsek-Modells verwendet.

Mit Hilfe des kritischen Punktes werden zwei kritische Exponenten des aktiven Systems berechnet. Der kritische Exponent der Magnetisierung $\beta = 0.30(3)$ wird aus dem Phasendiagramm bestimmt und stimmt mit dem Exponenten aus der 3D-Ising-Universalitätsklasse des zugrunde liegenden passiven Modells überein. Der kritische Exponent der Korrelationslänge $\nu = 0.82$ unterscheidet sich allerdings etwas von dieser Universalitätsklasse.

PUBLICATIONS

During my time as a Ph.D. student we wrote the following publications:

[1] B. Trefz, J. Siebert, and P.Virnau, "How molecular knots can pass through each other", Proceedings of the National Academy of Sciences **111**, 7948 (2014).

[2] S. K. Das, S. A. Egorov, B. Trefz, P. Virnau, K. Binder, "Phase Behavior of Active Swimmers in Depletants: Molecular Dynamics and Integral Equation Theory", Phys. Rev. Lett. **112**, 198301 (2014).

[3] B. Trefz, and P. Virnau, "Scaling behavior of topologically constrained polymer rings in a melt", Journal of Physics: Condensed Matter **27**, 354110 (2015).

[4] B. Trefz, S. K. Das, S. A. Egorov, P. Virnau, K. Binder, "Activity mediated phase separation: Can we understand phase behavior of the nonequilibrium problem from an equilibrium approach?", The Journal of Chemical Physics **144**, 144902 (2016).

Some of the ideas and data from [2] and [4] will be reiterated here.

CONTENTS

ACRONYMS

ABP active Brownian particle

AO Asakura-Oosawa model

CAO continuous Asakura-Oosawa model

DPD dissipative particle dynamics thermostat

HNC Hypernetted-chain

HWHM half-width half-maximum

IBI Iterative Boltzmann inversion

IET integral equation theory

MBS Maxwell-Boltzmann thermostat

MC Monte Carlo simulation

MD molecular dynamics simulation

MPCD multi-particle collision dynamic

MSD mean square displacement

μVT grand canonical ensemble

NVE microcanonical ensemble

NVT canonical ensemble

OZ Ornstein-Zernike

PBC periodic boundary condition

PY Percus-Yevick

VV Velocity Verlet

WCA Weeks-Chandler-Andersen potential

1 INTRODUCTION

"The goal of statistical mechanics is to elucidate physical phenomena occurring on the macroscopic scale as a result of the interactions among microscopic constituents" [5]. With this description it becomes directly clear why computer simulations are an important tool in statistical mechanics as they allow direct access to the microscopic properties of the particles and their surroundings. By setting these quantities and measuring macroscopic observables one can gain insight as to how the system is affected by the underlying potentials and properties. It is this flexibility, combined with increasing computer capabilities and sophisticated algorithms, that has established computer simulations as an important field of research bridging and supplementing experiments and theory.

Macroscopic systems can undergo remarkable transformations by changing from one phase into another, which has fascinated scientist for centuries [6]. Beside the classic phases: solid, liquid and gas, many more have been reported, like superconductivity, superfluidity, magnetic ordering, cosmological quark confinement, helix-coiling of proteins and many more [7]. Phase transitions can have a significant impact on physical properties of the system. For example one can swim in water, however the same technique is of no use in ice or vapour. With the knowledge of the phase diagram of specific materials new applications for materials can be discovered and novel techniques can be created. The magnetic resonance imaging (MRI) used in hospitals, for example, needs superconductive magnets to reach the necessary magnetic fields. The principle of phase transitions has since been applied not only to physical systems but is used in other fields, e. g. economic and social systems [8, 9], as well.

When systems such as flock of birds [10], or school of fish [11] are studied, the observed collective motion resulting from the combined motion of the individual animals is reminiscent of phase separation seen in passive equilibrium systems. These systems, where the 3D position has to be reconstructed from images, are difficult to modify and rely on observation of huge flocks or schools. It is, however, possible to create systems artificially, e. g. colloidal rollers [12], which become self-propelled due to Quincke rotation [13] in an external electric field. All of these systems have in common that they are out of equilibrium and their constituents can thus be collectively called: "Active particles".

Active particles are intrinsically non-equilibrium systems which have some means of self-propulsion. This can be a motor or flagellum, but can also be induced from the outside, e. g. via vibrations [14, 15] or light [16]. In all cases some form of energy is converted into kinetic energy that results in the self-propulsion. This general definition leads to a large variety of systems on different scales, that are considered active. Beside the rather big animal systems already mentioned, active particles can also be found on a micrometer scale. Such systems include actin filaments [17], and microtubules [18] that are moved by motor proteins in a plane and can be observed via microscopes. Some bacteria are able to propel themselves and can show a density dependent phase separation [19, 20]. It is even possible to alter microorganisms and make them thereby active, e. g. by attaching an artificial, magnetically activated flagellum [21].

In soft matter systems colloids play an important role as a model system since they provide an ideal environment to compare experiment, computer simulation, and theory. For active particles this is no exception and a variety of self-propelled systems have been studied. Colloidal systems that are driven from the outside, e. g. by shining light on the solution, allow for direct comparison of the active and the passive system [22–24]. Another approach is to provide the fuel necessary for the self-propulsion in the solution [25–27]. In these examples the solution contains hydrogen peroxide and the active constituents are so-called Janus-type particles, where one hemisphere is coated with platinum. The conducting hemisphere acts as catalyst for the reaction of hydrogen peroxide to water and oxygen and thus "consumes" the fuel, which in turn propels the particle forward.

There are different ways to model active particles. One of the first models is the so-called Vicsek model [28]. Here, a point-like particle travels at a constant velocity and interacts with other constituents only by adjusting its direction of movement to match the orientation of the mean velocity of neighbouring particles. This 2D model shows an order-disorder phase transition, depending on the average error with which the particles choose their new direction. Another way to model active particles are active Brownian particles (ABPs). Here the constituents have volume exclusion and their direction of self-propulsion diffuses rotationally [29]. The phase separation in this model can be explained by self-trapping of the particles [30, 31]. This generally happens when the rate of accumulating new constituents at the formed cluster is higher than the rotational diffusion of the swimming direction. One can also use inelastic collisions in order to generate active particles, when the energy loss of the collisions is compensated by having the particles self-propel until they exceed a predeter-

mined maximal velocity [32]. All of these systems have in common, that they introduce a phase separation. This phase transition is consequently referred to as motility-induced phase separation (MIPS) [33].

It is clear that these active systems are different from the passive equilibrium systems that are usually studied in statistical mechanics. Therefore, care has to be taken when methodologies from statistical mechanics are applied to active particles [34, 35]. However, the similarity of the phase behaviour is apparent as well. For this reason we are going to study the differences and similarities of a classical equilibrium system and an active counterpart in this thesis. To do so, we will reiterate the basic idea of statistical mechanics, the applied algorithms and the theory of phase transitions in Chapter 2. Instead of directly using an active model we will first discuss a passive model that already contains a phase transition in Chapter 3. In Chapter 4 the passive model from before is extended by a term that is related to the Vicsek model [28]. The active model will include the passive model in the limit of low activity. Therefore it is ensured that the active model, at least for small activities, will also feature a phase transition. After studying the active model we attempt a mapping onto a passive model using integral equation theory in Chapter 5. In Chapter 6 we discuss how the critical point of a test system in equilibrium can be determined. For this we review an already existing technique to analyse a canonical simulation when fluctuations in the particle number are the driving effect for the phase separation. We extend this technique by methods used in grand canonical simulations. In Chapter 7 we apply the discussed procedures to the active model from Chapter 4 and determine the critical point. With the critical point we calculate two critical exponents of the active system in Chapter 8 and compare them with the exponents found for the passive model. Chapter 9 summarises the results obtained in this thesis and provides an outlook for future work.

2 THEORY

2.1 STATISTICAL MECHANICS

2.1.1 Definitions and averaging

The idea of computer simulations of soft matter is to study many-particle systems. In such a simulation the user has access to the velocities and positions of all particles. From this information properties and thermodynamic variables can be computed. There are two approaches to this task: ensemble averaging typically used in Monte Carlo (MC) simulations and time averaging typically used in MD simulations. Both methods follow a similar line of thought which is illustrated in the following. Analogously to Frenkel and Smit in [36] we start with a quantum mechanical system. We have an Hamiltonian H that describes the system. For every energy eigenstate the relation $H|i\rangle = E_i|i\rangle$, where E_i is the energy of state $|i\rangle$, holds. Systems of interest have typically many degrees of freedom (e. g. $O(10^{23})$). As a consequence, many different states will have the same energy. Therefore, the quantity $\Omega(E, V, N)$ is introduced to count the degeneracy of states with the same energy E of a system with N particles in the volume V. At this point we assume that each of the states in $\Omega(E)$ has the same probability to be found. Now we want to find the probability that a system A is in one specific state $|i\rangle$ with energy E_i for a system in thermodynamic equilibrium with a bath system B. System B has to have an energy $E_B = E - E_i$ with the degeneracy $\Omega_B(E - E_i)$, so that the probability to find system A in this state is given by

$$P_i = \frac{\Omega_B(E - E_i)}{\sum_j \Omega_B(E - E_j)} \quad . \tag{2.1}$$

If the internal energy of the bath is much larger than in A we can compute the Taylor expansion of $\ln \Omega_B(E - E_i)$ around E.

$$\ln \Omega_B(E - E_i) = \ln \Omega_B(E) - E_i \frac{\partial \ln \Omega_B(E)}{\partial E} + O(E_i^2) \tag{2.2}$$

We define

$$\beta(E, N, V) = \left(\frac{\partial \ln \Omega_B(E)}{\partial E}\right)_{N,V} = \frac{1}{k_B T} \tag{2.3}$$

and insert Equations 2.2 and 2.3 in Equation 2.1 which gives us the probability to find system A in state $|i\rangle$ with energy E_i in thermodynamic equilibrium

$$P_i = \frac{\exp\left(-E_i/k_B T\right)}{\sum_j \exp\left(-E_j/k_B T\right)} \quad . \tag{2.4}$$

Note, that the denominator of Equation 2.4 is often referred to as partition function Z

$$Z = \sum_j \exp\left(-E_j/k_B T\right) \quad , \tag{2.5}$$

which is the sum over all states and serves as a normalisation, so that the probability to find the system in any state is equal to one. The partition function is closely related to the Helmholtz free energy F

$$F = -k_B T \ln Z \quad . \tag{2.6}$$

We can now compute the thermal average of an observable A

$$\langle A \rangle = \frac{\sum_i \exp\left(-E_i/k_B T\right) \langle i|A|i\rangle}{\sum_j \exp\left(-E_j/k_B T\right)} \quad , \tag{2.7}$$

where $\langle i|A|i\rangle$ is the expectation value of A in state $|i\rangle$. Since we are interested in finding the statistical average in classical systems, we change the summation of all states in Equation 2.5 to an integration over all coordinates and momenta and get the classical partition function for a system with N indistinguishable particles

$$Z_{\text{classical}} = \frac{1}{h^{3N} N!} \cdot \int d\mathbf{p}^N d\mathbf{r}^N \exp\left\{-\beta H(\mathbf{r}^N, \mathbf{p}^N)\right\} \quad . \tag{2.8}$$

Therefore we can determine the average of any observable in the classical limit of Equation 2.7 as

$$\langle A \rangle = \frac{\int d\mathbf{p}^N d\mathbf{r}^N \exp\left\{-\beta H(\mathbf{r}^N, \mathbf{p}^N)\right\} A(\mathbf{r}^N, \mathbf{p}^N)}{\int d\mathbf{p}^N d\mathbf{r}^N \exp\{-\beta H(\mathbf{r}^N, \mathbf{p}^N)\}} \quad , \tag{2.9}$$

which gives us the thermodynamic average of the observable A dependent only on the positions $\mathbf{r}$ and momenta $\mathbf{p}$.

2.1.2 Ergodicity

The average presented in Equation 2.7 and Equation 2.9 is the so-called ensemble average. A variant of it is typically used in MC simulations. In an experiment however, this way of averaging is often not accessible. Instead a time evolution

of the averaging quantity is observed. The same idea is also used in MD simulations, where the equations of motion are solved for each particle. The resulting average is thus

$$\overline{A} = \lim_{t\to\infty} \frac{1}{t} \int_0^t dt' A(\mathbf{r}, \mathbf{p}; t') \quad . \tag{2.10}$$

The idea on which statistical physics is based is the so-called "ergodic hypothesis" which states that both methods of averaging yield the same result

$$\overline{A} = \langle A \rangle \quad . \tag{2.11}$$

2.2 ALGORITHMS

In classical MD simulations the goal is to solve Newtons equations of motion. On a computer, only discrete time steps are available. The numerical integration will therefore need a certain level of approximation. The smaller the time step of the integration the better the approximation will be, however, a computer has a finite numerical resolution, meaning that for too small time steps, numerical errors will occur. Depending on the problem in question different algorithms are available. Two of the most common algorithms to study classical soft matter systems are depicted in the following.

2.2.1 Euler algorithm

The Taylor expansion of the position $\vec{r}(t + \Delta t) \equiv r(t + \Delta t)$ around $\Delta t = 0$ is defined as follows:

$$r(t + \Delta t) = r(t) + v(t)\Delta t + \frac{F(t)}{2m}\Delta t^2 + \frac{\Delta t^3}{3!}\dddot{r}(t) + O(\Delta t^4) \quad . \tag{2.12}$$

If we cut this expansion after the Δt^2 term we get the so-called Euler algorithm. The error of this algorithm is therefore of the order $O(\Delta t^3)$. As one can imagine this algorithm is easy to implement and rather fast. On the downside the scheme is not reversible, that means if we replace the velocities $\vec{v}_i(t)$ with $-\vec{v}_i(t)$ we do not trace the trajectory back even with perfect numerical stability. Since Newtons equations of motion are reversible, it is desirable to have the same for the integration scheme as well. Additionally, the Euler algorithm does not preserve the area in phase space which a normal Hamiltonian would and it can have a long term energy drift. Therefore this algorithm is never used for microcanonical (NVE) simulations and for NVT simulations it is most of the time replaced by the more common Velocity Verlet algorithm. We will use the Euler algorithm when discussing active Brownian particles (ABPs) in Section 4.6.

2.2.2 Velocity Verlet algorithm

We start once again with the Taylor expansion of the position $\vec{r}(t+\Delta t) \equiv r(t+\Delta t)$ as in Equation 2.12 and neglect terms of order $O(\Delta t^3)$ and higher. However, we change the integration scheme to a half time step process consisting of four steps:

1. Calculate the intermediate velocity

$$v\left(t+\frac{1}{2}\Delta t\right) = v(t) + \frac{1}{2m}F(t)\Delta t \tag{2.13}$$

2. Calculate the new positions from the intermediate velocities

$$x(t+\Delta t) = x(t) + v\left(t+\frac{1}{2}\Delta t\right)\Delta t \tag{2.14}$$

3. Calculate the new forces from the new positions

$$F(t+\Delta t) = -\nabla U(x(t+\Delta t)) \tag{2.15}$$

4. Calculate the new velocities

$$v(t+\Delta t) = v\left(t+\frac{1}{2}\Delta t\right) + \frac{1}{2m}F(t+\Delta t)\Delta t \tag{2.16}$$

Since we can insert Equation 2.13 into Equations 2.14 and 2.16 we can eliminate the half time step and thus calculate the new positions and update the velocities as

$$r(t+\Delta t) = r(t) + v(t)\Delta t + \frac{F(t)}{2m}\Delta t^2 \tag{2.17}$$

$$v(t+\Delta t) = v(t) + \frac{F(t)+F(t+\Delta t)}{2m}\Delta t \quad , \tag{2.18}$$

where $F(t+\Delta t)$ are the new forces calculated with the new positions before the velocities are updated. Computationally this algorithm is as fast as the Euler algorithm, since the new forces $F(t+\Delta t)$ can be reused in the next update step as the old forces, thus only the memory usage is a bit higher.

It can be shown that the local error in the position is now $O(\Delta t^4)$ which means the Velocity Verlet algorithm is more exact than the Euler algorithm from before. More importantly, this algorithm is reversible and preserves the area of the phase space. While the true Hamiltonian cannot be simulated, a so-called "shadow-" or "pseudo-" Hamiltonian is followed, which converges to the true Hamiltonian in the limit of infinitely small time steps.

2.2.3 Periodic boundary conditions

In the algorithms discussed above the forces between all particles are taken into account. A computer can handle only a finite number of particles which at the time is way lower than in a typical experiment ($\ll O(10^{23})$). In order to not

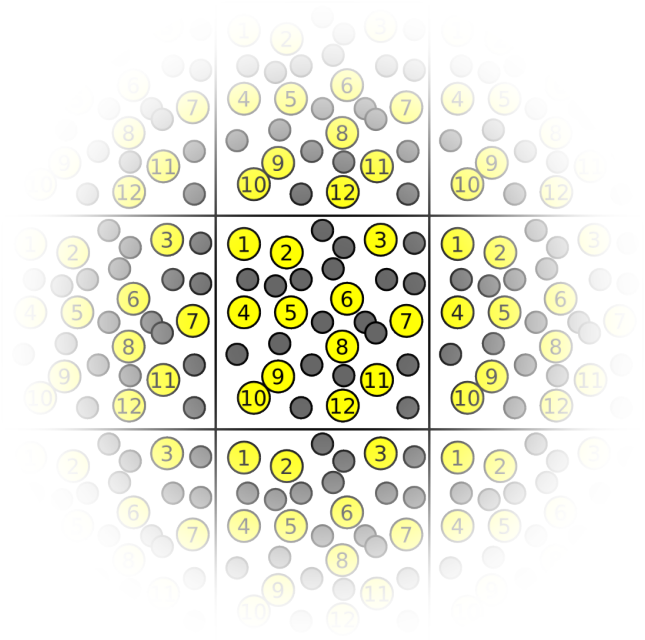

Figure 2.1: Visualisation of the applied periodic boundary condition in two dimensions. The simulation box is shown in the middle and is surrounded by image cells.

only simulate surface effects, we apply periodic boundary conditions (PBC). This means we create image simulation boxes all around the original box and let the particles interact with their neighbours. A two dimensional sketch of these image cells is shown in Figure 2.1. This technique is typically applied when the forces have a certain cut-off radius and thus the interaction of a particle with its own image can be avoided by choosing the size of the simulation box accordingly.

2.3 PHASE TRANSITIONS

2.3.1 Order parameter

For a phase transition we can typically define a parameter that is zero in the less or non ordered phase and non-zero in the other. A liquid-gas phase transition is described by the difference between the density of the liquid and the gas phase

$$m = \rho_{liquid} - \rho_{gas} \quad . \tag{2.19}$$

For an Ising ferromagnet the order parameter is the spontaneous magnetisation

$$m = \frac{\sum_i \sigma_i}{\sum_i |\sigma_i|} \quad , \tag{2.20}$$

where $\sigma_i = \pm 1$ represents a spin on a lattice.

2.3.2 Ehrenfest classification

Phase transitions are classified according to Ehrenfest by the first derivative of the free energy as a function of other thermodynamic variables that diverges. An example for a first order transition is the freezing of liquid water. While freezing one has to cool the system without changing the temperature thereof (latent heat), resulting in a discontinuity in the internal energy. An example for a second order phase transition is the gas-liquid phase transition at the critical point. If we derive the free energy by the temperature the resulting entropy is still continuous, however the entropy derived by the temperature resulting in the heat capacity is discontinuous. Thus the phase transition is of second order.

$$c_v = T \left(\frac{\partial S}{\partial T} \right)_V = -T \left(\frac{\partial^2 F}{\partial T^2} \right)_{N,V} \tag{2.21}$$

2.3.3 Phase diagrams

Phase transitions can occur if one of several different thermodynamic variables is varied. Therefore, we can use the dependence of those variables with each other to extract a “functional” dependence. Such a plot is called a phase diagram. In Figure 2.2 two representations of the water phase diagram are shown, the well known temperature-pressure and the density-temperature diagram. In this sketch the lines are first order transitions between the respective phases. A special point in this diagram is the critical point in which the liquid-gas coexistence line ends. At this point a second order phase transition occurs.

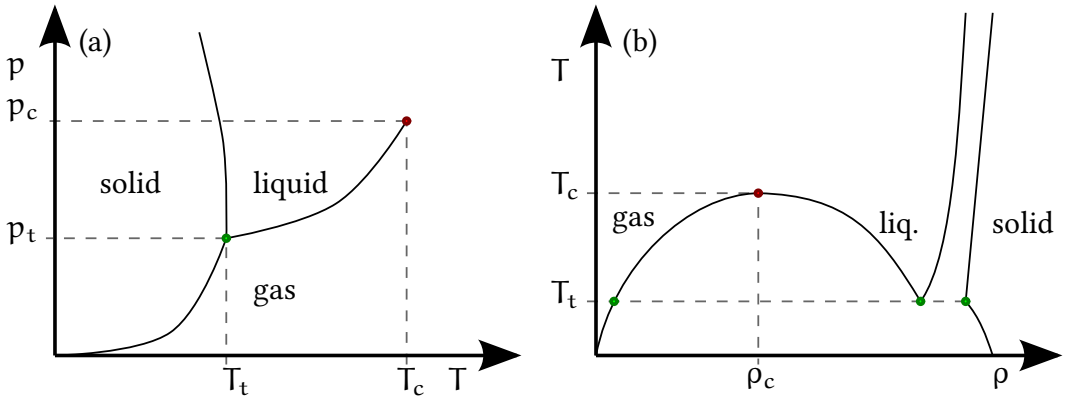

Figure 2.2: Sketch of two phase diagrams for water. (a) The classical temperature-pressure phase diagram and (b) the density-temperature phase diagram. In both graphs the triple point (t) (green) and the critical point (c) (red) are shown.

Predicting the phase diagram from the microscopic interactions is an important task of statistical mechanics [37]. While the system of water is very complex, we can construct model systems with much simpler phase diagrams. The most common example is the Ising ferromagnet with the Hamiltonian

$$H = -J_{nn} \sum_{nn} \sigma_i \sigma_j - h \sum \sigma_i \quad . \tag{2.22}$$

Where $J_{nn} > 0$ is the interaction constant between neighbouring spins σ, and h is an external field. If h is changed at a constant temperature $T < T_c$ a first order phase transition can be observed at $h = 0$, where all spins change their orientation. For $h = 0$ the system has a second order phase transition at $T = T_c$ from a paramagnetic to a ferromagnetic phase.

2.3.4 Universality

In the phase separated state the thermodynamic properties can be written in terms of a power law of the driving variable for the phase separation. For the Ising system this is a function of the temperature. The relations are then as follows [6]:

$$M = M_0 \varepsilon^{\beta} \quad , \tag{2.23}$$

$$\chi = \chi_0 \varepsilon^{-\gamma} \quad , \tag{2.24}$$

$$C = C_0 \varepsilon^{-\alpha} \quad , \tag{2.25}$$

$$\xi = \xi_0 \varepsilon^{-\nu} \quad , \tag{2.26}$$

with $\varepsilon = \frac{T_c - T}{T_c}$. M is the magnetisation, χ the susceptibility, C the specific heat, and ξ the correlation length. α, β, γ, and ν are the critical exponents of the

system. These relations are only valid for $\varepsilon \to 0$. In the 2D Ising model the values can be calculated analytically [38]. For the 3D Ising model no analytic solution has been found yet, but the exponents have been determined to high accuracy with computer simulations [39]. Higher dimensions have a mean field character [37]. In Table 2.1 the critical exponents of the Ising system are shown for different dimensionality. Systems with the same critical exponents belong to

Ising exponents	$d = 2$	$d = 3$	$d = 4$
α	0	0.11	0
β	$\frac{1}{8}$	0.33	$\frac{1}{2}$
γ	$\frac{7}{4}$	1.24	1
ν	1	0.63	$\frac{1}{2}$

Table 2.1: Critical exponents of the Ising model in various dimensions. Note, that the upper critical dimension of the Ising model is $d = 4$. All higher dimension will have the same exponents as those are a result of a mean field theory.

the same universality class [40].

2.3.5 Finite size scaling

Near the critical point the correlation length ξ diverges as indicated in Equation 2.26. In a finite system the maximum correlation length that can be reached is limited by the linear dimension L of the finite-size system, thus for $\xi \to L$ it makes sense to define a scaling variable x as

$$\begin{aligned} & \xi \propto L \overset{2.26}{\propto} \varepsilon^{-\nu} \\ \iff \quad & \varepsilon \propto L^{-\frac{1}{\nu}} \\ \implies \quad & x := \varepsilon L^{1/\nu} \quad . \end{aligned} \tag{2.27}$$

We can rescale Equation 2.23 to $M = M_0(x)L^{-\beta/\nu}$. At the critical point $x = 0$, the scaling function becomes a constant $M_0(0) = \text{const}$ which is no longer system size dependent. This means that if we calculate e. g. the magnetisation as a function of temperature for various system sizes, we could collapse all curves onto a master curve by rescaling the axes to $\varepsilon \to L^{1/\nu}\varepsilon$ and $M \to ML^{\beta/\nu}$. For small x all data would approach a constant, which is an estimate for $M_0(0)$ [37]. However, this makes the proper determination of the critical point rather tedious, as one has to precisely know the critical exponents and simulate close to the critical point from both directions.

A similar approach is to use higher moments of the order parameter. The Binder cumulant is defined as

$$U_4 = \frac{\langle m^4 \rangle}{\langle m^2 \rangle^2} \quad . \tag{2.28}$$

For the Ising model without external field the order parameter is the magnetisation, and we thus get

$$U_4 = \frac{\langle M_0^4(x) L^{-4\beta/\nu} \rangle}{\langle M_0^2(x) L^{-2\beta/\nu} \rangle^2} = \frac{\langle M_0^4(x) \rangle}{\langle M_0^2(x) \rangle^2} \quad , \tag{2.29}$$

which means that the cumulant is independent of the system size at the critical point. Far away of the critical point the value of the cumulant depends on the system size, however for reasonable big systems we can determine the limit of the cumulant. For the non-ordered phase the order parameter goes to zero because of its definition, therefore we divide the fourth moment of a zero mean Gaussian distribution $\left(3\sigma^4\right)$ by the second moment squared $\left((\sigma^2)^2\right)$. In the ordered phase we get a bimodal distribution of the order parameter. If the system is big enough and we are far enough away from the critical point, both peaks will be fully separated and sharply peaked [41]. This means that both moments tend to the same value. To summarise, for $L \to \infty$ we get

$$U_4 \to \begin{cases} 3 & \text{in the non-ordered phase} \quad \text{e.g.} \quad T > T_c \\ 1 & \text{in the ordered phase} \quad \text{e.g.} \quad T < T_c \end{cases} \quad . \tag{2.30}$$

2.3.6 Critical slowing down & Correlation

As already mentioned, close to a second order phase transition the correlation length ξ diverges. When the correlation length is comparable to the system size L we get finite size effects in our simulation as discussed above. Before this happens the simulation can be affected by critical slowing down. Since the correlation of measured quantities is getting larger. Thus observables measured close to the critical point will generally have a larger error bar or have to be averaged over a substantially longer time. One way to determine this effect is by calculating a correlation of an observable with itself. This is also called autocorrelation and can be calculated as

$$\mathrm{Cor}(X(t), \tau) = \frac{\langle (X(t) - \mu)(X(t+\tau) - \mu) \rangle}{\sigma^2} \quad , \tag{2.31}$$

where X is an observable, μ is the mean value of X, and σ is the standard deviation of X. Since $\mathrm{Cor}(X(t), \tau) = \mathrm{Cor}(X(t), -\tau)$ typically only the positive

branch of $\mathrm{Cor}(X(t), \tau)$ is shown. The values of the autocorrelation function will be in the interval $[-1, 1]$, where 1 indicates full correlation, -1 indicates anti-correlation, and 0 indicates no correlation.

3 PASSIVE MODEL

3.1 CONTINUOUS ASAKURA-OOSAWA MODEL

The original Asakura-Oosawa (AO) model [42] is composed of two components which we call colloids and polymers in the following. The colloids have a hard-sphere interaction with each other as well as with the polymers, whereas the polymers behave like ideal gas particles in respect with each other and are in our case slightly smaller than their colloid counterparts. This leads to a phase separation caused by depletion forces, as it becomes entropically favourable for the colloids to cluster together and thus leave more free volume for the polymers to explore. Hence, this simple, purely repulsive model shows phase separation driven only by the density (or the packing fraction) of the two particle types.

The AO model was later extended by Zausch et al. [43] to a continuous version by introducing a soft polymer potential and replacing the hard-sphere interactions by Weeks-Chandler-Andersen (WCA) potentials [44]. By changing the interactions to continuous potentials, it becomes possible to perform MD simulations. For this reason the model is typically referred to as continuous Asakura-Oosawa (cAO) model. The resulting potentials are shown in Equation 3.1-3.3 with cc referring to the colloid-colloid, cp to the colloid-polymer, and pp to the polymer-polymer interaction.

$$U_{cc}(r) = \begin{cases} 4\epsilon_{cc}\left[\left(\frac{\sigma_{cc}}{r}\right)^{12} - \left(\frac{\sigma_{cc}}{r}\right)^{6} + \frac{1}{4}\right] & , r < r_{cc} \\ 0 & \text{otherwise} \end{cases} \tag{3.1}$$

$$U_{cp}(r) = \begin{cases} 4\epsilon_{cp}\left[\left(\frac{\sigma_{cp}}{r}\right)^{12} - \left(\frac{\sigma_{cp}}{r}\right)^{6} + \frac{1}{4}\right] & , r < r_{cp} \\ 0 & \text{otherwise} \end{cases} \tag{3.2}$$

$$U_{pp}(r) = \begin{cases} 8\epsilon_{pp}\left[1 - 10\left(\frac{r}{r_{pp}}\right)^{3} + 15\left(\frac{r}{r_{pp}}\right)^{4} - 6\left(\frac{r}{r_{pp}}\right)^{5}\right] & , r < r_{pp} \\ 0 & \text{otherwise} \end{cases} \tag{3.3}$$

As all three potentials describe a two body interaction, we use the abbreviation $r = |\vec{r}_i - \vec{r}_j|$ for the distance between two interacting particles i and j. For our simulations we choose $\epsilon_{cc} = \epsilon_{cp} = 1$, $\epsilon_{pp} = 0.0625$, $\sigma_{cc} = 1$, $\sigma_{cp} = 0.9$, and $\sigma_{pp} = 0.8$. The cutoff radii are determined as $r_{cc} = 2^{1/6}\sigma_{cc}$, $r_{cp} = 2^{1/6}\sigma_{cp}$, and $r_{pp} = 2^{1/6}\sigma_{pp}$. This corresponds to the parameters used in [43]. A plot of those potentials can be seen in Figure 3.1.

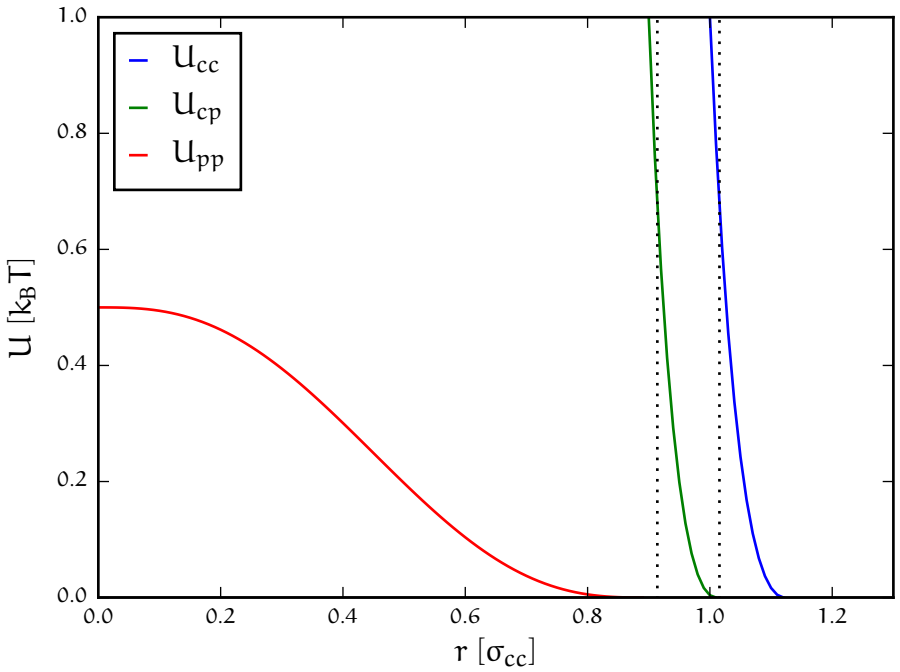

Figure 3.1: Plot of the potentials given in Equations 3.1, 3.2 and 3.3 where cc stands for the colloid-colloid, cp for the colloid-polymer and pp for the polymer-polymer interaction. The Barker-Henderson diameter d_{cc}, as calculated in Equation 3.4, and $d_{cp} = 0.9 \cdot d_{cc}$ are shown as dotted lines.

It has been shown by Barker and Henderson [45], that potentials which diverge for small radii can be mapped to hard-sphere potentials with an effective diameter d by using

$$d_{cc} = \int_0^{r_{cc}} \left[1 - e^{-\frac{U_{cc}(r)}{k_B T}}\right] dr \tag{3.4}$$
$$\overset{T=1.0}{\approx} 1.0156\sigma_{cc} \quad .$$

The same approach can be done for the colloid-polymer interaction as well, and one finds $d_{cp} = 0.9 \cdot d_{cc}$. For the polymer-polymer interaction such an approach is not possible as the soft potential is not diverging, instead we define the effective polymer diameter analogously to [43] as $d_{pp} = 0.8 \cdot d_{cc}$.

From the effective diameter an effective volume of the hard sphere is calculated and thus we define a packing fraction for the colloids and the polymers as

$$\eta_{col} = \frac{\pi}{6} d_{cc}^3 \rho_{col} \approx 0.5484 \, \sigma_{cc}^3 \rho_{col} \tag{3.5}$$
$$\eta_{pol} = \frac{\pi}{6} d_{pp}^3 \rho_{pol} \approx 0.2808 \, \sigma_{cc}^3 \rho_{pol} \quad . \tag{3.6}$$

Since the phase separation depends solely on the packing fractions of the two particle types, we get the phase diagram by plotting η_{col} against η_{pol}. In a grand canonical ensemble on can introduce a so-called polymer reservoir packing fraction η^r_{pol} [46–48] which is given by

$$\eta^r_{pol} = \frac{\pi}{6} d^3_{pp} \cdot e^{\frac{\mu_p}{k_B T}} \quad , \tag{3.7}$$

with μ_p being the chemical potential of the polymers.

We use the cAO model in this work and extend it later with an additional potential to make the colloids behave as active particles. This extension will continuously pump energy in the system. Therefore, a simulation in the microcanonical ensemble is not possible and we need a thermostat to remove excess energy (see Section 3.4 and Chapter 4). Furthermore, it is not obvious whether one can include such an extension in the pair potentials. We will attempt a mapping in Chapter 5, but for now we expect that we cannot calculate the Barker-Henderson diameter as in Equation 3.4. To still be able to compare our results with the passive model we first have to test the influence that a changed temperature or friction has on this model (Sections 3.4 and 3.5). For these comparisons we will use the phase diagram of the cAO model which will be determined as described in Section 3.3.

3.2 REDUCED UNITS

In the previous section we started already to express all length dependencies as multiples of σ_{cc} which takes the role of a length unit. Since $\sigma_{cc} = 1$ in the simulation, it makes sense to replace, e. g. all packing fractions by a unitless representation $\eta^*_\alpha = \eta_\alpha / \sigma^3_{cc}$. A similar approach can be used for other quantities as well. In the rest of the thesis we will set the mass m, ϵ_{cc} and k_B to unity and express all quantities by their reduced form while omitting the asterisk.

3.3 DETERMINING THE PHASE DIAGRAM

A short introduction into the importance of phase diagrams to characterise systems with a phase transition is given in Section 2.3.3. To determine the phase diagram in the cAO model we simulate state points that are clearly in the two phase region. That means the packing fraction of both colloids and polymers should be high enough so that a phase separation is observed. If the resulting finite size phase is a so-called slab, meaning that the colloid and polymer liquids are separated by flat interfaces, the correct equilibrium packing fractions can be

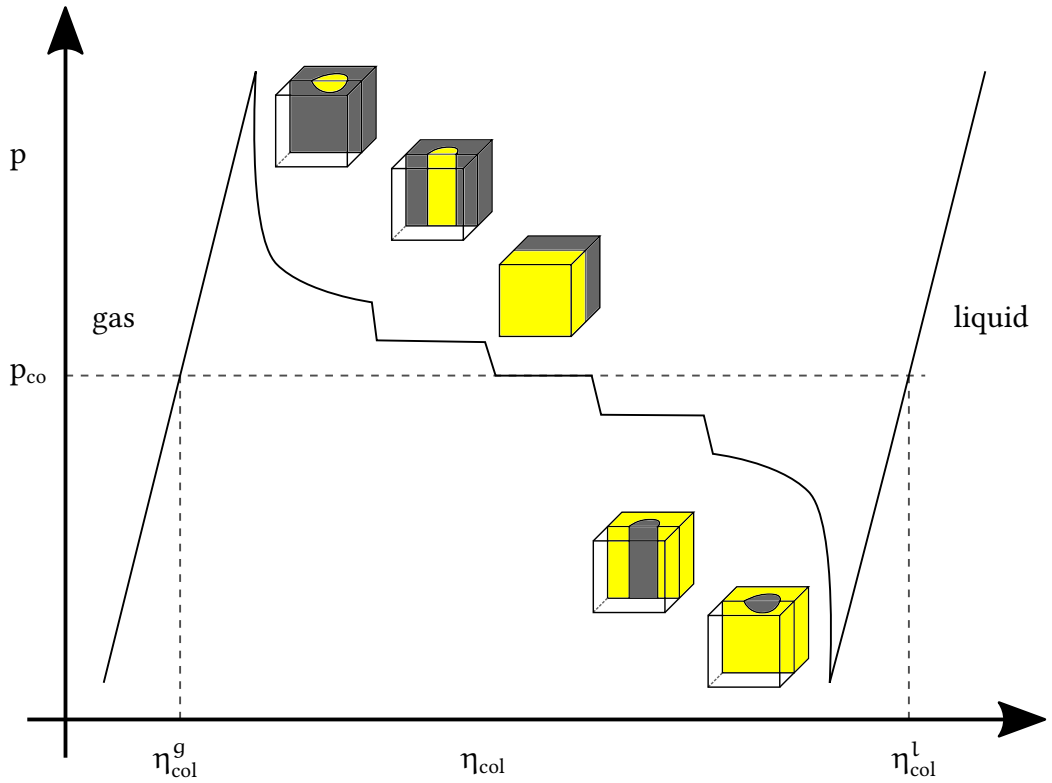

Figure 3.2: Schematic drawing of the pressure dependence on the colloid packing fraction in a finite size system at coexistence conditions. If the number of colloids is steadily increased, one starts with a homogeneous mixture of gaseous colloids and liquid polymers. By adding more colloids to the system the pressure increases until a liquid droplet is formed by the colloids. Which is then followed by a cylinder and ultimately results in a slab. If one goes on increasing the number of colloids, a polymer cylinder forms embedded in a colloid liquid, followed by a polymer sphere in a colloid liquid and ultimately a homogeneous liquid is reached and the phase transition is completed. In an infinite system one would not obtain those phases, instead the pressure would increase to the coexistence pressure p_{co} and remain there until the packing fraction of the colloids exceeds η^{l}_{col}. Idea adopted from [49].

read off in the resulting phases. In Figure 3.2 possible finite size structures are sketched for varying colloid packing fractions. To ensure that the slab configuration is the favoured structure over a long range of packing fractions we use an elongated simulation box geometry. As the system tries to reduce the interfacial tension the resulting slab is always oriented perpendicular to the elongated axis, which simplifies the analysis. Here, we chose the z-axis.

Once the system is in a phase separated state, the equilibrium packing fractions are determined. This results in two points for the phase diagram $\left(\eta^{g}_{col}\middle|\eta^{l}_{pol}\right)$ and $\left(\eta^{l}_{col}\middle|\eta^{g}_{pol}\right)$, where l stands for liquid and g for gas. This is done for one example in Figure 3.3. Figure 3.3(a) shows that the slab geometry is reached for

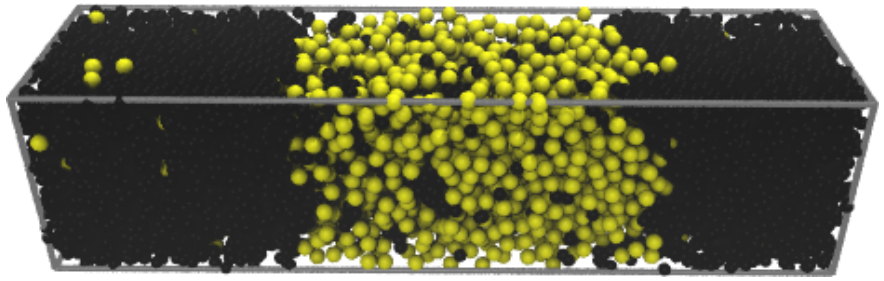

(a)

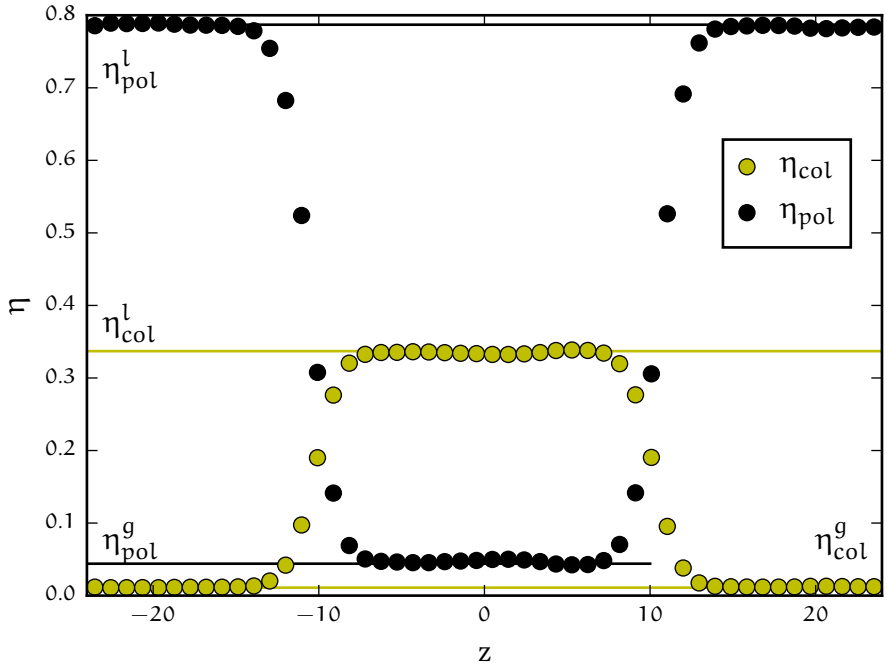

(b)

Figure 3.3: Simulation of continuous Asakura-Oosawa model with $\eta_{col} = 0.15$ and $\eta_{pol} = 0.46$ in a system of $L_x = L_y = 12\sigma$ and $L_z = 48\sigma$. (a) One exemplary simulation snapshot showing that the finite size geometry is a slab. (b) Density distribution averaged over a long simulation run, by shifting the centre of mass of the colloids to $z = 0$. The values for the phase diagram are extracted by a linear fit to the plateaus as indicated by the black and yellow lines. In this graph the linear fit results in the points $(0.337|0.044)$ and $(0.011|0.787)$, which are used in the phase diagram in Figure 3.4.

this combination of η_{col}, η_{pol}. The density distribution can now be accumulated for independent snapshots where the centre of mass of the colloids is always shifted to $z = 0$. This is done in Figure 3.3(b). From the formed plateaus one can determine the equilibrium packing fractions in both regions. This results in two points that are used in the phase diagram in the next section. Repeating this procedure for different packing fractions will result in the phase diagram

(Figure 3.4). Note, that finite size effects and critical slowing down as discussed in Sections 2.3.5 and 2.3.6 affect how close one can get to the critical point. With this technique, one will therefore always have a region around the critical point which cannot be sampled.

3.4 TEMPERATURE DEPENDENCE

The Velocity Verlet algorithm outlined in Section 2.2.2 solves Newton's equation of motion in the NVE ensemble. To allow for fluctuations in energy (NVT ensemble), a thermostat has to be added. There are several thermostats in the literature to choose from with different strengths and weaknesses. Some of them will be discussed in Section 4.4. For now we choose the Langevin thermostat to control the temperature of the passive system. This means that we have to solve:

$$m\ddot{\vec{r}}_i = -\vec{\nabla}U - \gamma m\dot{\vec{r}}_i + \sqrt{2\gamma k_B T m}\,\vec{R}_i(t) \quad , \tag{3.8}$$

with $m = 1$ being the particles' mass for all particle types, $\gamma = 1$ is a damping coefficient or friction, U is the interparticle potential, $T = 1$ is the temperature and $\vec{R}$ is a zero-mean unit-variance Gaussian white noise. We use a Velocity Verlet algorithm with a time step $\Delta t = 0.002 t_0$, with $t_0 = \sqrt{\sigma_{cc}^2 m/\epsilon_{cc}}$ similar to the one discussed in Section 2.2.2. The modified Velocity Verlet algorithm reads then:

$$\vec{r}_i(t+\Delta t) = \vec{r}_i(t) + \vec{v}_i(t)\Delta t\left(1 - \Delta t\frac{\gamma}{2}\right) + \frac{\Delta t^2}{2m}\vec{G}_i(t) \tag{3.9}$$

$$\vec{v}_i(t+\Delta t) = \frac{\vec{v}_i(t)\left(1 - \Delta t\frac{\gamma}{2}\right) + \frac{\Delta t}{2m}\left(\vec{G}_i(t) + \vec{G}_i(t+\Delta t)\right)}{\left(1 + \Delta t\frac{\gamma}{2}\right)} \quad , \tag{3.10}$$

where $\vec{G}_i(t) = -\vec{\nabla}U + \sqrt{2\gamma k_B T m}\ \vec{R}_i(t)$ is the total force. This algorithm is motivated by the so-called BBK integrator [50] which can be written in a position-velocity representation [51] and then be further reduced to a full time step integration.

To check the correctness of our simulation code we compare the phase diagram for the passive model with data obtained from MC simulations [43]. In the regions far from the critical point both coincide nicely as can be seen in Figure 3.4. Since the correlation length ξ is determined by the smallest length scale of the simulation box, the correctness close to the critical point is limited by the smallest length scale as the correlation length diverges. To get closer to the critical point one has thus to use a bigger system.

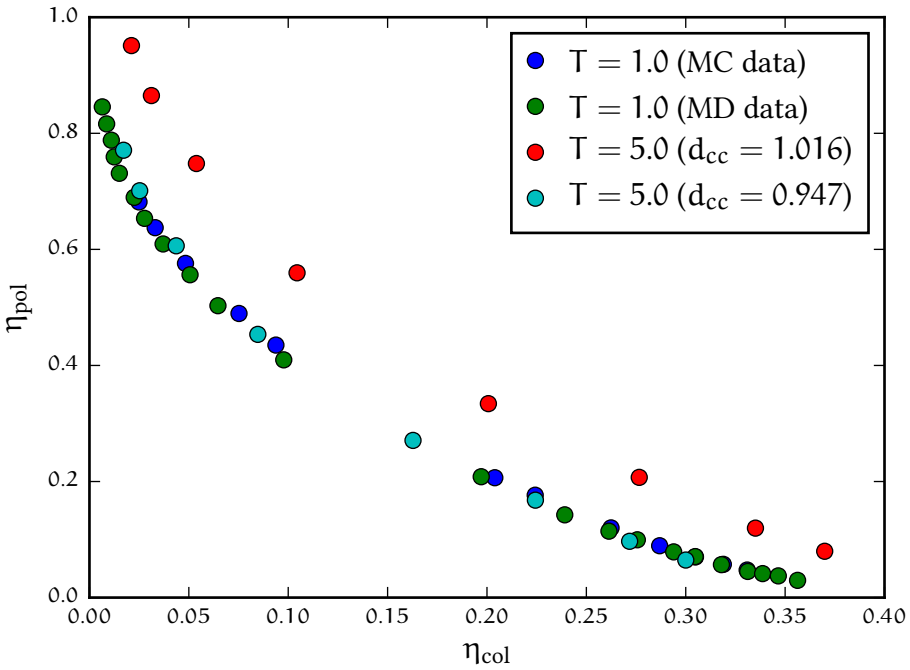

Figure 3.4: Comparison of the results of the cAO model obtained with MC (blue) (data from [43]) and MD simulations (green). The MD data is generated in a system with $L_x = L_y = 12\sigma$ and $L_z = 48\sigma$. The phase diagram does not change for higher temperatures T as long as one accounts for an adjusted Barker-Henderson diameter (see Equation 3.4) (cyan). If one does not change the effective diameter d_{cc} the phase diagram shifts to higher packing fractions (red).

In Figure 3.4 we calculate the phase diagram for different temperatures. It is clear that the cAO model is not temperature sensitive as long as one calculates the correct Barker-Henderson diameter. However, if the effective pair potential is not known, as in the active case, the Barker-Henderson formalism cannot be applied. Therefore, we note that a higher temperature shifts the phase diagram to higher packing fractions if the effective diameter is unchanged. This is also what one would naively expect as a higher kinetic energy prevents the colloids from clustering.

3.5 FRICTION DEPENDENCE

The Langevin thermostat introduces another parameter which can be chosen independently from the temperature; the friction γ. Since the friction neither enters the equations of the potentials nor changes the Barker-Henderson diameter, one would not expect it to have an influence on the passive system. This

is shown in Figure 3.5. However, it is likely that an active system which is by definition not in equilibrium behaves differently.

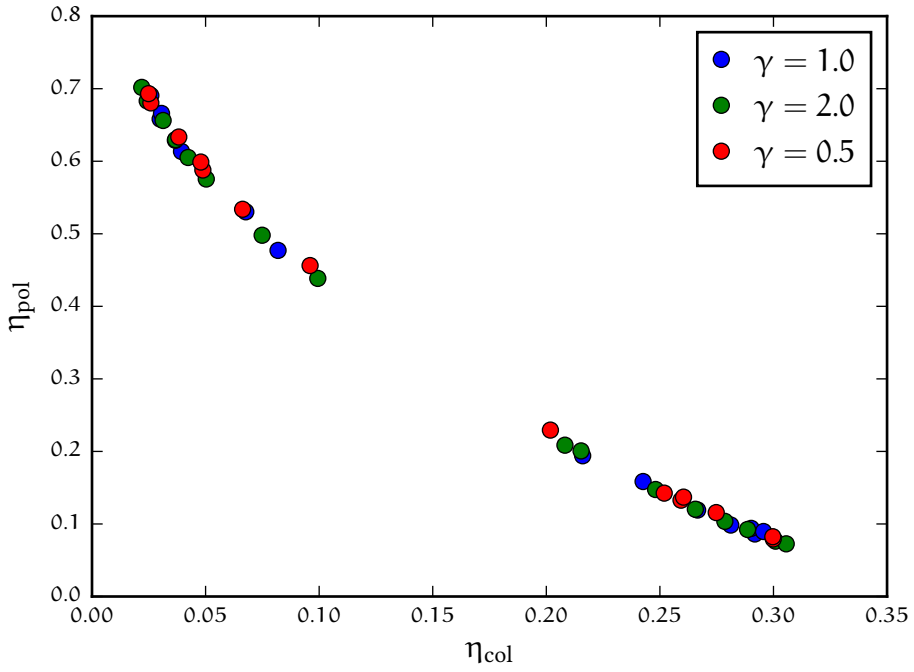

Figure 3.5: Comparison of the effect of different values for the friction γ for the passive cAO model. All values of γ result in the same phase diagram.

4 ACTIVE MODEL

4.1 CONSTRUCTING AN ACTIVE SYSTEM FROM THE PASSIVE MODEL

4.1.1 The active Vicsek model

To compare an active with a passive model, we want to remain as close as possible to the passive model discussed in Chapter 3. Ideally, the new model contains the equilibrium result as a limit of one parameter that describes the activity of the system and can be changed continuously. This will allow us to directly compare the two models and study the effect the added activity has on the system.

A well-known model for active particles is the Vicsek model [28, 52], which was introduced to study the structure and dynamics of clustering active particles. This can be achieved by applying an alignment rule to the self-propelled particle so that it moves in a similar direction as neighbouring particles. This alignment is well motivated for macroscopic systems, as birds would not want to crash into each other. In microscopic systems it can be interpreted as steric interaction or hydrodynamic effects [53]. In [53] a Vicsek-like model is used to successfully compare experiments of self-propelled bacteria with simulations. The Vicsek model generates correlations between active particles, which leads to a clustering effect and introduces a phase separation that is not present in the passive model. It is worth noting that self-propelled particles do not in general enhance clustering. While there are observations where phase separation is induced by motility [54], the contrary has been observed as well [55].

We construct the active model by adding a variation of the Vicsek model [28] on top of the passive cAO model. For that we still solve the Langevin Equation 3.8 first just as in the passive model. The resulting velocity is then modified by an additional force $\vec{f}_i$ which is acting on the active particle i as determined by Equation 4.1.

$$\vec{f}_i = f_A \cdot \frac{\langle \vec{v}_j \rangle_R}{\langle |\vec{v}_j| \rangle_R} \tag{4.1}$$

The constant force is set to $f_A = 0$ for the polymers and $f_A = 10$ for the colloids, if not stated otherwise. $<>_R$ denotes the average in a sphere of radius R, with $R = \sqrt{2}\, r_{cc}$ being the cut-off radius for what is considered a neighbour. Note,

that the colloids interact only with neighbouring colloids, but that the velocity of the colloid itself is also respected. Therefore a non interacting particle is pushed in its direction of motion, hence is self-propelled. Additionally the active force $\vec{f}_i$ introduces an alignment and thus a correlation between the active particles which is similar to the alignment rule in the original Vicsek model.

For the implementation of this model we keep the integration algorithm as defined in Equations 3.9 and 3.10 and update the velocities after this Velocity Verlet step by

$$\vec{v}_{act}(t + \Delta t) = \vec{v}(t + \Delta t) + \frac{\Delta t}{m}\vec{f}_i(\vec{r}(t + \Delta t), \vec{v}(t + \Delta t)) \ , \tag{4.2}$$

where $\vec{v}(t + \Delta t)$ is the velocity determined by the Velocity Verlet step. Note that this is technically no longer a Velocity Verlet algorithm, as the active force can only be calculated when both the positions $\vec{r}$ and velocities $\vec{v}$ are known. Therefore the half time step of the velocity which is used in the derivation of the Velocity Verlet algorithm (compare with Section 2.2.2) would have an undefined active force. We solve this problem by integrating the system as before and change the velocity once the position and velocities are known. One can think of this as a run and tumble update of the particles. In each integration step the particles are first treated as if they were passive and are moved according to the potentials (run), then they are influenced by the surrounding active particles and their direction or in this case their velocity is updated (tumble). This algorithm still has the advantages of the Velocity Verlet algorithm for the passive update. The active part is integrated as an Euler algorithm, similar to the standard integration for other active particles as well e. g. [56]. An alternative interpretation is to treat the active interaction as kind of an "activity thermostat". In each time step the velocities are adjusted according to the average velocity of surrounding particles. Independent of the interpretation this update method has the passive system as its limit for $f_A \to 0$ and the correct integration method is regained for no active force which was the initial goal.

4.1.2 Steady state

With this additional directed force heat is pumped into the system and the temperature will no longer be the same as the initial temperature set by the thermostat. Instead the system will have an increased temperature $T_{active} > T$ as can be seen in Figure 4.1, where the active colloids carry most of the heat. Once T_{active} is reached, the temperature does no longer increase. While the active particles are still pumping energy into the system, the thermostat is now removing the same amount. While this state is clearly not the same as an equilibrium state,

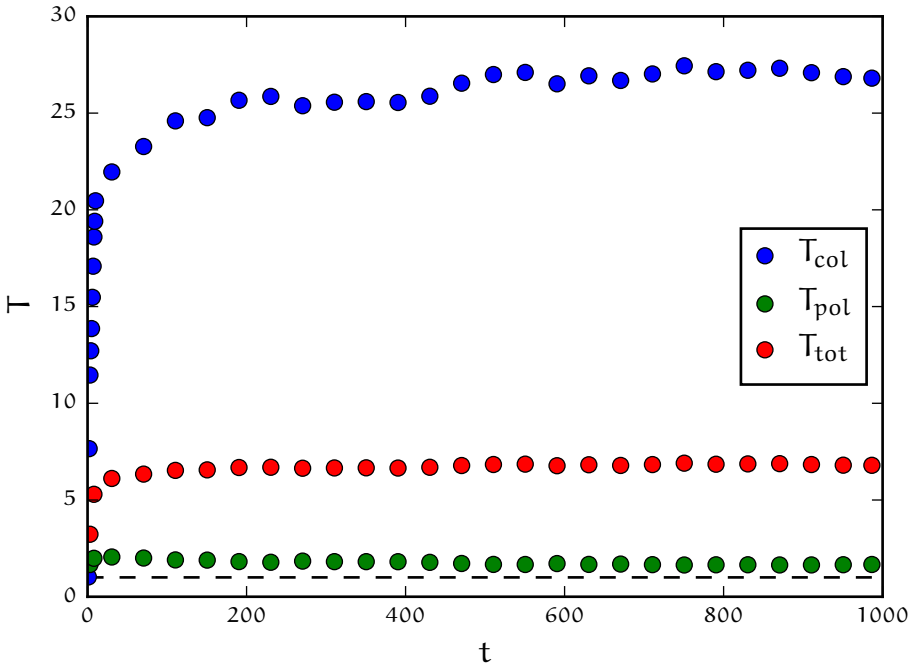

Figure 4.1: "Equilibration" of temperature distinguished by particle type and as a total at the state point $\eta_{col} = 0.15$ and $\eta_{pol} = 0.30$. The initial temperature of the thermostat is set to $T_{init} = 1.0$ and is shown by the black dashed line. The average temperatures for this state point after the system has reached the steady state are: $\langle T_{col} \rangle = 27.3$, $\langle T_{pol} \rangle = 1.6$ and $\langle T_{tot} \rangle = 6.9$.

one can still expect that static observables, like e. g. the density distribution, do no longer change with time. Therefore we call this state a steady state.

In the cAO model the temperature plays only a minor role. As shown before the main reason for a phase separation is the entropic attraction of the colloids at high enough densities. But since the hard sphere interactions got replaced by a smooth potential in order to be able to perform MD simulations we will have a temperature dependence if we do not adjust the Barker-Henderson diameter as discussed in Section 3.1. Unfortunately, the Barker-Henderson approach from Equation 3.4 cannot be applied to the Vicsek potential since it is not a pairwise interaction. Therefore, the increased temperature should lead to phase separation at higher packing fractions as displayed in Figure 3.1. Instead Figure 4.2 shows that the addition of activity leads to phase separation at lower densities due to the clustering effect of the Vicsek interaction. This indicates that the increased temperature plays a minor role compared to the clustering effect of the active model. The clustered colloids move through the system and collect the remaining free colloids, which drives the phase separation. The melting of such a cluster is repressed by the alignment rule from Equation 4.1.

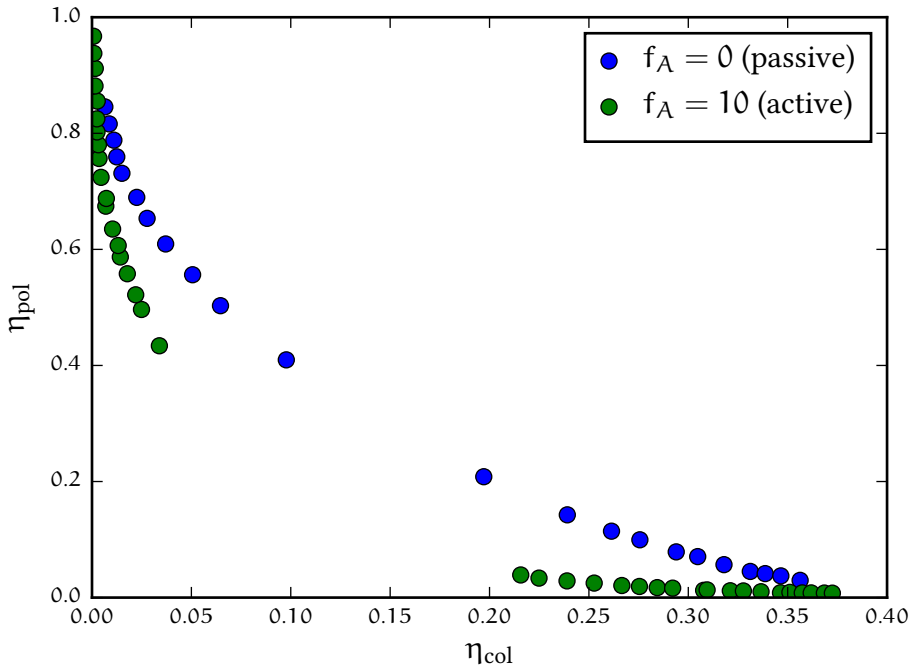

Figure 4.2: Comparison of the cAO with the active model. The phase separation happens earlier if we switch on the Vicsek model ($f_A = 10$). The simulation box has the dimension $L_x = L_y = 12\sigma$ and $L_z = 48\sigma$.

We have introduced a model of activity that mostly depends on one parameter f_A that controls the activity of the system. If we set $f_A = 0$ for both particle types we regain the passive model. Thus the constructed model will return the passive results for $f_A \to 0$. For active forces greater than zero the temperature can no longer be held at the initial value but rises until a steady state is reached. We have shown that such a temperature increase would in principle hamper phase separation in the underlying passive cAO model. Nevertheless, in the active model phase separation is facilitated which is due to the clustering effect of the Vicsek model.

4.1.3 Choice of cut-off radius

In the definition of the active model the cut-off radius R, which is determining what is considered a neighbour, is introduced as a free parameter. Since the interaction radius determines the average number of velocities over which the Vicsek update averages, it is clear that the choice of R will influence the clustering effect of the active model. However, the strength of the interaction is only dependent on the active force f_A so that the interaction radius has only a minor influence. In Figure 4.3 the phase diagrams for various interaction radii are shown. Since

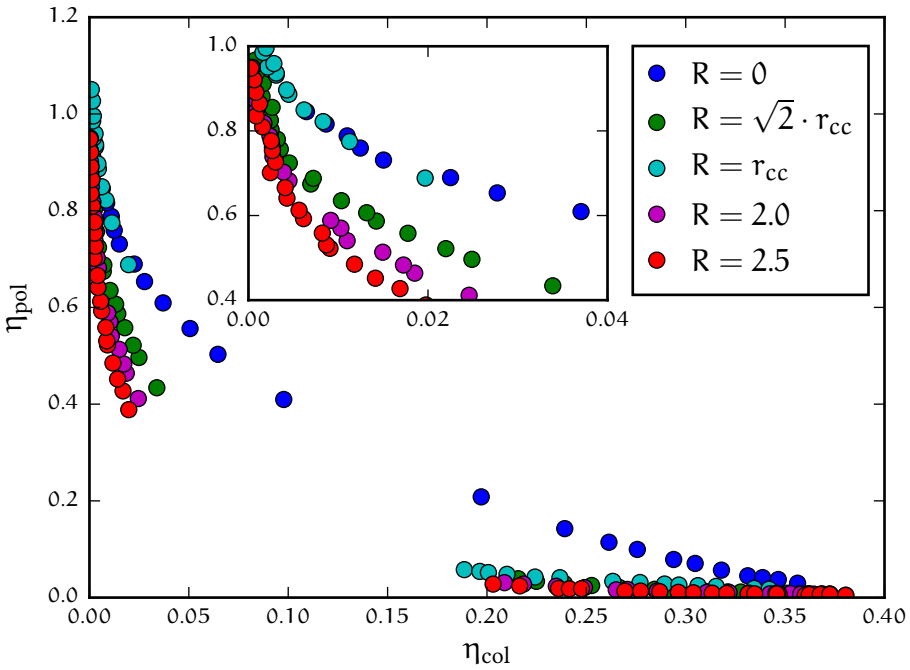

Figure 4.3: Phase diagram for various values of the interaction radius R at a constant active force of $f_A = 10$. The green and blue dots correspond to the green and blue data points in Figure 4.2 respectively. Larger radii lead to faster phase separation, but the effect is rather small, especially in the colloid rich branch. The polymer-rich branch is shown magnified in the inset.

the differences are only minor, the polymer-rich branch is magnified in the inset. A bigger cut-off radius facilitates phase separation, but slows the computation down, since one has to account for bigger cells in the simulation program. A small cut-off radius leads to a big discrepancy of the colloid-rich and colloid-deprived branch as shown exemplary for $R = r_{cc}$. The polymer-rich branch can no longer be distinguished from the passive branch, but due to the self-interaction of the colloids, the colloid-rich branch is nearly unchanged. Therefore the passive model for which $R = 0$ is different from the limit of $R \to 0$. This is due to the fact that the particles remain self-propelled for $R > 0$ since they still see themselves as a neighbour. Hence it is not a good idea to replace f_A by R as the parameter to describe the activity of the system and we set $R = \sqrt{2} \cdot r_{cc}$ for all following simulations.

4.1.4 Active Model with noise term

The Vicsek model can be further altered to yield more forms of activity by adding a noise term ν to Equation 4.1. After calculating the active force and the direc-

tion in which it should apply, the direction is rotated randomly in the interval $\nu \cdot \phi, \phi \in [-\pi, \pi]$. In the original Vicsek model this is motivated as an uncertainty or error with which, e. g. , a bird would choose its direction to match the direction of neighbouring birds [28]. Therefore, the noise ν is the order parameter in the original Vicsek model.

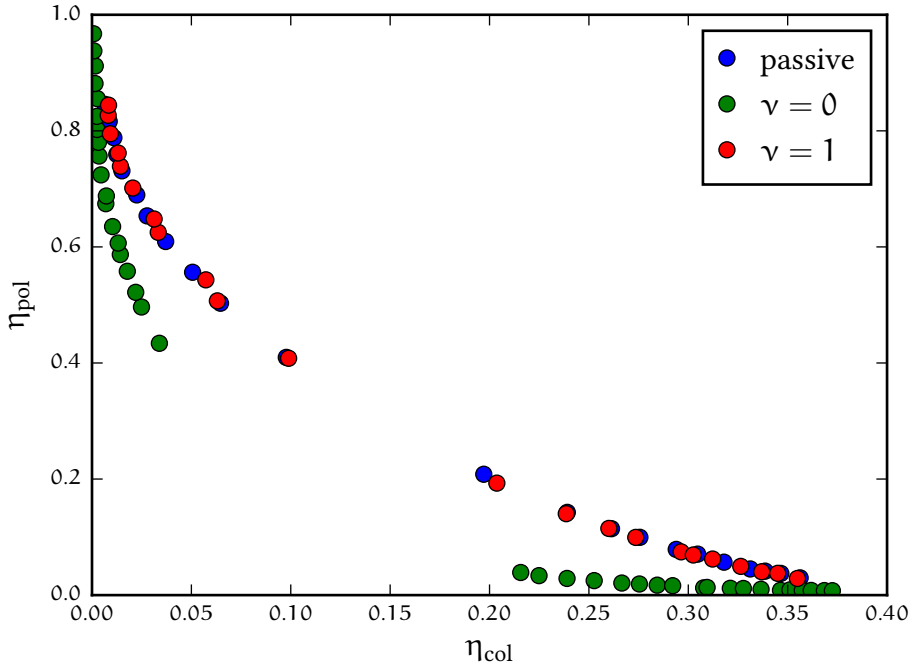

Figure 4.4: Variation of the noise ν. For $\nu = 0$ we get the phase diagram as discussed before. Due to the clustering effect of the Vicsek model the phase separation happens at lower packing fractions. $\nu = 1$ results in a randomly distributed active force which results in the same phase diagram as the passive system. The temperature is equal to the initial temperature $T = 1$ of the thermostat.

In Figure 4.4 two values of the noise are shown. For $\nu = 0$ we get the same results as before, while for $\nu = 1$ we recover the passive system, as the force is now no longer directed but distributed randomly, and the thermostat manages to cool the system to the desired temperature. For values in between the phase diagram will change accordingly.

This addition to the model is not pursued in the rest of the thesis for two reasons: On the one hand the change of the noise parameter ν has a similar effect on the phase diagram as a change of the active force f_A, as can be seen in Figure 4.2 and which will be further discussed in Section 4.2.2. On the other hand the addition of a noise term can hardly be motivated in our model. In the classical Vicsek model the particles are ideal point-like particles that only interact via a neighbouring rule similar to Equation 4.1, while in our model the noise is generated

by the interacting particles themselves. The noise will therefore be set to $\nu = 0$ for all following simulations.

4.1.5 Other implementations of a Vicsek-like model

There are several other ways one could implement a Vicsek-like model. Two of these options are briefly introduced here, but we will not pursue them any further in this thesis.

First we look at an implementation closer to the original Vicsek model, where the velocities are rotated in the neighbour update. For that we still calculate the mean direction of the neighbouring velocities as in Equation 4.1. But instead of the update in Equation 4.2 we rotate the calculated velocities to match the mean direction:

$$\vec{v}_{act}(t + \Delta t) = \hat{f}_i \cdot |\vec{v}(t + \Delta t)| \quad . \tag{4.3}$$

It turns out that this update method leads to a lot of noise in the system and no proper phase separation can be observed. The main reason why this method is unsuited as an implementation is that if two particles overlap they get a strong kick to separate from the potential forces, but since the velocity is then rotated they do not necessarily separate which leads to even more noise and energy in the system. Due to the Velocity Verlet algorithm we use for the passive update, the particles will not get stuck with each other, since the force enters the calculation of positions directly as well. In contrast to the model we are using this method does not pump energy into the system directly. Thus it might be better suited for other applications.

Alternatively, we look into a method that only treats the divergence of a particle from the collective motion. Again, we keep Equation 4.1 to determine the mean direction and replace the velocity update in Equation 4.2 by Equation 4.4.

$$\vec{v}_{act}(t + \Delta t) = \vec{v}(t + \Delta t) + \frac{\Delta t}{m} \cdot \left(\vec{f}_i - (\hat{v}(t + \Delta t) \cdot \vec{f}_i) \cdot \hat{v}(t + \Delta t) \right) \quad . \tag{4.4}$$

The particle itself is always included in this average and thus the resulting average direction will be similar to the current velocity of the particle if inside a cluster. Therefore it can be expected that this model will generally have slower dynamics than the active models from before as the correction terms will be small for aligned particles. A particle without any neighbours will now behave as a passive particle, since the orthogonal component will vanish, thus we no longer are looking at self-propelled particles. This prevents a cluster of aligned

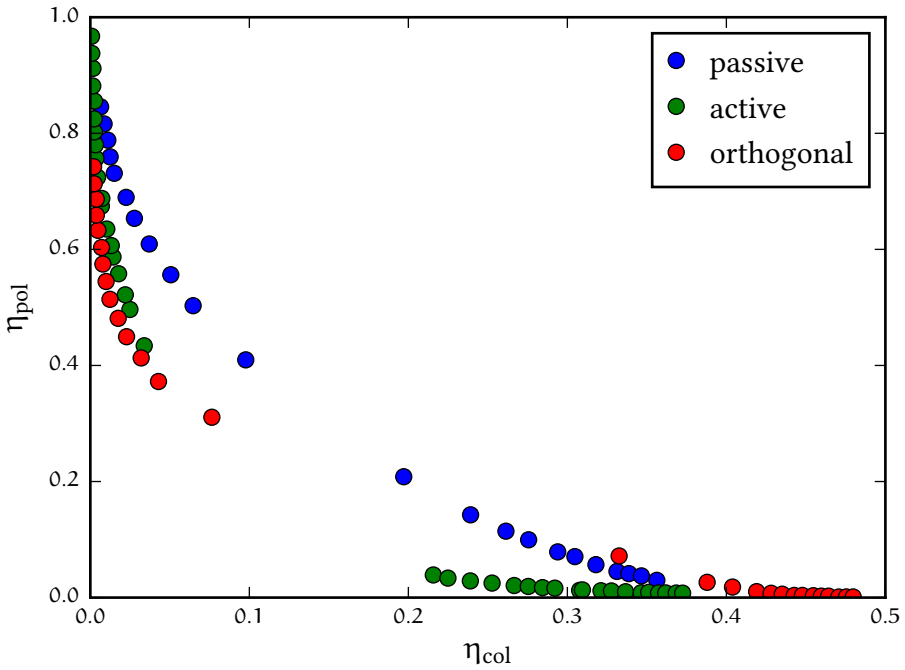

Figure 4.5: Phase diagram for the cAO model (blue), the Vicsek-like model from Section 4.1.1 (green) and the here discussed model where we only look at the orthogonal component of the Vicsek force (red). The orthogonal model will cross the phase boundaries of the other models at some point, since the polymer-rich branch is below the other branches, while the colloid-rich is above.

particles to speed up, as only the noise of the collective motion is treated. The orthogonal correction to their velocity will nonetheless still lead to a collective motion, while the temperature of the system remains at the initial set value for the thermostat. Again this way of implementing a Vicsek-like model could be better suited for certain applications. The phase diagram, which can be seen in Figure 4.5, changes dramatically for this implementation of the Vicsek model. For the same active force $f_A = 10$ the polymer-rich branch is deeper than in the active model, while the colloid-rich branch is even higher than in the passive case. So that we can speak of a completely different model. While we retain the passive model in the limit of $f_A \to 0$ we get a crossing for the phase boundaries for higher active forces which is unfavourable for the studies we intend to do. Therefore we stick to the Vicsek-like model described in Section 4.1.1.

As a general remark: one could always remove the self-propelled nature of a model by rescaling the active velocity $\vec{v}_{act}$ to match the norm of the passive velocity.

$$\vec{v}_{act}(t) \to \frac{|\vec{v}(t)|}{|\vec{v}_{act}(t)|} \cdot \vec{v}_{act}(t) \tag{4.5}$$

With that it is possible to study collective motion without self-propulsion.

4.2 COMPARISON WITH THE PASSIVE MODEL

4.2.1 Friction dependence

In Chapter 3 we have seen the dependence of the passive model on friction and temperature. With the definition of active particles we can now look at how those dependencies change by varying some parameters. We start by looking at

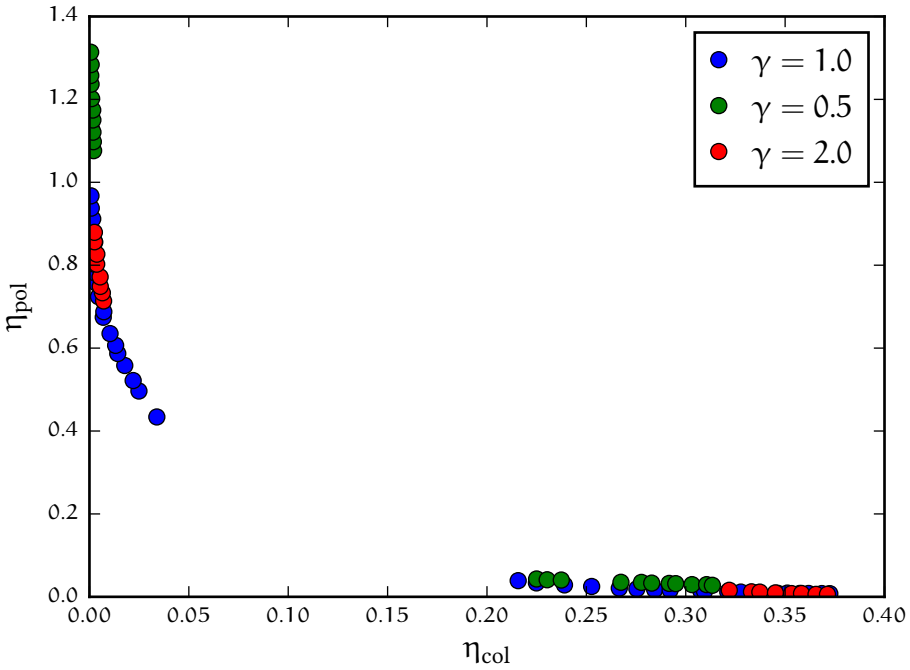

Figure 4.6: Variation of γ for the active model with $f_A = 10$. Changing the value of γ affects where we are on the phase boundary, when starting from the same initial values of η_{col} and η_{pol}. However, the overall structure of the phase diagram is unchanged.

different damping factors γ from Equation 3.8, which obviously do not change the passive system (Figure 3.5). In Figure 4.6 the phase diagram of the active system is shown for different values of γ. The influence on the phase boundaries is minor, in a sense that we appear to get the same locus for the phase diagram. However, starting from the same initial configurations can lead to different final points on the phase boundary. For $\gamma = 0.5$ we are at the lower values of $\gamma = 1.0$ in the colloid rich phase, while we are way above the higher values of $\gamma = 1.0$ in the polymer rich phase. For $\gamma = 2.0$ the result is not as extreme, but still noticeable. These results indicate that the choice of the friction parameter γ

could affect the position of the critical point in the active model. While this is an intriguing idea we will see later how difficult the determination of the critical point in this model is, thus the variation of the friction is not included and γ is set to unity for the rest of this work.

4.2.2 Active force dependence

Next we look at the influence different forces f_A in Equation 4.1 will have on the phase diagram. In Figure 4.7 one can see that for an active system with

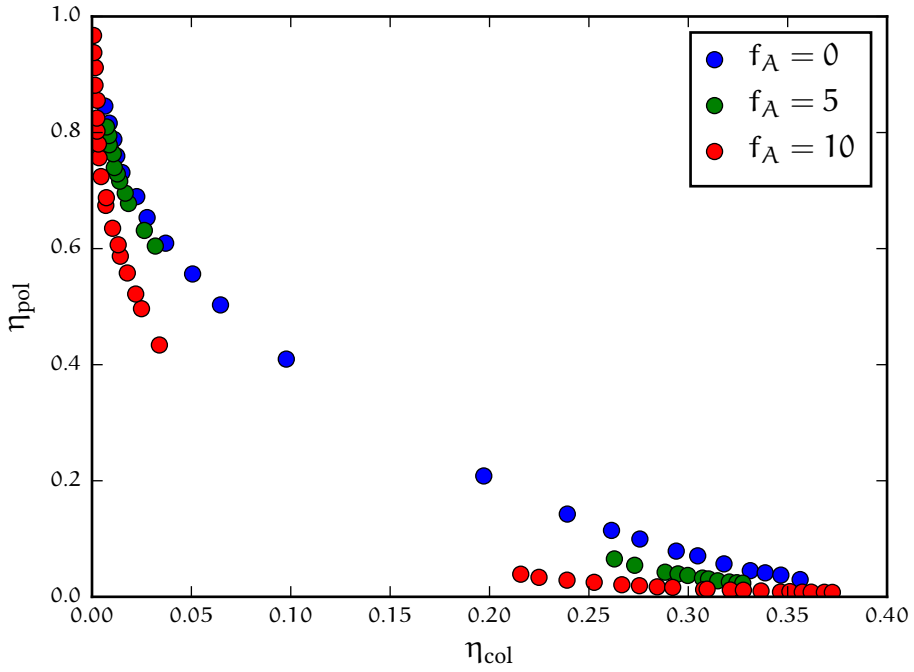

Figure 4.7: Variation of f_A. For higher colloid numbers one can clearly see that $f_A = 5$ (green) is in between the passive model $f_A = 0$ (blue) and the "more" active system with $f_A = 10$ (red).

$f'_A = f_A/2$ the phase diagram is located somewhere in between the passive and the previous active case as expected. Higher forces hence facilitate phase separation. Forces larger than $f_A = 10$ were not considered because even for $f_A = 10$ both branches of the phase diagram are already close to the axis and the intermediate regime cannot be sampled due to finite size effects close to the potential critical point.

Starting with the same colloid and polymer number and varying the active force we can determine the evolution of the passive system to the active system. This is done exemplary for a configuration with $\eta_{col} = 0.12$ and $\eta_{pol} = 0.40$ in

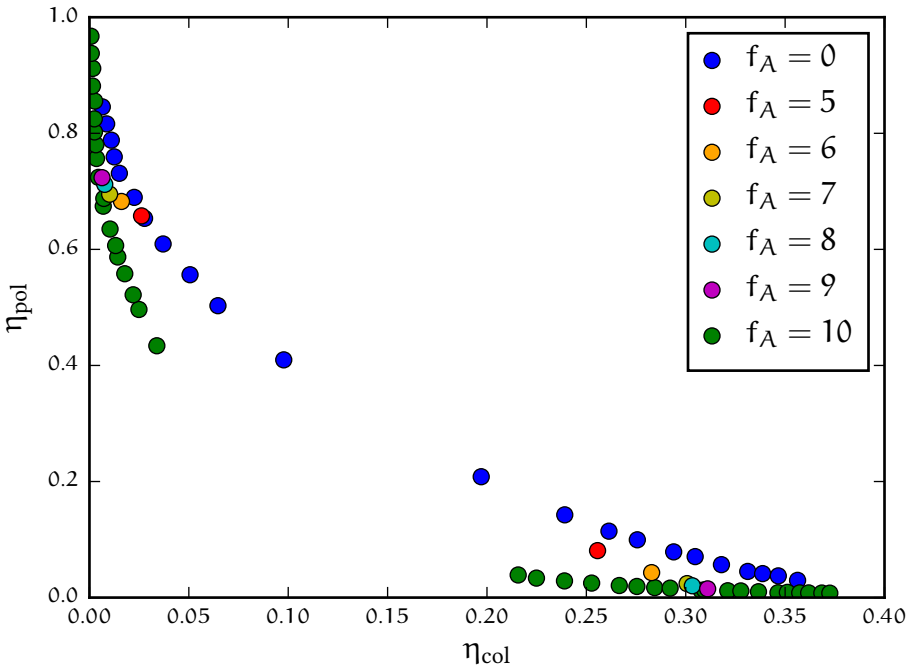

Figure 4.8: Variation of f_A for the same starting configuration of $\eta_{col} = 0.12$ and $\eta_{pol} = 0.40$ in a $L_x = L_y = 12$ and $L_z = 48$ simulation box. For $f_A = 0$ and $f_A = 10$, the whole phase diagram is shown for comparison.

Figure 4.8. The evolution is not linear in force, since for higher forces we are already close to the axes, while for smaller forces we get into a regime which is already in the vicinity of the critical point of the passive system.

The influence of the temperature on the active system is the topic of the following sections, as the definition of temperature in non-equilibrium systems is challenging and the results might depend on the chosen thermostat.

4.2.3 Differences to the passive model

We have shown so far that the active model features a similar phase separation as the passive model. However due to the clustering nature of the active model this phase separation occurs earlier. Of course, the Vicsek update will effect the dynamics of the system as well. For this we will examine the mean square displacement (MSD), which we calculate for the colloids as

$$\mathrm{MSD} = \left\langle |\vec{r}_i(t) - \vec{r}_i(0)|^2 \right\rangle \quad . \tag{4.6}$$

For a system in equilibrium one expects to reach a diffusive regime where the MSD is linear in time after a short time of ballistic motion where the MSD scales

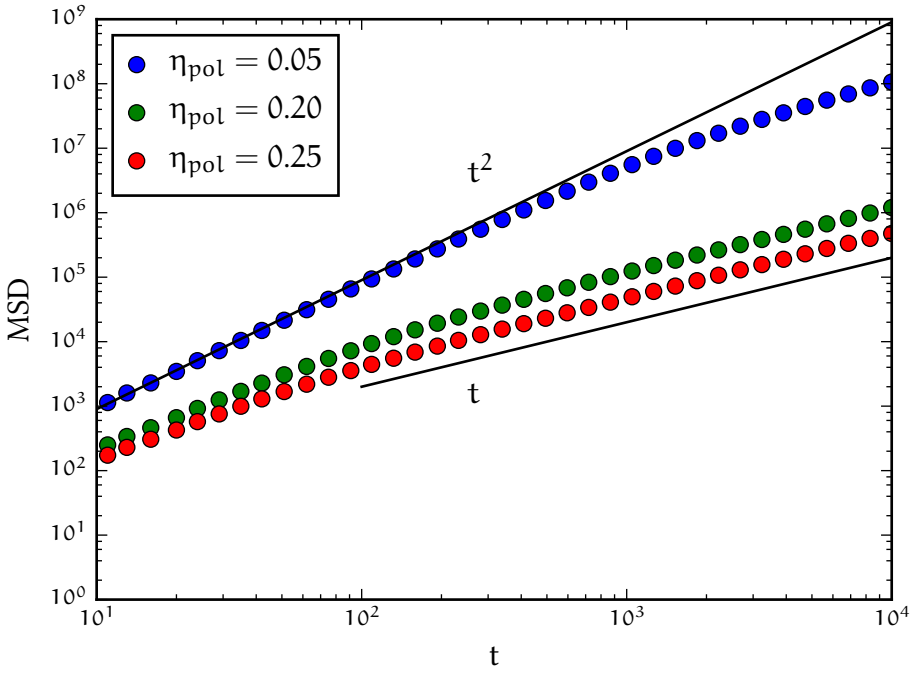

Figure 4.9: The mean square displacement for the active model with $f_A = 10$, $\eta_{col} = 0.05$ and different values of η_{pol} which are mentioned in the legend. The system size is $L = 12$. For a high colloid concentration the linear regime appears later.

with time squared. In Figure 4.9 three different polymer packing fractions are studied for a fixed colloid packing fraction of $\eta_{col} = 0.05$. All simulated state points are in the homogeneous phase of the active system. The higher the active particle concentration, the later the linear regime is reached. For $\eta_{pol} = 0.05$ we just left the ballistic regime and a lot longer simulation would be necessary to get to the linear regime. Therefore, the active model introduces an increase in the time scale of fluctuations.

Additionally, we determine the time evolution of the average velocity fluctuation of the colloids. For that we look at a configuration in the one phase region as well as one that is clearly phase separated. In the one phase region we expect the average velocity to be independent of the spatial component. In contrast the slab should be stable in regards to its normal axis once the two phases are separated. In Figure 4.10 both cases are shown. For Figure 4.10(a) only the x component is shown, as y and z follow the same trend. The time average is $< v_x >= 0.25$ while the standard deviation is $\sigma(v_x) = 2.9$. Thus the active model enhances the amplitude of the velocity fluctuations. In Figure 4.10(b) the same analysis is done in a phase separated system where the fluctuations are greatly reduced, while the averages are no longer necessarily close to zero. The results for this

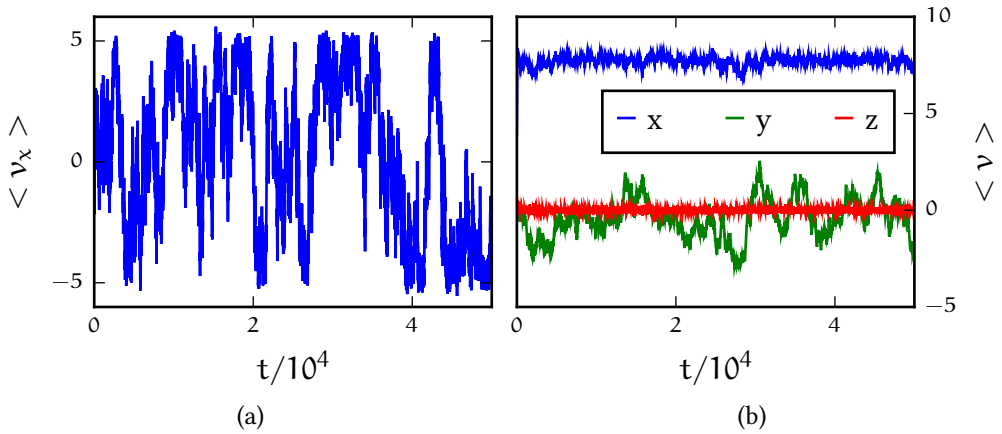

Figure 4.10: The evolution of the average velocity with time for a configuration in the (a) one phase region $\eta_{col} = 0.05$, $\eta_{pol} = 0.05$ in a system with $L = 12$ and (b) the phase separated case $\eta_{col} = 0.15$, $\eta_{pol} = 0.20$ in a system with $L_x = L_y = 12$ and $L_z = 48$ in this case the cluster moves along the x-direction.

example can be seen in Table 4.1. The fact that the velocity component normal

α	$< v_\alpha >$	$\sigma(v_\alpha)$
x	7.7	0.2
y	−0.4	1.0
z	0.0	0.1

Table 4.1: The mean velocities and the respective standard deviations for the data shown in Figure 4.10(b)

to the interface does not vary, indicates that we indeed simulate a steady state with the slab as a stable finite size structure. The velocity components parallel to the interface carry the heat that the active model introduces to the system. Due to the strong alignment the cluster, once formed, can hardly change its direction, thus the fluctuation decreases compared to the one phase region. The direction the cluster travels is therefore determined shortly after initialisation and can be either in x- or y-direction.

4.3 CAN WE DEFINE A TEMPERATURE?

When we introduced the active model we stated that the alignment rule pumps energy into the system and thus the temperature rises, ignoring at first how the temperature would be defined. For that we will first recall how the temperature is defined in equilibrium and then formulate a definition for our steady state.

In a system in thermodynamic equilibrium the temperature is defined by the equipartition theorem [57].

$$\left\langle x_m \frac{\partial H}{\partial x_n} \right\rangle = \delta_{mn} k_B T \tag{4.7}$$

Here x is a generalised coordinate and $H(\vec{q}, \vec{p})$ is the Hamiltonian of the system:

$$H(\vec{q}, \vec{p}) = \sum \frac{\vec{p}_i^2}{2m} + V(\vec{q}) \quad , \tag{4.8}$$

where V is the potential energy of the system. Typically one chooses the generalised momenta $\vec{p}$ and gets with Equation 4.7

$$k_B T_{inst} = \left\langle p_m \frac{\partial H}{\partial p_m} \right\rangle = \frac{1}{3} \left\langle \frac{\vec{p}^2}{m} \right\rangle = \frac{2}{3} \langle E_{kin} \rangle \quad . \tag{4.9}$$

This is a temperature which can be recorded at no extra cost since the velocities and therefore the momenta are known in every integration step, hence the name instantaneous temperature T_{inst}. All similar definitions will result in the same average for the temperature of a system in equilibrium, which is why typically only this definition is considered. However, even in equilibrium different definitions of temperature might converge differently towards the equilibrium value, and thus can give an indication on how long it takes the system to reach an equilibrium state [58].

We want to additionally use a temperature that is not based on the momenta but on the generalised positions of the particles instead. One possible temperature that only depends on the relative positions is the so-called configurational temperature T_{conf} [58]:

$$k_B T_{conf} = \left\langle \frac{\sum_{i=1}^{N} \vec{F}_i^2}{-\sum_{i=1}^{N} \vec{\nabla} \vec{F}_i} \right\rangle = \frac{\left\langle \sum_{i=1}^{N} \sum_{j \neq i} \left(\frac{\partial U}{\partial x_{ij}} \right)^2 \right\rangle}{\left\langle \sum_{i=1}^{N} \sum_{j \neq i} \frac{\partial^2 U}{\partial x_{ij}^2} \right\rangle} \quad , \tag{4.10}$$

with N being the number of particles, F_i the force acting on particle i, U the potential and x_{ij} the distance of the particle pair. The proof that this is indeed a correct definition of temperature (for NVE and NVT ensemble) and a more general form of the equipartition theorem can be found in [58]. Similar definitions of temperature have been applied successfully in the past even in non-equilibrium systems, e. g. [59].

In a non-equilibrium system the question of how to measure the temperature arises. While the equipartition theorem is no longer fulfilled and thus the different methods to determine the temperature will have a different average, the

temperature can still give us an indication as to what is happening in the system. In our model two different temperatures are present if the phases are separated: the temperature of the polymers which is close to the one set by the thermostat and the temperature of the phase separated colloids which is way higher. This distribution of temperature will be discussed in the next section. For now we will monitor the "standard" definition of temperature as defined in Equation 4.9 and refer to it as T_{inst}. This leads to quite high temperatures for the active particles in their steady state. We also calculate the configurational temperature as defined in Equation 4.10 [58]. With this method we measure a significantly lower overall temperature in our active system (as can be seen in Figure 4.11(a)), while the temperature in the passive case remains (obviously) unchanged (see Figure 4.11(b)). This indicates that the activity, as one would expect, is mostly in the kinetic part of the energy, while the configurations are similar to the ones in the passive case.

4.4 COMPARISON OF DIFFERENT THERMOSTATS

In an equilibrium system a thermostat has to be chosen in a way that the correct thermodynamics, e. g. , the canonical ensemble are preserved and that the dynamics of the system remain realistic. For this task various thermostats are used in MD simulations with different advantages and disadvantages. A good thermostat will not change the thermodynamics of a system in equilibrium, but it can have a considerable impact on a non-equilibrium system. To measure a static observable, e. g. the density distribution, one needs to have a system that is in a steady state, so that the static variable is no longer changing as a function of time. This state however, will depend on the thermostat that was used to reach it. Therefore, the choice of the thermostat plays an important role. In our model the thermostat has to somehow remove the induced heat, but also leave the collective motion induced by the active particles undisturbed.

In the following we will look at three different thermostats. Namely the Langevin thermostat [37], the Lowe-Andersen thermostat [60] and an implementation of a multi-particle collision dynamics (MPCD) thermostat [61]. Of course this is not an exclusive list of thermostats, but rather what we have already tested.

4.4.1 Langevin thermostat

The Langevin thermostat has already been described in Section 3.4 for the cAO model and in Section 4.1.1 for the active model. As a quick reminder, we want to solve

$$m\ddot{\vec{r}}_i = -\vec{\nabla}U - \gamma m\dot{\vec{r}}_i + \sqrt{2\gamma k_B T m}\,\vec{R}(t) \quad , \tag{3.8}$$

with $m = 1$ being the mass for all particle types, $\gamma = 1$ being a damping coefficient, U is the particle potential, $T = 1$ is the temperature and $\vec{R}$ is a δ correlated noise by using a Velocity Verlet (VV) algorithm with a time step $\Delta t = 0.002$. In

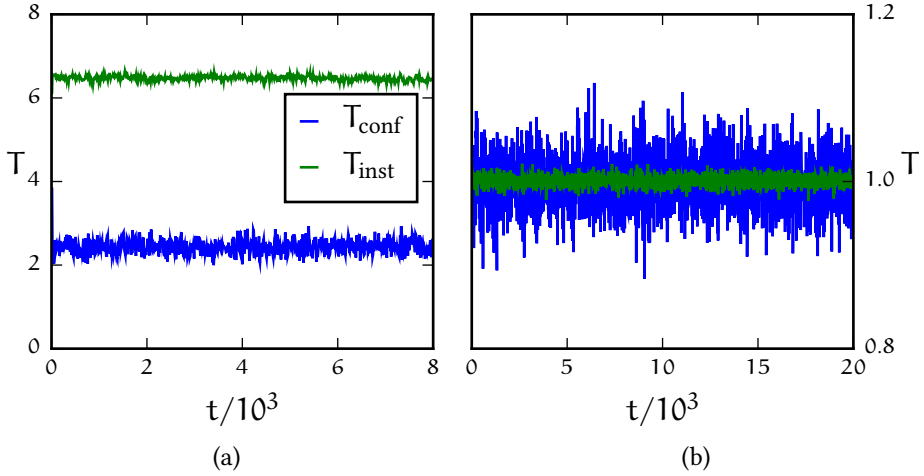

Figure 4.11: Comparison between the two methods to measure the temperature of all particles with the Langevin Thermostat ($T_{initial} = 1.0$). For a system with $L_x = L_y = 20$ and $L_z = 30$ at the state point $\eta_{col} = 0.15$ and $\eta_{pol} = 0.4$. (a) In the active case the temperature can be lowered significantly by measuring it with the configurational temperature instead. Still the active particles lead to a higher overall temperature, this is expected as they are still putting energy into the system. (b) For the passive case both methods result in the initial temperature of $T_{init} = 1.0$.

the active case Equation 4.2 is used after each VV update to adjust the velocities depending on the velocities of their neighbouring particles.

In Figure 4.11 and all following initial tests for a thermostat we study a state point in the two phase region of the system. This has the advantage, that we can directly compare whether working thermostats result in the same two points for the phase diagram. Of course, once we find a working thermostat we will still have to calculate the full phase diagram again.

By applying a Langevin thermostat to the active system we get a steady state for our active model. The temperature is clearly above the initial set temperature

of $T_{init} = 1.0$ as can be seen in Figure 4.11(a), nonetheless the clustering effect induced by the Vicsek model can be seen in Figure 4.2.

4.4.2 Lowe-Andersen thermostat

Next we take a look at the so-called Lowe-Andersen thermostat [60]. This thermostat was proposed by Lowe in 1999 and origins from the dissipative particle dynamics (DPD) thermostat which conserves momentum (and thereby hydrodynamics) and enhances viscosity. We construct a list of all pairs of particles for which $r_{ij} < r_c$. Here r_c is a predefined interaction radius for the thermostat analogous to the interaction radius in DPD. For each pair we decide, with a probability $\Gamma\Delta t$, where Γ is a "bath collision" frequency, whether to draw a new relative velocity from a Maxwell distribution to thermalise the system. For each pair of particles whose velocities are to be thermalised we work on the component of the velocity parallel to the line of centres (to conserve angular momentum) and generate a relative velocity $\vec{v}'_{ij} \cdot \hat{r}_{ij}$ from a distribution $\xi_{ij}\sqrt{2k_B T/m}$. To impose this new relative velocity on the particles, and conserve momentum, we update the velocities pairwise:

$$\vec{v}'_i = \vec{v}_i + \vec{\Delta}_{ij} \tag{4.11}$$

$$\vec{v}'_j = \vec{v}_j - \vec{\Delta}_{ij} \tag{4.12}$$

$$\text{with} \quad 2\vec{\Delta}_{ij} = \hat{r}_{ij}\left(\vec{v}'_{ij} - \vec{v}_{ij}\right) \cdot \hat{r}_{ij} \quad . \tag{4.13}$$

Figure 4.12 shows the results obtained with the Lowe-Andersen thermostat. Unfortunately, this thermostat does not lead to a steady state for the active system. Instead the colloids are accelerating, which in turn means the temperature is diverging. While the Lowe-Andersen thermostat conserves momentum, our model of activity does not, thus the thermostat cannot reduce the additional energy put into the system in every simulation step. Even with the other proposed implementations of a Vicsek-like model this thermostat would not work, since alignment rule of the Vicsek model will violate the conservation of momentum.

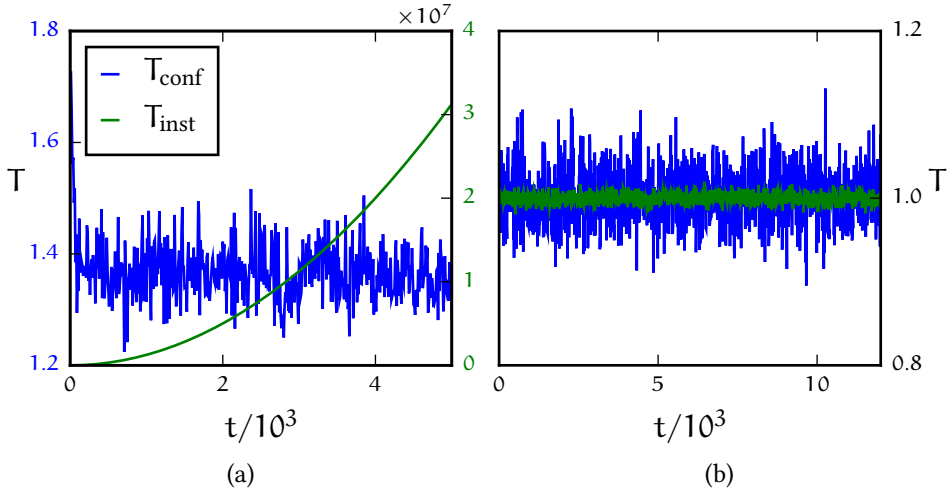

Figure 4.12: Comparison between the active and passive model with the Lowe-Andersen thermostat. At the same state point and system size as for the Langevin thermostat in Figure 4.11. (a) The configurational temperature is even lower than with the Langevin thermostat used before (see Figure 4.11(a)) and approaches the initial temperature of $T_{init} = 1.0$. Unfortunately, the thermostat does not reach a steady state and the kinetic energy diverges, as shown by the green curve. Note that two different y axes are used and the divergence in the kinetic energy is of the order of 10^7 after only a few thousand time steps already, which of course means that we cannot use this thermostat for our studies. (b) For the passive case both methods show the initial temperature of $T_{init} = 1.0$.

4.4.3 Maxwell-Boltzmann thermostat

We test a Maxwell-Boltzmann (MBS) thermostat [61] which explicitly simulates solution particles. The thermostat is based on the multi-particle collision dynamic (MPCD) algorithm [62] which conserves the momentum locally and thereby has hydrodynamic interactions on scales greater than the so-called collision cells. The algorithm can be divided in two different steps:

1. **Streaming step**: The solvent particle positions and velocities are updated by the standard Velocity Verlet algorithm.

$$\vec{r}_i(t+\tau) = \vec{r}_i(t) + \vec{v}_i(t)\tau \tag{4.14}$$

$$\vec{v}_i(t+\tau) = \vec{v}_i(t) \tag{4.15}$$

Note that the solvent particles behave like ideal gas particles, hence they do not interact with each other. $m_s = 0.025 \cdot m_{col}$ is the mass of the solvent particles and τ is the collision time step, which relates to the MD time step Δt as $\tau = I \cdot \Delta t$ with I being a positive integer, which we set to $I = 4$.

2. **Collision step**: The velocities of all solvent particles in each cell are updated by a rotation of their relative velocities:

$$\vec{v}_i = \vec{u} + R(\alpha)\delta\vec{v}_i \quad . \tag{4.16}$$

Here $\vec{u}$ is the mean velocity in the cell, $\delta\vec{v}_i = \vec{v}_i - \vec{u}$ and $R(\alpha)$ is a rotation matrix with angle $\alpha = 90°$ around a randomly chosen rotation axis. In this step the fluid particles (colloids and polymers) are integrated as well. By associating them to the respective solvent cells the mean velocity $\vec{u}$ of the cell is calculated as the mass weighted average of all velocities. This leads to a momentum transfer from the fluid to the solvent. The velocity of the fluid particles is updated in the same way as the velocity of the solvent particles (see equation 4.16). This leads to a momentum transfer from the solvent to the fluid particles. The collision step is the only point the two particle species interact. Until the next collision the fluid particles are treated via the Velocity Verlet algorithm.

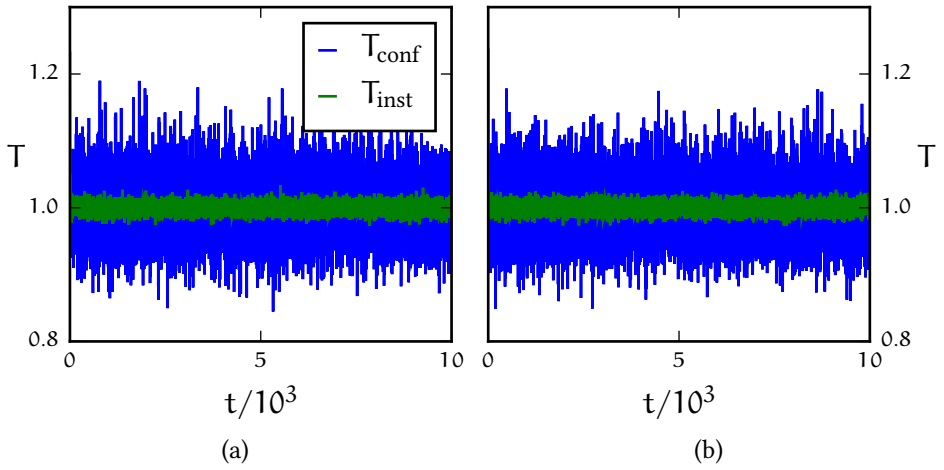

Figure 4.13: Comparison between the two methods to measure the temperature with the Maxwell-Boltzmann thermostat. For a system with $L_x = L_y = 12$ and $L_z = 48$ at the state point $\eta_{col} = 0.15$ and $\eta_{pol} = 0.4$. (a) The configurational temperature as well as the kinetic temperature yield the correct initial temperature of $T_{init} = 1.0$. Also, there is no more difference to the passive case which is shown in (b). A steady state is reached for both, the active and the passive case.

To get the Maxwell-Boltzmann thermostat one has to change the rule in the collision step from before. Instead of only rotating the velocities in the collision step, they are now rotated and rescaled by a factor ξ, which depends on two types of kinetic energies, the relative local kinetic energy of the cell

$E_{kin} = \frac{1}{2}\sum_i m_i(\Delta\vec{v}_i)^2$ and the target local kinetic energy E'_{kin} which is taken from a gamma distribution:

$$P(E'_{kin}) = \frac{1}{E'_{kin}\Gamma(f/2)}\left(\frac{E'_{kin}}{k_B T}\right) e^{-E'_{kin}/(k_B T)} \quad . \tag{4.17}$$

Here f is the number of degrees of freedom of the system and $\Gamma(x)$ is the gamma function. The rescaling factor ξ is then calculated as $\xi = \sqrt{\frac{E'_{kin}}{E_{kin}}}$. During each collision step the particle velocities are then rescaled as $\Delta\vec{v}_i \to \xi\Delta\vec{v}_i$.

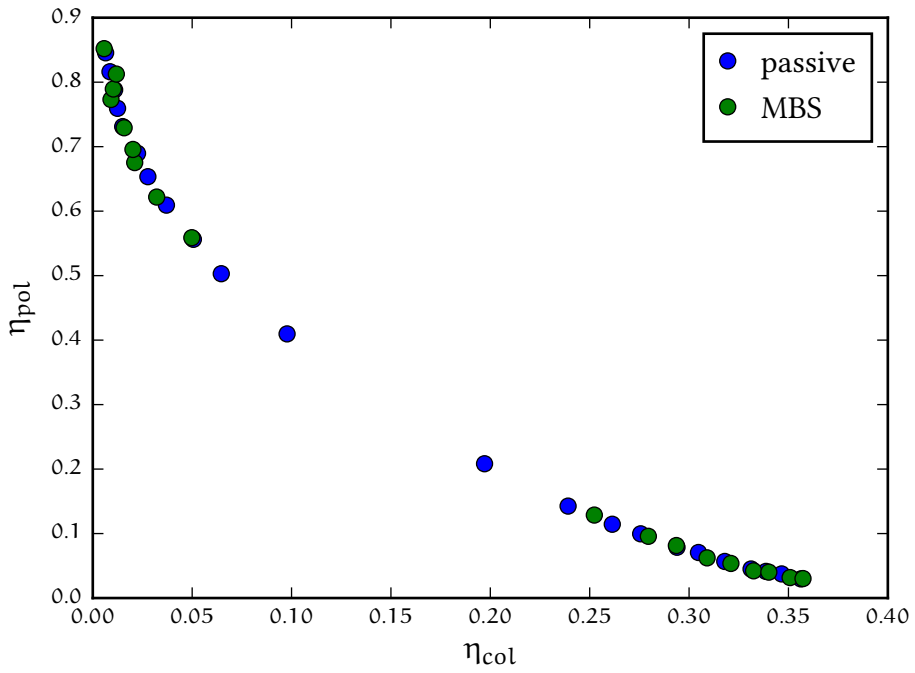

Figure 4.14: Phase diagram of the passive system and the active system ($f_A = 10$) cooled by the Maxwell-Boltzmann thermostat. The clustering effect of the Vicsek-like active particles vanishes and we regain the passive behaviour of the system.

In Figure 4.13 we can see that the thermostat manages to cool the system to the set temperature in both the active and the passive case. However, the thermostat is so rigorous that the effect of the active particles is lost, and we get the same phase diagram as for the passive model as shown in Figure 4.14. Therefore, we cannot use this thermostat either.

4.4.4 Conclusion

We have tested three thermostats to check their effect on the active model. To reach a steady state the thermostat needs to remove energy from the system, which is put in by the constant force of the active Vicsek model. Since this model is not conserving momentum thermostats which do are not working, as was demonstrated in Section 4.4.2 with the Lowe-Andersen thermostat. Also, a thermostat should not destroy the clustering effect of the active particles. In fact a too restrictive thermostat can completely remove any effect the active model might have. An example for this behaviour is the Maxwell-Boltzmann thermostat as discussed in Section 4.4.3. The Langevin thermostat is a fairly simple thermostat which removes heat from the system via a friction term and conserves the local ordering of the active particles. It is the only thermostat we have tested that fulfils the demands of reaching a steady state. There are other thermostats one could try like Berendsen [63], Andersen [64], or Nosé-Hoover thermostat [65], but for this work we will stick with the Langevin thermostat. Note, that for other active models [66–68] or non-equilibrium systems [69] the here discarded thermostats work as intended. We do not discredit those thermostats, but merely state that they do not work for the active system discussed in this work for the above mentioned reasons. Other active models like e. g. active Brownian particles [70–72] include the thermostat in their definition, and for the rest of this thesis we will do the same and state that the active system as defined here uses the Langevin thermostat.

4.5 TEMPERATURE DISTRIBUTION

Figure 4.1 indicates that the active particles carry almost all of the heat. This raises the question as to how this heat is distributed over the phase separated system. To study the temperature distribution of the colloids in our system we use two approaches. In both cases we follow the trajectory of an already phase separated steady state of a system well inside the two phase region. The simulation box is expanded in z direction to enforce the formation of a slab. During each analysis step all particles are shifted in a way that the centre of mass of the colloids coincides with $z = 0$. The velocity of the particles is then recorded in a spatial histogram of the z axis.

In the first approach (compare with Figure 4.15) we use Equation 4.18 to determine an overall temperature histogram.

$$T(z;\alpha) = \frac{2}{3k_B}\left\langle \sum_i^{N_z} \frac{1}{2} m v_{i,\alpha}^2 \right\rangle, \tag{4.18}$$

with N_z being the number of colloids in this bin. If $N_z = 0$ we do not count

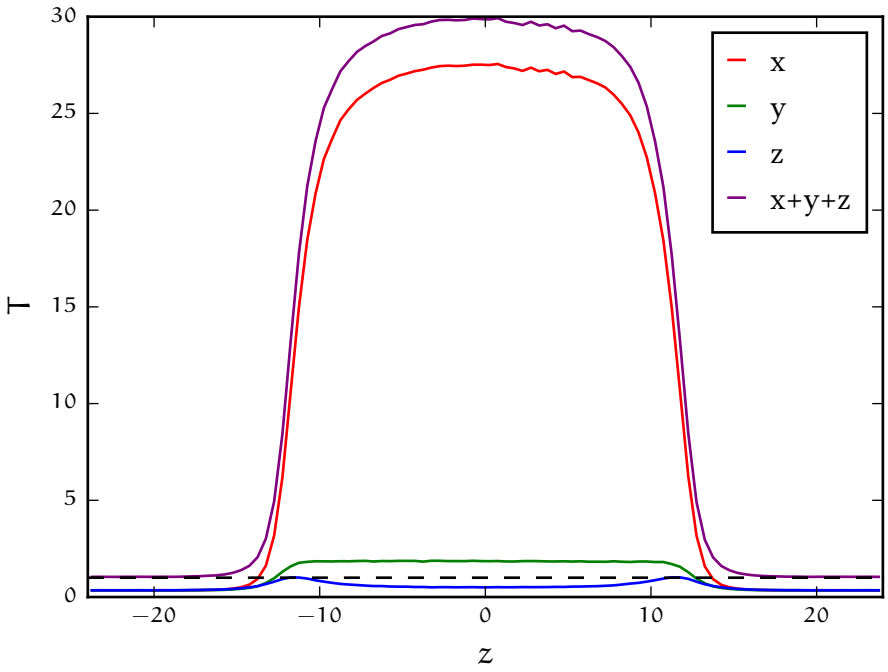

Figure 4.15: Results for the kinetic energy relation as defined in Equation 4.18 for a steady state with $\eta_{col} = 0.15$ and $\eta_{pol} = 0.30$ in a system with $L_x = L_y = 12\sigma$ and $L_z = 48\sigma$. In this plot both particle types are considered, for a representation distinguishing between colloids and polymers see Figure A.1. The colloid slab in this example moves in x-direction. The initial temperature $T_{init} = 1$ is shown by the dashed black line. If we average the temperature over all bins we get $\langle T \rangle = 14.5$.

the bin to the overall statistics. We distinguish each axis α, so that we generate three different histograms. This results in a distribution which shows that the colloid slab carries nearly all the heat of the system, while in the polymer rich phase the temperature is close to the one set by the thermostat. This is to be expected since the energy is pumped into the system via the colloids, therefore the temperature in the colloid gas (or polymer liquid) phase should be lower.

For the second approach we assume that the colloids, which are spatially close to each other, travel in the same direction. The local mean velocity, indicated by $<>_z$, should thus be subtracted as shown in Equation 4.19. This phenomenon

is similar to the flying ice cube effect known from equilibrium MD simulation which is an artefact due to velocity rescaling [73].

$$T(z;\alpha) = \frac{2}{3k_B}\left\langle \sum_i^{N_z} \frac{1}{2} m \left(v_{i,\alpha} - \langle v(\alpha)\rangle_z\right)^2 \right\rangle \tag{4.19}$$

The distribution shown in Figure 4.16 indicates that the clustered colloids travel

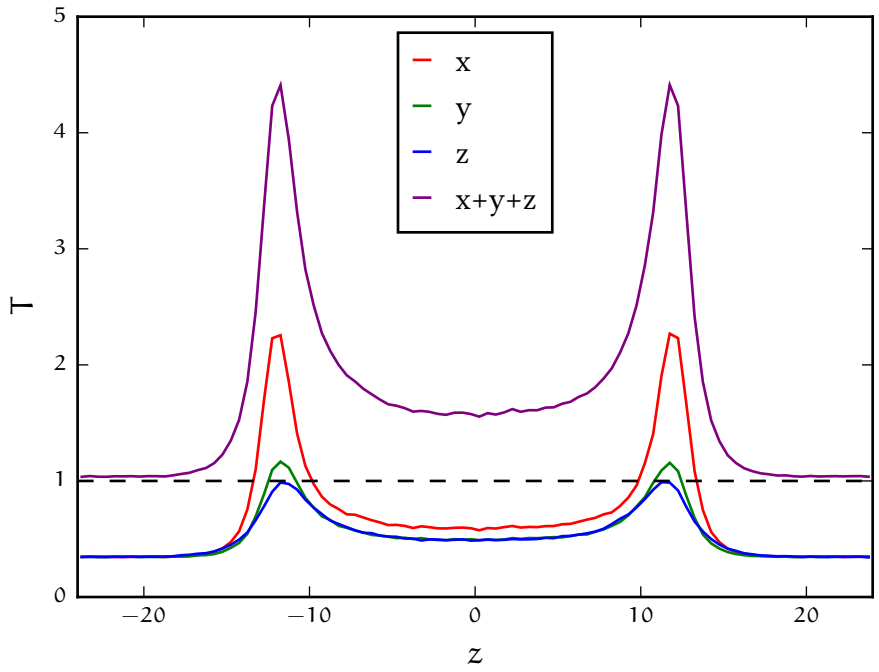

Figure 4.16: Results for the second approach using Equation 4.19 for the same steady state as in Figure 4.15. Again both particle types are treated, while Figure A.1 shows the individual contributions. The initial temperature $T_{init} = 1$ is shown by the dashed black line. If we average the temperature over all bins we get $\langle T\rangle = 1.8$ which is slightly lower than the configurational temperature for the same system: $T_{conf} = 2.2$.

mostly in the same direction so that most of the heat is generated at the interface of the two particle types. Note that the overall temperature is still slightly higher than the initially set temperature of the thermostat but even lower than the configurational temperature. A plot distinguishing the two particle types is shown in the appendix in Figure A.1. It shows that indeed the colloids carry most of the heat and cannot be cooled to the initially set temperature even in the colloid gas phase. The polymers in their dense phase reach $T = 1$. In the colloid rich phase they are dragged along and thus have a higher temperature as well.

4.6 ACTIVE BROWNIAN PARTICLES

A different, more common way to introduce activity into a system is the active Brownian particle (ABP) model. It has recently become of interest in statistical mechanics as a model system that induces phase separation in hard spheres [70–72]. We want to compare this model to the active Vicsek model. Jonathan Siebert has implemented a model for ABPs in our shared simulation code, which we extend to include the polymers as passive Brownian particles. The colloids in our system are then treated as ABPs. In this model the integration scheme has to be changed to an Euler algorithm with a time step of $\Delta t = 2 \cdot 10^{-5}$. The equations of motion are:

$$\dot{\vec{r}}_i = v_A \vec{e}_i + \frac{D_t}{k_B T} \vec{F}_i + \sqrt{2D_t} \vec{R}_1(t) \tag{4.20}$$

$$\dot{\vec{e}}_i = \sqrt{2D_r} \vec{R}_2(t) \times \vec{e}_i \quad , \tag{4.21}$$

where $\vec{e}_i$ is the direction of the particle, $\vec{F}_i$ is the total force on the particle, $D_t = 1$ is the translational diffusion coefficient, $D_r = 3D_t/\sigma_{cc}^2$ is the rotational diffusion coefficient, and $\vec{R}_1$ and $\vec{R}_2$ are zero-mean unit-variance Gaussian white noises. The active velocity v_A is set to $v_A = 0$ for the polymers and $v_A = 10$ for the active colloids. In Figure 4.17 the effect of both models of activity on the phase diagram is compared. While the Vicsek-like activity facilitates phase separation, the active Brownian particle activity hinders it for $v_A = 10$. However this value for the active velocity is far below the typical velocities at which self-trapping occurs [70–72]. For this small active velocity the configurational temperature changes only slightly. A system with $\eta_{col} = 0.15$ and $\eta_{pol} = 0.90$ has a temperature of $T_{conf} = 1.06$, thus the hindrance of phase separation is most likely due to the self-propelled motion of the ABPs. It is possible that higher active velocities lead to an effect similar to self-trapping in this model as well. In fact there could exist a region in which an increase in active velocity v_A induces stronger phase separation. This has been observed for active Brownian particles, even the reentrant of such phases is possible [74]. In [74] the authors show that starting from a phase separated state one can reach a homogeneous state for higher active velocities before entering a phase separated state again for even higher velocities. We have scanned through active velocities starting from $v_A = 10$ up to $v_A = 400$ but have not observed such a behaviour. It should be noted that for $v_A = 400$ the same configuration as before has a temperature of $T_{conf} = 6.6$. This could prevent the phase separation due to the temperature dependence of the underlying cAO model. Therefore, the usage of ABPs is limited in this model, as one cannot tell if the reason for phase separation is dominated by the changed temperature or by the collective motion. For small active veloc-

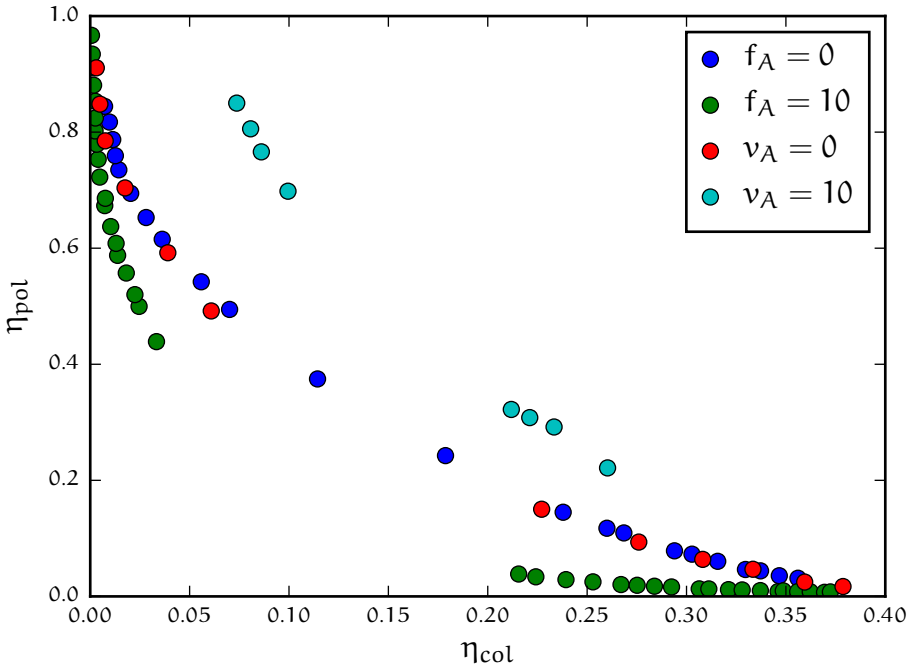

Figure 4.17: Comparison of the Vicsek-like activity (f_A) with the active Brownian particle activity (v_A). The curves with $f_A = 0$ and $v_A = 0$ are the corresponding passive systems. As expected they fall onto the same curve, although there are small deviations in the low colloid region. While the Vicsek model ($f_A = 10$) enhances phase separation the active Brownian particle model ($v_A = 10$) makes phase separation more difficult.

ities we can still summarise that phase separation is hindered because of the self-propelled particles.

5 MAPPING TO A PASSIVE MODEL

In an attempt to understand the phase behaviour of the non-equilibrium model with an equilibrium approach we develop a mapping of the active model onto a passive one using integral equation theory (IET) in [2] and [4]. This procedure is reiterated in this chapter. The IET modelling and calculations have been performed by Sergei Egorov, while the simulations shown have been performed by the author.

5.1 INTEGRAL EQUATION THEORY

5.1.1 Ornstein-Zernike Equation

The Ornstein-Zernike (OZ) equation expresses the total correlation of two particles by the direct correlation of the two combined with an indirect contribution. In the following the equation will be motivated without giving the full derivation, which is beyond the scope of this thesis but can be found in the literature e. g. [75, 76].

We consider a system that interacts via a pair potential $U(|\vec{r}_2 - \vec{r}_1|)$. For simplicity's sake we assume that this potential is homogeneous and isotropic, thus we can write $U(|\vec{r}_2 - \vec{r}_1|) = U(r_{12})$ with $r_{12} = |\vec{r}_2 - \vec{r}_1|$. It makes sense to define the total correlation function of two particles as

$$h(r_{12}) = g(r_{12}) - 1 \quad , \tag{5.1}$$

where $g(r_{12})$ is the radial distribution function.

$$g(r) = \frac{1}{\rho}\langle \sum_{i \neq 0}^{N} \delta(r - r_i) \rangle \tag{5.2}$$

Formally we can then differentiate between the direct and the indirect influence of particle one and two. The direct influence will be written as $c(r_{12})$. The indirect influence involves at least one additional particle three. Therefore, we will write it as the direct influence of particle one with three and the total correlation of particle three with particle two $c(r_{13})h(r_{32})$. Since the position of the third

particle is arbitrary, this effect has to be weighted by the density and averaged over all possible positions. This gives us the OZ equation:

$$h(r_{12}) = c(r_{12}) + \rho \int dr_3 c(r_{13}) h(r_{32}) \quad . \tag{5.3}$$

This equation could now be solved recursively, replacing $h(r_{32})$ by $c(r_{32}) + \rho \int dr_3 dr_4 c(r_{34}) h(r_{42})$ and so on. Instead we replace r_{13} with $r_{12} - r_{32}$ and get

$$h(r_{12}) = c(r_{12}) + \rho \int dr_{32} c(r_{12} - r_{32}) h(r_{32}) \tag{5.4}$$

$$= c(r_{12}) + \rho (c * h)(r_{12}) \quad . \tag{5.5}$$

In Equation 5.5 we used the definition of a convolution. By using the convolution theorem the equation can be written down in Fourier space

$$\hat{h}(k) = \hat{c}(k) + \rho \hat{h}(k) \hat{c}(k) \quad , \tag{5.6}$$

which leads to

$$\hat{h}(k) = \frac{\hat{c}(k)}{1 - \rho \hat{c}(k)} \quad \text{or} \quad \hat{c}(k) = \frac{\hat{h}(k)}{1 + \rho \hat{h}(k)} \quad . \tag{5.7}$$

This means that in order to solve the OZ equation we need to determine $h(r)$ or $c(r)$ (or their Fourier transforms) and thus need an additional equation which is typically referred to as a closure relation.

5.1.2 Ornstein-Zernike Closures

In order to solve the Ornstein-Zernike equation we need to choose a closure relation. Some of the common approximations will be discussed here.

5.1.2.1 Percus-Yevick equation

The density distribution function $g(r)$ can be written as

$$g(r_{12}) = \exp\left[-\beta w(r_{12})\right] \tag{5.8}$$

with $w(r_{12})$ being the potential of mean force, which can be related to the underlying pair potential in the limit of infinite dilution

$$u(r) = \lim_{\rho \to 0} w(r) \quad . \tag{5.9}$$

Alternatively, $g(r)$ can be expressed as a power series of the density ρ

$$g(r_{12}) = \exp\left[-\beta u(r_{12})\right]\left(1 + \sum_{n=1}^{\infty} \rho^n g_n(r_{12})\right) \quad , \tag{5.10}$$

where $\exp\left[-\beta u(r_{12})\right]$ denotes the direct interaction between the two particles one and two. The higher order terms where particle one affects particle two over one or more intermediate particles are weighted by the density ρ.
In Section 5.1.1 we have introduced $c(r_{12})$ as the direct correlation between particle one and two. This means we can formally write

$$c(r_{12}) = g_{\text{total}}(r_{12}) - g_{\text{indirect}}(r_{12}) \quad . \tag{5.11}$$

In Equation 5.11 we substitute $g_{\text{total}}(r_{12})$ by Equation 5.8. To estimate $g_{\text{indirect}}(r_{12})$ we divide $g_{\text{total}}(r_{12})$ from Equation 5.8 by the first Taylor expansion of Equation 5.10 around small ρ, which is the direct interaction. Thus only $g_{\text{indirect}}(r_{12})$ remains and we get an approximation of Equation 5.11 as

$$c(r) = e^{-\beta w(r)} - e^{-\beta\left[w(r)-u(r)\right]} \quad . \tag{5.12}$$

By introducing the functions

$$y(r) = e^{\beta u(r)} g(r) \quad \text{and} \quad f(r) = e^{-\beta u(r)} - 1 \tag{5.13}$$

we can rewrite Equation 5.12 and get the typical notation for the Percus-Yevick (PY) approximation

$$c(r) = g(r) - y(r) = f(r)y(r) \quad . \tag{5.14}$$

If we put this result together with Equation 5.1 back into the OZ equation, Equation 5.3, we get the PY equation

$$\begin{aligned}
& h(r_{12}) && = c(r_{12}) + \rho \int dr_3 c(r_{13}) h(r_{23}) \\
\iff & h(r_{12}) && \overset{5.14}{=} f(r_{12}) y(r_{12}) + \rho \int dr_3 f(r_{13}) y(r_{13}) h(r_{23}) \\
\iff & g(r_{12}) - 1 && \overset{5.1}{=} f(r_{12}) y(r_{12}) + \rho \int dr_3 f(r_{13}) y(r_{13}) h(r_{23}) \\
\iff & y(r_{12}) && \overset{5.13}{=} 1 + \rho \int dr_3 f(r_{13}) y(r_{13}) h(r_{23}) \quad .
\end{aligned} \tag{5.15}$$

This approximation was first introduced by Percus and Yevick [77].

5.1.2.2 Hypernetted-chain equation

For the hypernetted-chain (HNC) equation we start with the same premise as before, but expand g_{indirect} in Equation 5.12 by a Taylor expansion around $w(r) = u(r)$ that we terminate after the first order. Thus we approximate $c(r)$ as

$$\begin{aligned} c(r) &= e^{-\beta w(r)} - 1 + \beta\,[w(r) - u(r)] \\ &\overset{5.13}{=} g(r) - 1 - \ln y(r) \quad . \end{aligned} \tag{5.16}$$

If we insert Equation 5.16 back into the OZ equation, Equation 5.3, we get the HNC equation [75]

$$\ln y(r) = \rho \int dr_3\,[h(r_{13}) - \ln g(r_{13}) - \beta u(r_{13})]\,h(r_{23}) \quad . \tag{5.17}$$

5.1.2.3 Modified Hypernetted-chain equation

The HNC approximation, Equation 5.16, can be extended by an unknown function $d(r_{12})$ to make it exact [78].

$$c(r) = g(r) - 1 - \ln y(r) + d(r) \tag{5.18}$$

The solution of Equation 5.18 for a potential $u(r) - \frac{1}{\beta} d_i(r)$ gives us the exact $g(r)$ for a potential $\phi(r) \approx u(r) + \frac{1}{\beta}\,[d(r) - d_i(r)]$, where $d(r)$ is the exact function and $d_i(r)$ is an assumed function (e. g. $d_i(r) = 0$ as in the HNC approximation). We know that the radial distribution function is proportional to

$$g_{d_i}(r) \propto \int \exp\left[-\beta u(r) + d_i(r)\right] dr \tag{5.19}$$

and thus if $d_i(r) > d_j(r)$ it directly follows that $g_{d_i}(r) > g_{d_j}(r)$. With this we can deduce that

$$\int \left[g_{d_i}(r) - g_{d_j}(r)\right]\left[d_i(r) - d_j(r)\right] dr \geqslant \epsilon \sim 0 \tag{5.20}$$

$$\int \Big[g_{\text{exact}}(r) - g_{\text{est}}(r)\Big]\Big[d_{\text{exact}}(r) - d_{\text{est}}(r)\Big]\,dr \geqslant \epsilon \sim 0 \quad . \tag{5.21}$$

Equation 5.21 can now be used to iteratively increase the accuracy of function $d_{est}(r)$ if both radial distribution functions g_{exact} and g_{est} are known. This procedure is called the modified HNC approximation [78].

5.2 BOLTZMANN INVERSION

In Section 5.1 we have discussed how a correlation function (e. g. the radial distribution function) can be constructed via an integral equation theory. For that

we solve the OZ equation together with a chosen closure relation and get the total correlation function which is related to the radial distribution function by Equation 5.1.

In an attempt to map the active model onto a passive model consisting of only pair potentials, we have now to perform an inversion to get from the calculated correlation function back to a pair potential. A well-known method for this is the so-called iterative Boltzmann inversion (IBI) [79]. Here we iteratively adjust the pair potential $U_i(r)$ to fit the calculated $g_i(r)$ to the "real" (simulated) radial distribution function $g_{sim}(r)$

$$U_{i+1}(r) = U_i(r) - \alpha k_B T \ln\left[\frac{g_i(r)}{g_{sim}(r)}\right] \quad , \tag{5.22}$$

where α is a damping factor smaller than one. As an initial guess for Equation 5.22 we can use

$$U_0(r) = -k_B T \ln[g_{sim}(r)] \quad . \tag{5.23}$$

The IBI approach can be state point dependent, and is improved by a multistate IBI algorithm [80]. For that we put in additional data in form of radial distribution functions at other state points, and average over the N states we use. The resulting iterative algorithm is then:

$$U_{s,0}(r) = -\frac{1}{N}\sum_s k_B T_s \ln[g^s_{sim}(r)] \tag{5.24}$$

$$U_{s,i+1}(r) = U_{s,i}(r) - \frac{1}{N}\sum_{s=1}^{N} \alpha_s(r) k_B T_s \ln\left[\frac{g^s_i(r)}{g^s_{sim}(r)}\right] \quad , \tag{5.25}$$

where s is the number of the state and $\alpha_s(r)$ is a state dependent damping factor.

5.3 EFFECTIVE POTENTIALS

5.3.1 Estimation of the radial distribution functions

We determine the radial distribution functions $g_{sim}(r)$ of all interactions far from the critical point in the homogeneous region and use the OZ equation 5.7 to relate these pair correlations to the total correlation functions. These relations with the OZ equations are exact but for the closure functions. In case of the here discussed active system both the colloid-colloid and the colloid-polymer potentials are highly repulsive and diverge for small distances, while the polymer-polymer potential converges to a fixed value at $r = 0$. This makes this system

highly asymmetric and there is no default way to choose the closure in such a system. Therefore, several different known closures where tested: hypernetted-chain (HNC), modified HNC, Percus-Yevick (PY) and thermodynamically consistent Rogers-Young closure [75, 77, 78, 81]. We then choose the empirically best working closure for each pair correlation by comparing the results with the simulated radial distribution function of the interaction. For the colloid-colloid potential we use the modified HNC closure, the colloid-polymer and polymer-polymer OZ equations are closed by a PY closure.

5.3.2 Inversion to find the effective potentials

The resulting radial distribution functions are inverted via the iterative Boltzmann inversion [80] as discussed in Section 5.2. Here we use the simulated radial distribution functions $g_{sim}(r)$ as "target" and iteratively adjust the effective potentials until the difference between IET calculated $g_{IET}(r)$ and simulated is minimised. This has been done by using only the simulation data from one state point [79] as well as with several different state points [80] to test the robustness of this approach. In Figure 5.1 the resulting radial distribution functions are compared to the originally measured ones, other state points are shown in the appendix in Figures A.2 and A.3. It is difficult to match all radial distribution functions. Therefore, we choose to put the emphasis on the colloid-colloid and colloid-polymer interactions, as we expect them to be the responsible interactions for the influence of the activity, while the polymer-polymer interaction is only changed indirectly by the active colloids. Still the polymer-polymer distribution function deviates clearly from g_{pp}^{sim} (Figure 5.1) and the deviation increases with increasing polymer concentration (Figures A.2 and A.3). We can therefore expect that the resulting passive potential will not give the same results as the active system for higher polymer concentration.

5.3.3 Results for the IET potential

With the IET approach it is possible to replace the colloid-colloid as well as the colloid-polymer interaction by effective now passive potentials as shown in Figure 5.2.

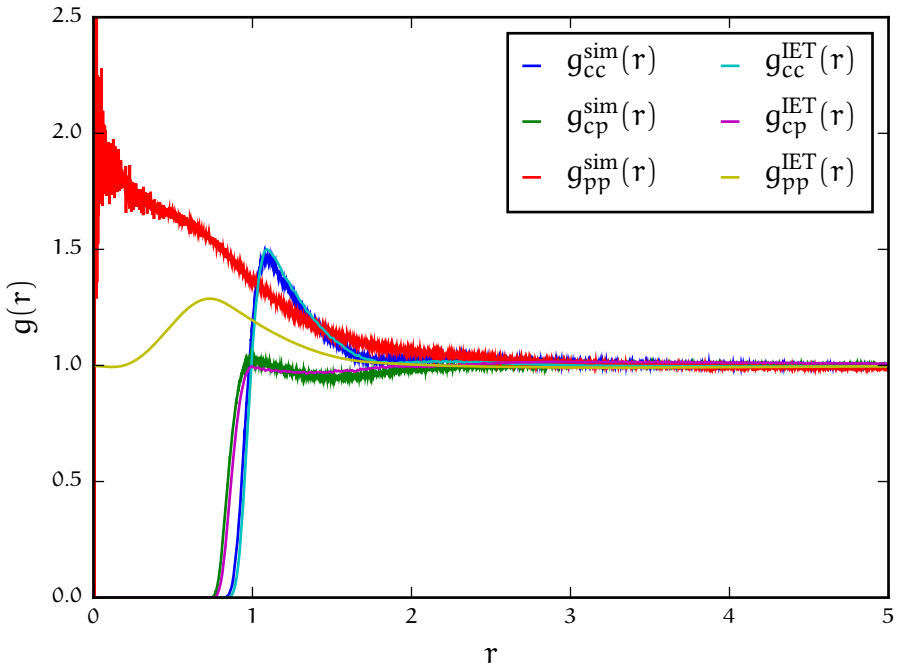

Figure 5.1: The radial distribution function $g(r)$ for a state point with $\eta_{col} = 0.10$ and $\eta_{pol} = 0.05$ as measured by simulating the active system (sim) and as estimated by IET calculations (IET) for the colloid-colloid (cc), colloid-polymer (cp) and polymer-polymer (pp) interaction. The radial distribution functions obtained from simulation and IET agree nicely for the colloid-colloid and colloid-polymer interaction. The not matched g_{pp}^{IET} differs clearly from the simulation.

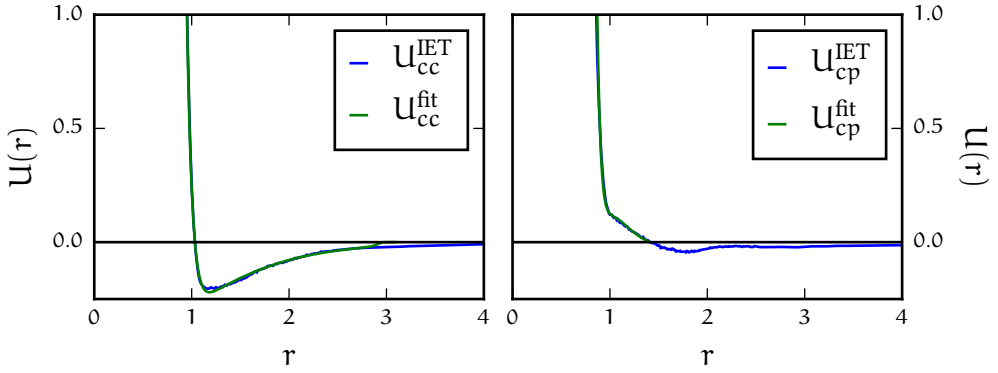

Figure 5.2: The potentials obtained via IET calculations are shown together with their respective fit. The colloid-colloid interaction is cut-off at $r_{cc} = 3$, while the colloid-polymer potential, is cut-off at the first crossing of the x-axis. Since the attraction between colloids and polymers for longer range is most likely an artefact of the inversion. $U_{cc}^{fit}(r)$ is defined in Equation 5.26, $U_{cp}^{fit}(r)$ in Equation 5.27.

$$
\begin{aligned}
U_{cc}^{fit}(r) = \epsilon_{cc} \cdot \Bigg[& \\
& 11.8164 \cdot \left(\frac{\sigma_{cc}}{r}\right)^{12} - 118.642 \cdot \left(\frac{\sigma_{cc}}{r}\right)^{10} \\
& +318.727 \cdot \left(\frac{\sigma_{cc}}{r}\right)^{9} - 392.529 \cdot \left(\frac{\sigma_{cc}}{r}\right)^{8} \\
& +240.715 \cdot \left(\frac{\sigma_{cc}}{r}\right)^{7} - 59.8517 \cdot \left(\frac{\sigma_{cc}}{r}\right)^{6} \\
\Bigg] & \cdot \frac{(r - r_{cc})^4}{10^{-4} + (r - r_{cc})^4}
\end{aligned} \tag{5.26}
$$

$$
\begin{aligned}
U_{cp}^{fit}(r) = \epsilon_{cp} \cdot \Bigg[& \\
& 27.9968 \cdot \left(\frac{\sigma_{cp}}{r}\right)^{12} - 304.967 \cdot \left(\frac{\sigma_{cp}}{r}\right)^{10} \\
& +707.509 \cdot \left(\frac{\sigma_{cp}}{r}\right)^{9} - 707.090 \cdot \left(\frac{\sigma_{cp}}{r}\right)^{8} \\
& +343.246 \cdot \left(\frac{\sigma_{cp}}{r}\right)^{7} - 66.5698 \cdot \left(\frac{\sigma_{cp}}{r}\right)^{6} \\
\Bigg] & \cdot \frac{(r - r_{cp})^4}{10^{-8} + (r - r_{cp})^4}
\end{aligned} \tag{5.27}
$$

With $\sigma_{cc} = \sigma_{cp} = \epsilon_{cc} = \epsilon_{cp} = 1$, $r_{cc} = 3.0$ and $r_{cp} = 1.41213$. The polymer-polymer interaction remains unchanged (see Equation 3.3). The potentials compared to the formerly used ones can be seen in Figure 5.3. The colloid-polymer interaction becomes more repulsive, this can be seen in the increasing Barker-Henderson diameter $d_{cp}^{fit} \approx 0.9193$ as well. The colloids are now attractive for other colloids and their Barker-Henderson diameter is getting smaller $d_{cc}^{fit} \approx 0.9648$. The clustering of the colloids is therefore enhanced and we expect sharp interfaces, due to the repulsive nature of the colloid-polymer interaction. Note, that we do not actually do any adjustments to the Barker-Henderson diameters, but leave them as they were for the active model since these are the values the mapping was done for. The here calculated diameters are just to quantify the changes in the potentials.

The fitted potentials differ slightly from the calculated potentials using IET (compare with Figure 5.2). Therefore, we once again compare the effective potentials to the actual potentials by calculating the radial distribution functions. The results can be seen in Figure 5.4 and for different state points in the appendix Figures A.4 and A.5. The agreement is very good for the first peek in the radial distribution function. For higher distances slight deviations are visible. It is noteworthy that g_{pp} agrees for both methods, while no change was introduced to the polymer-polymer potential compared to Figure 5.2.

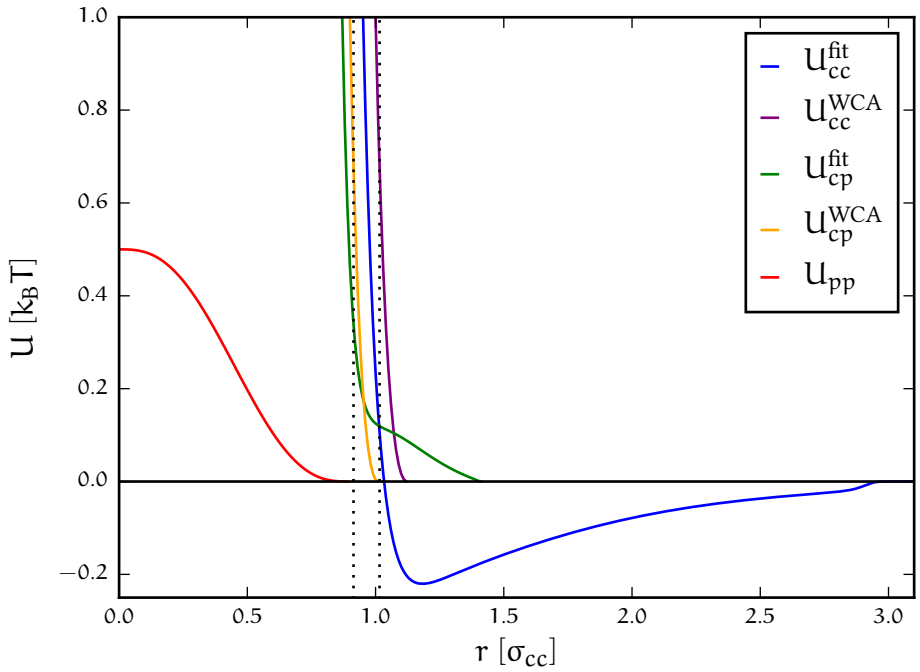

Figure 5.3: Plot of the fitted potentials obtained from IET where cc stands for the colloid-colloid, cp for the colloid-polymer and pp for the polymer-polymer interaction. The original WCA potentials are shown for comparison (purple, orange). The Barker-Henderson diameter d_{cc} of the original potential U_{cc}^{WCA} and $0.9\ d_{cc}$ are shown as dotted lines.

5.4 PHASE DIAGRAMS

From the analytically determined radial distribution functions the structure factors can be determined as

$$S_{\alpha\beta}(\vec{k}) = 1 + \rho \int e^{i\vec{k}\cdot\vec{r}} g_{\alpha\beta}(\vec{r}) d\vec{r} \quad , \tag{5.28}$$

where α and β stands for c or p. At the spinodal line, the line at which spontaneous phase separation occurs, the structure factors diverge for $k = 0$, thus $S_{\alpha\beta}^{-1}(\vec{k} = \vec{0}) = 0$. Therefore, we determine the spinodal line by starting from a certain colloid packing fraction and increasing the number of polymers until all three structure factors are equal to zero. The spinodal line is always above the binodal (phase diagram) except at the critical point where they have the same value.

Alternatively, we can use the fitted potentials to determine the phase diagrams with MD simulations. Here we can either choose to use the fitted colloid-colloid interaction only or use both fits together. A comparison of the resulting phase diagrams can be seen in Figure 5.5. The effective potentials overestimate the at-

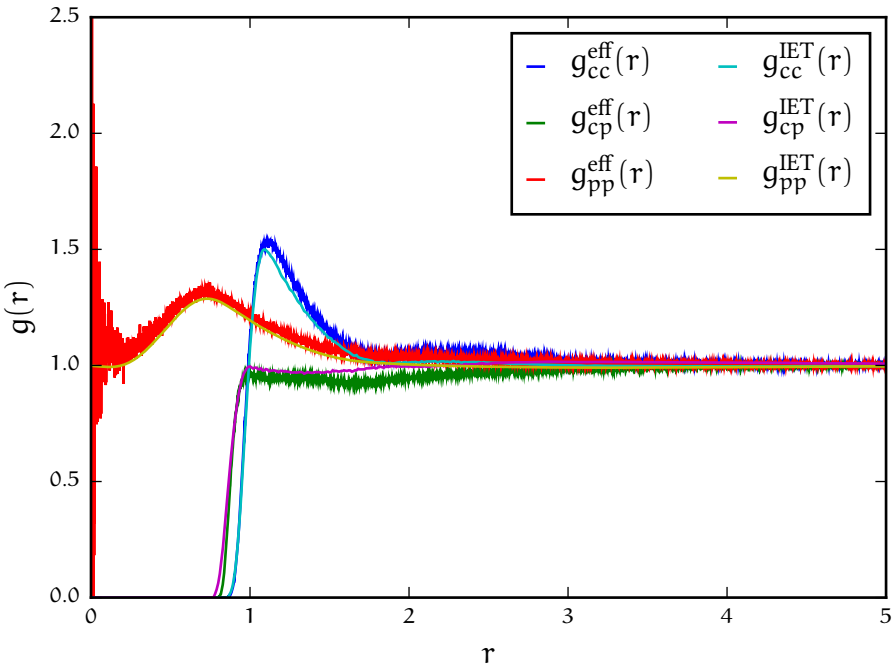

Figure 5.4: The radial distribution function $g(r)$ for a state point with $\eta_{col} = 0.10$ and $\eta_{pol} = 0.05$ as measured by simulating with the effective potentials (eff) and the active model (sim) for the colloid-colloid (cc), colloid-polymer (cp) and polymer-polymer (pp) interaction.

tractive effect of the Vicsek model regardless of which version we look at (IET, only u_{cc}^{eff}, or $u_{cc}^{eff} + u_{cp}^{eff}$). However, the constructed potentials give consistent results in a way that they all seem to be reasonably similar to each other. In the colloid-rich side of the phase diagram the active system overlaps nicely with both mappings. The differences between the active and the mapped passive potentials are directly correlated to the differences between the estimated and the simulated radial distribution functions, which cannot be neglected. Especially for the polymer-polymer interaction we get large differences for small distances. This induces an uncertainty into the left arm of our phase diagrams where the polymer concentration tends to be high. Another reason that the active phase diagram is not properly reproduced is that the Vicsek model introduces more than pair wise interaction while the IET approach tries to approximate the clustering effect with only pair potentials. This means, that with all constructed potentials we expect to be in the 3D Ising universality class, when studying the system via simulations, while the active system might belong to another universality class if at all.

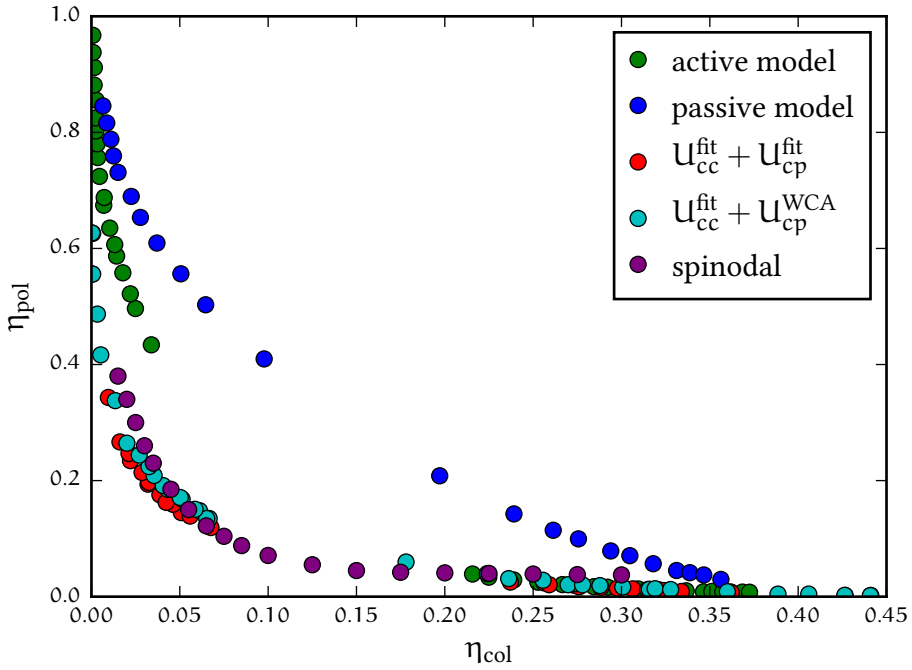

Figure 5.5: Comparison of the resulting phase diagrams. The spinodal calculated via IET is shown in purple. The related, passive MD simulation results are shown in red and cyan for the fitted potentials. The effect of the colloid-polymer interaction on the phase diagram is minor, as the red and cyan points differ only slightly. However, while the red points are consistently below the purple ones, as expected, the cyan points intersect in both branches. The IET potentials phase separate too fast compared to the "real" active system (green).

6 DETERMINING THE CRITICAL POINT IN EQUILIBRIUM SYSTEMS

Before we determine the critical point of the active system, we need to devise the methods to do so and confirm that they are working. For that we will look at a test system in equilibrium where we have literature values for the critical point and know the universality class. However, we will keep the limitations of the active system in mind, so that we can then extend the methods to non-equilibrium.

The first problem is that we do not know the universality class and therefore the critical exponents. This means we have to determine the critical point without knowledge of the universality class. The second problem is that while for the grand canonical (μVT) ensemble the finite size scaling as described in Section 2.3.5 gives a reliable method to determine the critical point, our active model can only be simulated in the canonical (NVT) ensemble.

6.1 BLOCK DISTRIBUTION ANALYSIS

One approach to determine the critical point for equilibrium systems in a NVT ensemble is the so-called block distribution analysis [82–85]. A sketch of this method can be seen in Figure 6.1. Here we divide our big, cubic NVT system

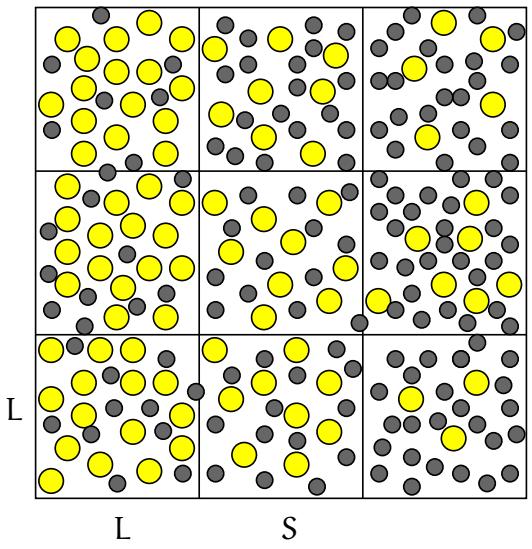

Figure 6.1: Sketch of the block distribution method in two dimensions. The NVT simulation box with length S is divided into $N^2 = 9$ subboxes. In each of the subboxes with area L^2 one can calculate the particle numbers and thus the packing fraction each step. Here the yellow spheres represent the slightly larger colloids and the black spheres depict the polymers.

with length S by an integer N in many small, cubic systems with length L. In these subboxes the particle number is allowed to fluctuate, which results in a "quasi" μVT ensemble. Each of these small systems has its own density ρ_i from which we can determine the first moments to calculate the Binder cumulant:

$$m^2 = \frac{1}{N^3} \sum_i (\rho_i - \bar{\rho})^2 \tag{6.1}$$

$$m^4 = \frac{1}{N^3} \sum_i (\rho_i - \bar{\rho})^4 \tag{6.2}$$

$$U_N = \frac{\langle m^4 \rangle}{\langle m^2 \rangle^2} \quad . \tag{6.3}$$

The value of $\bar{\rho}$ is a constant given by the complete NVT system. As all particles have to be in a subbox this implies for the densities of the subboxes $\bar{\rho} = \frac{1}{N^3} \sum_i \rho_i$. Note that in Equations 6.1 and 6.2 the moments are already averaged over all subboxes while in Equation 6.3 the average is calculated over independent simulation snapshots [84, 85]. With this method the same NVT trajectory can be used to compute all subbox systems simultaneously. This reduces the computation time substantially.

To test the implementation and get a feeling for the method, we use it on a cut and shifted Lennard-Jones system (Equation 6.4) similar to [85, 86].

$$U_{LJ}(r) = \begin{cases} 4\epsilon \left[\left(\frac{\sigma}{r}\right)^{12} - \left(\frac{\sigma}{r}\right)^{6} + \frac{127}{16384} \right] & , r < 2 \cdot \sqrt[6]{2}\sigma \\ 0 & \text{otherwise} \end{cases} \tag{6.4}$$

In [85] Watanabe et al. used simulation boxes as big as $S = 128\sigma$ to determine the critical point. In this model the critical point is expected to be at $T_c = 0.999$ and $\rho_{crit} = 0.320$ [86]. Since our active particle simulation is already time consuming we are rather interested in how much smaller we can choose the simulation box while still determine the critical point with reasonable accuracy. In a two dimensional Lennard-Jones system already 4096 particles were enough to determine the critical temperature with good precision [84]. Therefore, we choose $S = 24\sigma$ and simulate the system along its rectilinear diameter.

$$\frac{1}{2}(\rho_{gas} + \rho_{liquid}) = a \cdot T + b \tag{6.5}$$

The coexistence densities of this well studied system are known and taken from [86]. As the critical density is around $\rho_{crit} \approx 0.3$, this corresponds to roughly the same number of particles as in the two dimensional system from Rovere et al. [84].

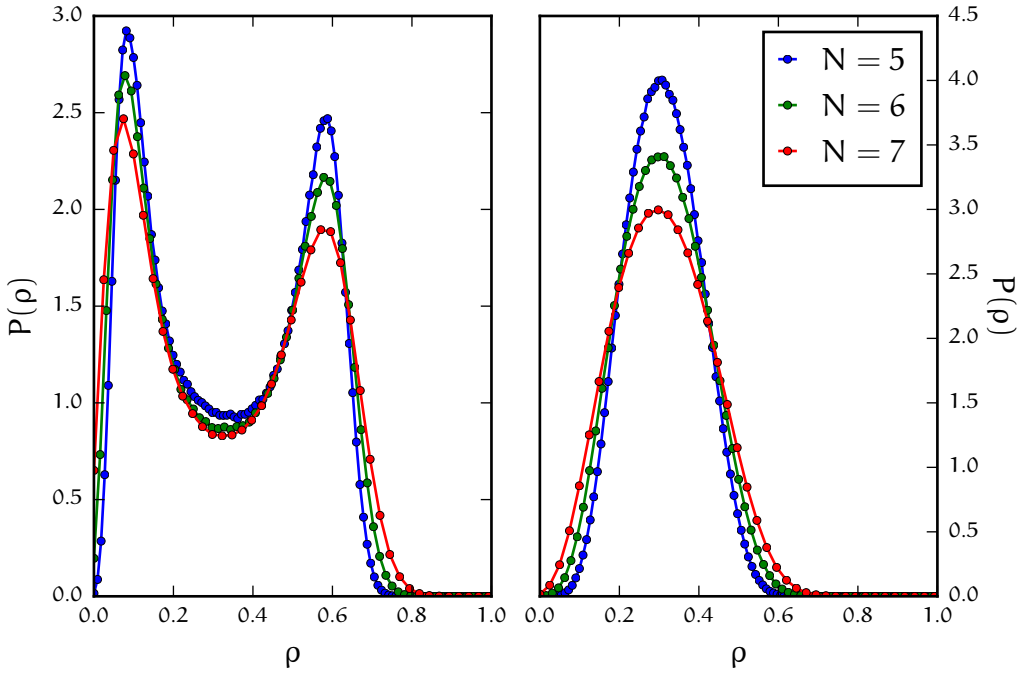

(a) $T = 0.900$ (b) $T = 1.050$

Figure 6.2: Density distribution for different subbox sizes (a) below and (b) above the critical temperature. The probability is normed so that the integral over the curve is one.

In Figure 6.2 two density distributions at different temperatures around the critical point are shown. For $T < T_c$ a double peak in the density distribution is seen, while for $T > T_c$ a single peak remains.

For the analysis one has to select the subbox sizes. In [84] the authors estimate that the subbox size L should be chosen in a way that $\xi \ll L \ll S$, where ξ is the correlation length and thus a priori unknown but constant. Unfortunately, there is no direct way to choose the correct subbox sizes. Surely, the remaining subbox volume should not be too small, since the fluctuation of the density, if one particle more or less is in the subbox, is getting bigger. Thus, the resolution of the density is effectively reduced and the distribution becomes Poissonian instead of Gaussian. On the other hand the subbox should not be too big, as there are too few subboxes then and the correlation between them is increasing. Therefore, the overall explored phase space gets to narrow and thus the μVT ensemble is not properly studied. Also, it will take very long for an individual particle to leave the subbox. Therefore, we choose the subbox sizes empirically, by only using subboxes that show the correct behaviour far from the critical point. In this model this means that for temperatures $T \ll T_c$ the smallest subbox has to have the largest value for the cumulant and the biggest subbox the

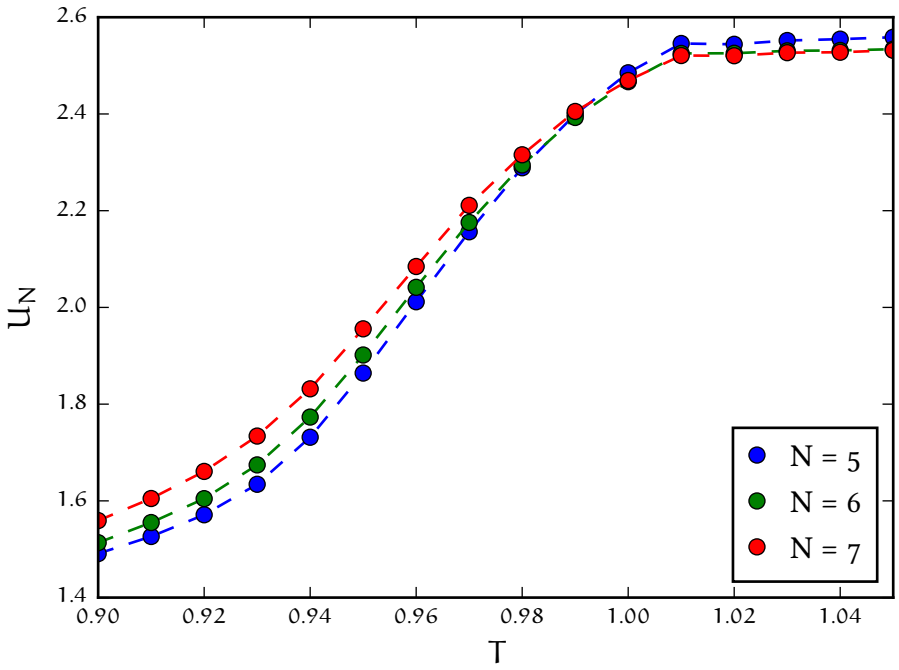

Figure 6.3: Cumulant intersection of the block-distribution method on a cubic simulation with $S = 24\sigma$ over a broad temperature range. The dotted lines are guide to the eye.

lowest, whereas the behaviour switches for temperatures $T \gg T_c$. With this criteria we choose to use the subboxes with $N = 5, 6, 7$. This corresponds, at a density of $\rho = 0.32$, to an average number of $13 - 35$ particles in each subbox. In Figures 6.3 and 6.4 it can be seen that the behaviour far from the critical point is as predicted.

In Figure 6.3 the crossing of the cumulants for different subbox sizes can be seen. However, in Figure 6.4 it is evident that the three cumulants do not cross in one point. Potential reasons include:

- Fluctuations of the temperature because of the thermostat. It is possible to switch the thermostat off and simulate the system in the NVE ensemble to reduce this error [85], but since we will not be able to do this for the active model, we neglected it.

- Fluctuations because of the low amount of particles inside a subbox due to the small size of these subboxes ($L_{N=7} \approx 3.4\sigma$, $L_{N=6} = 4.0\sigma$, $L_{N=5} = 4.8\sigma$). For the active system we try to address this problem by simulating a bigger NVT system.

Still we get an approximation of the critical point by taking the mean of all three intersections, which results in $T_c = 0.994(9)$. This is reasonably close to the lit-

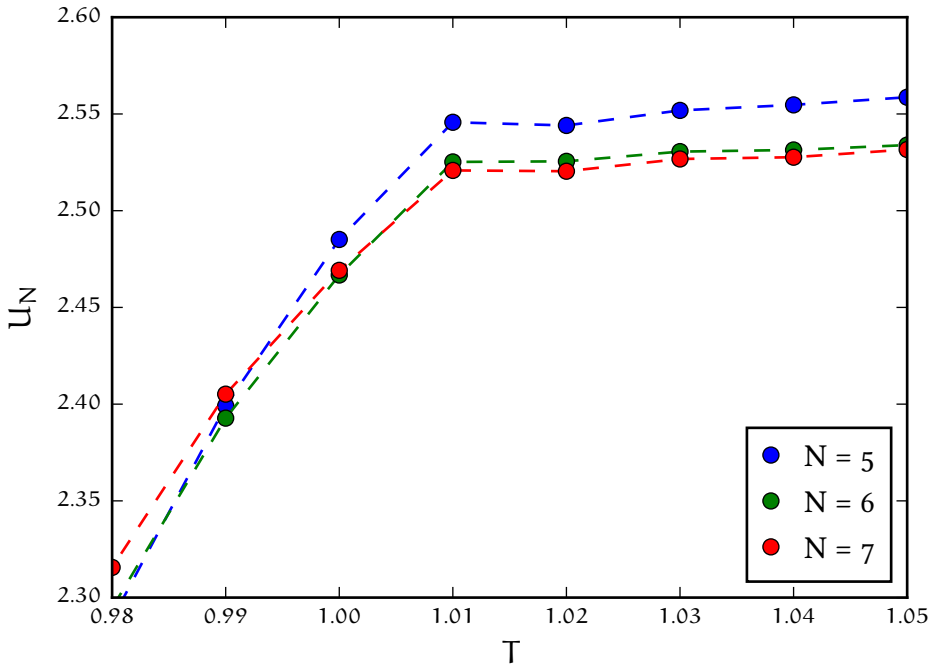

Figure 6.4: Zoom into the relevant part of the cumulant intersection. The red curve lies indeed beneath the green curve after their crossing. In this zoom it is obvious that the three cumulants do not cross in one point. From the three crossings the critical temperature $T_c = 0.994(9)$ can be determined which is in good agreement with the literature value of $T_c = 0.999$ [86].

erature value of $T_c = 0.999$ [86]. Note that the value of the critical cumulant U_{crit} is not the value one would obtain from a grand canonical simulation of a system belonging to the 3D Ising universality class. Since the boundary conditions are no longer periodic for the subboxes, a change is expected. Similar differences to the cumulant were observed in [87] for a two dimensional Ising system and in [85] for a slightly different three dimensional Lennard-Jones system.

6.2 DETERMINATION OF THE COEXISTENCE DENSITIES

In the previous section we have discussed a method to determine the critical point, if the coexistence densities are known. Unfortunately, we do not know the coexistence densities, or rather packing fractions, of the active system. We could use the rule of equal area under the density distribution curve to check if we are already at the correct density or in which direction we have to adjust the simulation. This has been done exemplary for the data shown in Figure 6.2. Here, we would determine the coexistence densities as shown in Table 6.1. The errors are determined as the distance to the next bin of the density distribution and are

T	$\rho_{N=5}$	$\rho_{N=6}$	$\rho_{N=7}$	ρ_{lit}
0.900	0.344(9)	0.34(2)	0.35(2)	0.341
1.050	0.307(9)	0.31(2)	0.30(2)	0.311

Table 6.1: Coexistence densities calculated with the equal area method for Figure 6.2. The literature values are taken from [86].

thus depending on the size of the subbox. The results are in good agreement with the literature. However, a method where the error can be reduced by statistics would be preferred.

In [88] Kim et al. have shown that the coexistence densities of a system can be determined from grand canonical simulations without knowledge of T_c or the universality class. The authors use a finite size parameter Q_L as in Equation 6.6, which is the inverse cumulant. L is the size of the cubic subbox.

$$Q_L = \frac{1}{U_L} = \frac{\langle m^2 \rangle_L^2}{\langle m^4 \rangle_L} \tag{6.6}$$

In the limit of $L \to \infty$ the finite size parameter $Q_L \to \frac{1}{3}$ in a single phase region and $Q_L \to 1$ at coexistence. The coexistence density is given by the position of the maximal Q_L.

We extend this idea to the block distribution method and apply it to the Lennard-Jones test system for different temperatures. In Figure 6.5 the functional dependence of Q_L can be seen. As predicted, $Q_L \to \frac{1}{3}$ for high densities as the sys-

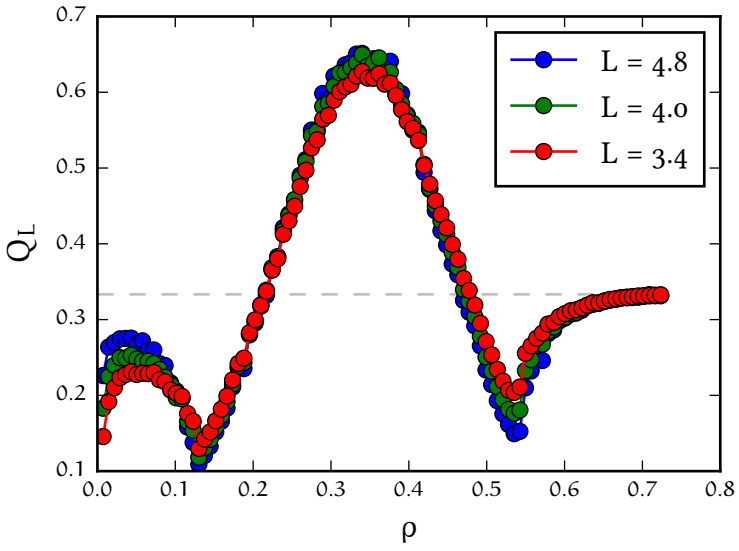

Figure 6.5: Q_L of various densities for a Lennard Jones system at $T = 0.900$.

tem phase separates. For small densities the same behaviour is expected but not reached. This is due to the fact that the subboxes are nearly all empty. At a density $\rho = 0.01$ we have only 138 particles in the simulation box which have to be distributed over $125 - 343$ subboxes. This uncertainty for low density is also seen in μVT simulations [88]. The maximum value for all three subboxes is at a density $\rho = 0.340(7)$ which is close to the literature value of $\rho_{lit} = 0.341$ [86]. We have done a similar analysis at other temperatures which can be seen in Table 6.2. The agreement has to be appreciated. For this method the error is

T	ρ_{coex}	ρ_{lit}
0.900	0.340(7)	0.341
0.930	0.33(1)	0.334
0.997	0.324(4)	0.321
0.999	0.321(1)	0.320

Table 6.2: Coexistence densities calculated from the described method compared to the literature values in [86] determined by grand canonical simulations.

depending on the step size with which the overall number of particles is modified to reach the next density. Thus, the coexistence density can be determined with the same resolution in each subbox.

With these two methods combined we could now calculate the critical point of the Lennard-Jones test system without knowledge of the universality class of the system, or the coexistence densities. One would first determine the rectilinear diameter by determining the coexistence densities for different temperatures as in Table 6.2 and then determine the cumulant intersection as in Figure 6.3.

7

DETERMINING THE CRITICAL POINT IN NON-EQUILIBRIUM SYSTEMS

The determination of the critical point in a non-equilibrium system is quite difficult. For systems under shear one finds that the system changes its behaviour to mean field [89, 90]. For active particles, to our knowledge, only in the classical Vicsek model the critical point has been determined successfully [28, 91]. It should be noted that this was a heavily discussed issue, and the continuous phase transition from unordered to ordered state was questioned [92]. It was later shown that the way the noise is implemented in the classical Vicsek model can change the order of the phase separation [93, 94]. For the determination of the critical point numerous simulations at different system sizes, densities and noise values had to be performed. In other models the critical point in the active case turned out to be at infinite density and could thus not be determined directly via simulation [95].

The way we have introduced the active Vicsek model has the advantage that even the passive model already has a phase transition, which we know is of second order. Since the active model is then imposed on top of this, the transition is likely shifted but expected to be of second order as well. However, this model is computationally more complex to simulate. Therefore, to determine the critical point, we apply the discussed methods from Chapter 6. It should be noted that the methods discussed here apply not only to this model, but could be used on any active or passive model that features a second order phase transition. Jonathan Siebert is currently analysing the active Brownian particle (ABP) model using techniques described in this section and the results look promising.

In this chapter we will determine the critical point of the active system. As mentioned above, this task is quite difficult, and the determination was done with an iterative approach. In the following we will reiterate the performed steps. Starting from a simulation along the rectilinear diameter as determined from the phase diagram we get an estimate for $\eta_{\text{col}}^{\text{crit}}$ and $\eta_{\text{pol}}^{\text{crit}}$. We then correct the estimation for $\eta_{\text{pol}}^{\text{crit}}$, under the assumption that $\eta_{\text{col}}^{\text{crit}}$ is correct, from independent simulations in the homogeneous phase. In further independent simulations $\eta_{\text{pol}}^{\text{crit}}$ is determined from the cumulant intersection that goes through the estimated critical point. Finally, we show that the extrapolations from the homogeneous

phase to the correct η_{pol}^{crit} result, within the error, in the same η_{col}^{crit} that was originally determined.

7.1 SIMULATIONS ALONG THE RECTILINEAR DIAMETER

It has been shown that the law of rectilinear diameter applies to the passive cAO model [96]. For now we assume

$$\frac{1}{2} \cdot (\eta_{pol}^{gas} + \eta_{pol}^{liquid}) = \frac{a}{2} \cdot (\eta_{col}^{gas} + \eta_{col}^{liquid}) + b \quad . \tag{7.1}$$

In Figure 7.1 the fit is shown for the phase diagram of the active system. We estimate the slope to be $a = 3.84(2)$. Note that it is an assumption that our active system follows a law of rectilinear diameter and that we do not aim to prove this here, we just use it as an estimate for the coexistence packing fractions for now.

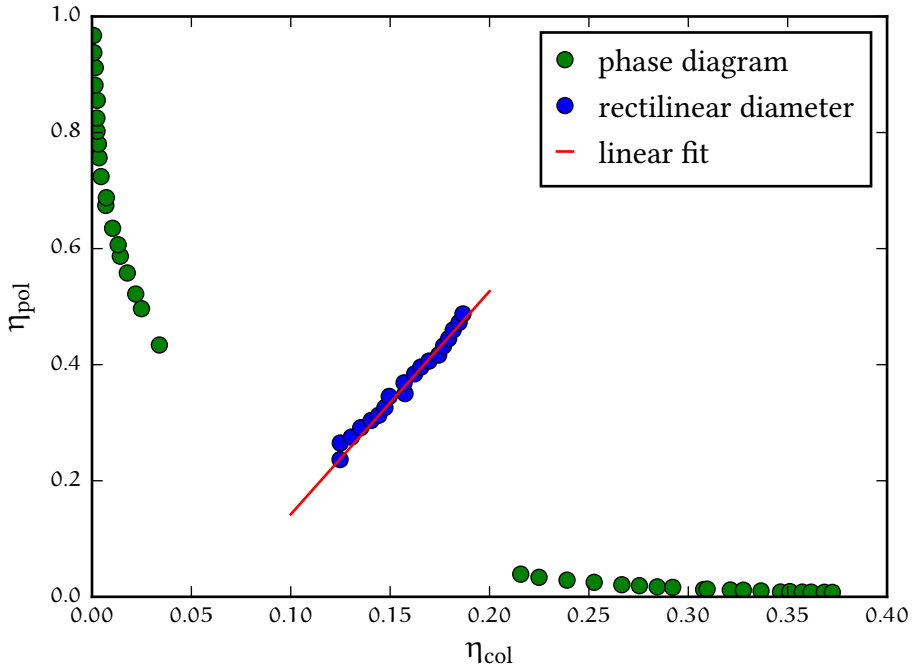

Figure 7.1: Fit of the rectilinear diameter as an estimation of the coexistence packing fractions.

We then analyse the system along the fitted line with the block distribution method from Chapter 6. The procedure changes slightly as to what has been discussed before for the Lennard-Jones system. Instead of the density ρ an a

priori unknown linear combination $\eta_d = \eta_{col} + \lambda\eta_{pol}$ of η_{col} and η_{pol} is the order parameter of the system

$$m = \eta_d^{liquid} - \eta_d^{gas} \quad . \tag{7.2}$$

By simulating along the rectilinear diameter we assume that we are at the correct coexistence packing fractions and thus a modification of η_{col} and η_{pol} must change η_d. For the rest of this section we will therefore use η_{col} as the driving variable for the phase transition, and implicitly adjust η_{pol} so that we remain on the line of rectilinear diameter.

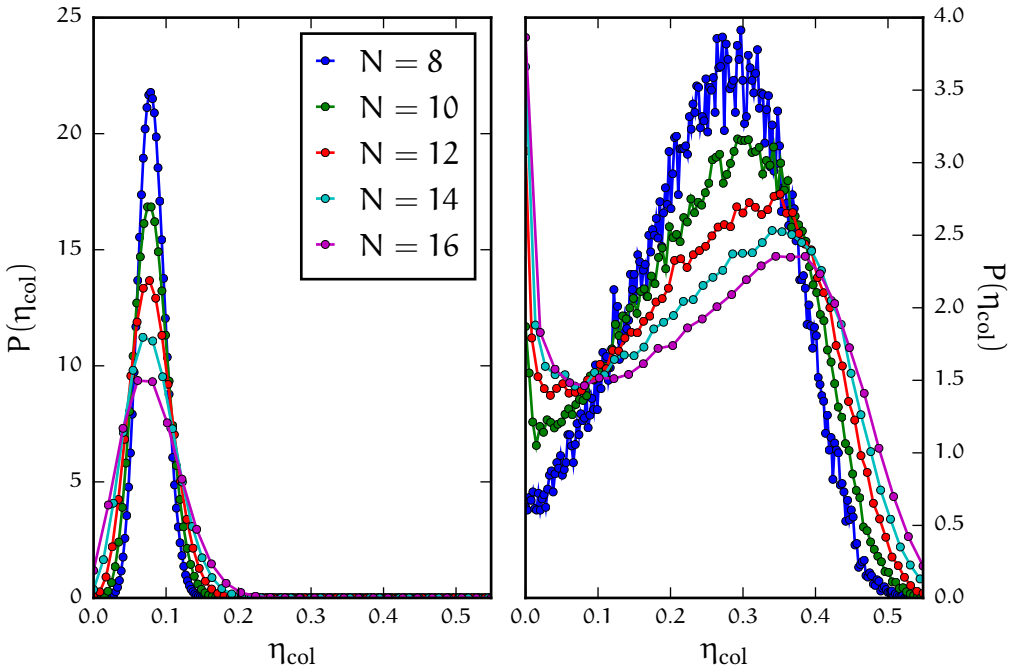

(a) $\eta_{col} = 0.08$ (b) $\eta_{col} = 0.25$

Figure 7.2: Density distribution for different subbox sizes (a) below and (b) above the critical packing fraction. The probability is normed so that the integral over the curve is one.

If we look at the density distribution of the colloids in the subboxes below and above the critical point (Figure 7.2), we get the expected behaviour from Section 2.3.5. Below the critical packing fraction the density distribution has a single Gaussian peak. Above the critical packing fraction the distribution becomes bimodal with a sharp peak at $\rho = 0$ and a second peak at higher density. The width of the peaks increases for smaller subbox sizes. The double peak structure above the critical colloid packing fraction is not as nicely developed as for the Lennard-Jones test in Figure 6.2. This could potentially lead to difficulties for the cumulant intersection, as the cumulant is expected to decrease in the two

phase region due to the increasing distance of the two peaks. For now, we proceed and calculate the cumulants for different values of η_{col} and η_{pol}. We analyse the system for various subbox sizes in Figure 7.3. The subbox sizes range from $L_{N=16} = 3.0$ to $L_{N=8} = 6.0$ and are thus from a slightly larger interval compared to the passive Lennard Jones system from before. For the state point closest to the cumulant intersection ($\eta_{col} = 0.10$ and $\eta_{pol} = 0.14$) are on average $5 - 39$ colloids and $13 - 108$ polymers in each subbox.

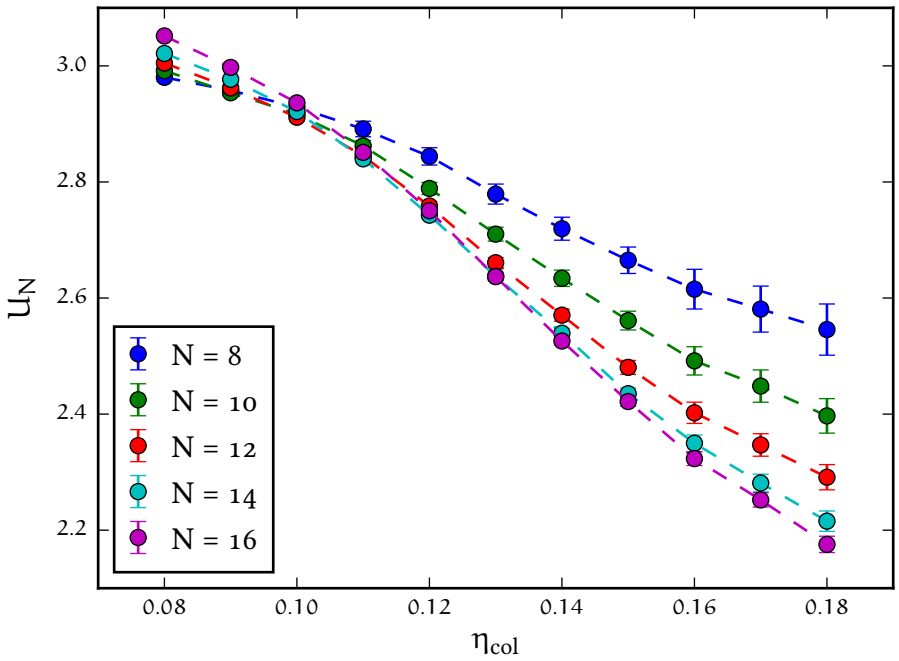

Figure 7.3: Intersection of the cumulants in a $S = 48\sigma$ cubic simulation box. Similar to the intersection of the cumulants in a passive Lennard Jones system not all subboxes cross in the same point. In total ten crossing points are present from which the critical colloid packing fraction can be determined as $\eta_{col}^{crit} = 0.103(4)$.

The value of the cumulant is already very close to the single phase limit of $U_N \to 3$. Therefore, the selection rule of the subboxes becomes difficult. Analogously to the Lennard-Jones case before, the subboxes should be clearly distinct, if we are far away from the critical point. For $\eta_{col} \gg \eta_{col}^{crit}$ this is the case and the biggest subbox also has the highest cumulant, as one would expect. $N = 16$ and $N = 14$ are only for high colloid packing fractions ($\eta_{col} \geqslant 0.16$) statistically distinguishable from each other, so that it is difficult to determine at which point these two cross. Therefore, an argument could be made to leave $N = 16$ out of the discussion. But for now we keep the smallest subbox, as it follows the predefined criteria for choosing the correct subbox sizes. For $\eta_{col} \ll \eta_{col}^{crit}$ we are already at so small densities that the cumulant is close to three. At $\eta_c = 0.08$

the values for the cumulant for the shown system sizes are in the correct order and the statistical errors indicate that all subboxes are fully separated.

To get an estimate for the statistical error of the cumulant U_N we first compute the mean of both moments separately. Then the standard deviations are divided by the square root of the number of uncorrelated snapshots. For that the autocorrelation, as discussed in Section 2.3.6, of the moments is analysed. In Figure 7.4 the autocorrelation of both moments for individual subboxes at $\eta_{col} = 0.10$ can be seen. After $t = 10^3$ the autocorrelation is close to zero. Due to the time step of $\Delta t = 0.002$ this corresponds to $5 \cdot 10^5$ MD steps, after which we use the block distribution method and average the calculated cumulants. The example shown is close to the critical packing fraction of the colloids in a region where the system is affected by critical slowing down. The correlation times for systems further away from the critical packing fraction are uncorrelated even faster and we use $t = 100$ as correlation time for them.

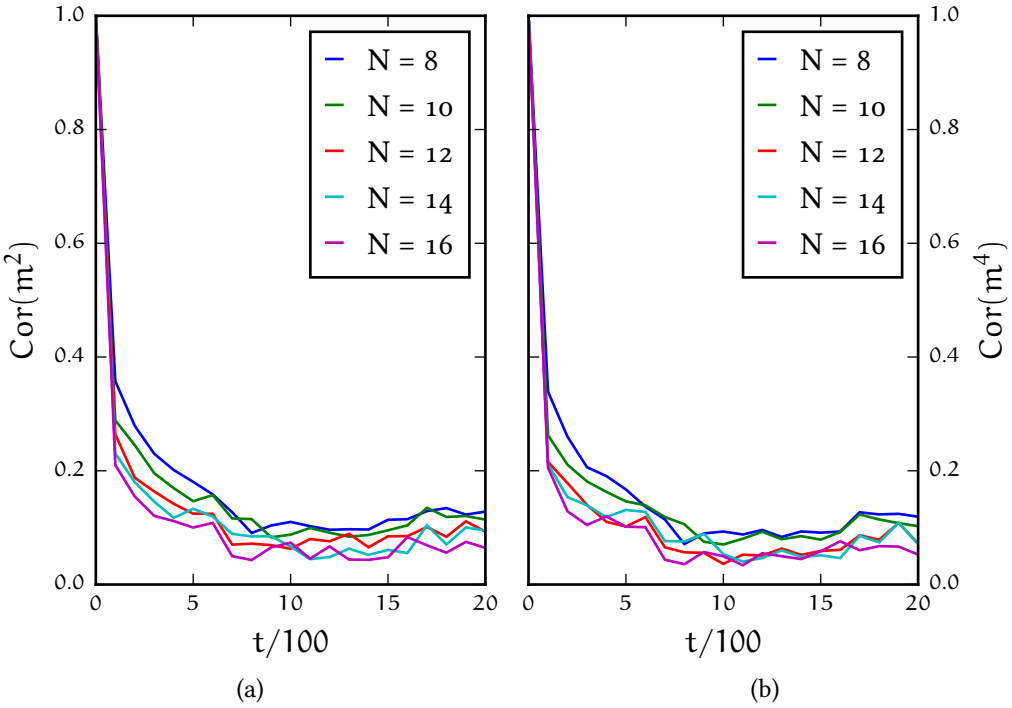

Figure 7.4: The autocorrelation of the moment (a) m^2 and (b) m^4 for various subbox sizes in a system with $S = 48\sigma$ and $\eta_{col} = 0.10$.

Similar to the test system before, the cumulants in Figure 7.3 do not cross in a single point. From the ten crossings we estimate the critical point to be at $\eta_{col}^{crit} = 0.103(4)$ at a cumulant $U_N = 2.88(3)$. The critical polymer packing fraction can then be extracted from the rectilinear diameter $\eta_{pol}^{crit} = 0.15(2)$. This

estimate for the critical point is shown in Figure 7.5 in relation to the phase diagram with the estimated error.

Note that we do not claim that this is the critical point of this active system. Instead this would be the critical point if the system followed the law of rectilinear diameter which, at this point, we do not know. In the calculation of the error of the critical point we neglected the possible error of the fitted rectilinear diameter. It is, however, a good indication that the active model gives a similar slope as the passive model, which follows the law of rectilinear diameter [96]. In Figure 7.5 the rectilinear diameter of the passive system as obtained with our simulation is shown. The critical point as determined in [43] falls nicely onto the linear fit. As a matter of fact, this result could motivate a mapping of the active system onto a passive one as attempted in Chapter 5, since the slope is hardly changing. This could indicate that a mapping on a different pair potential might result in a similar phase diagram, e. g. a more repulsive potential or even just a lower overall temperature.

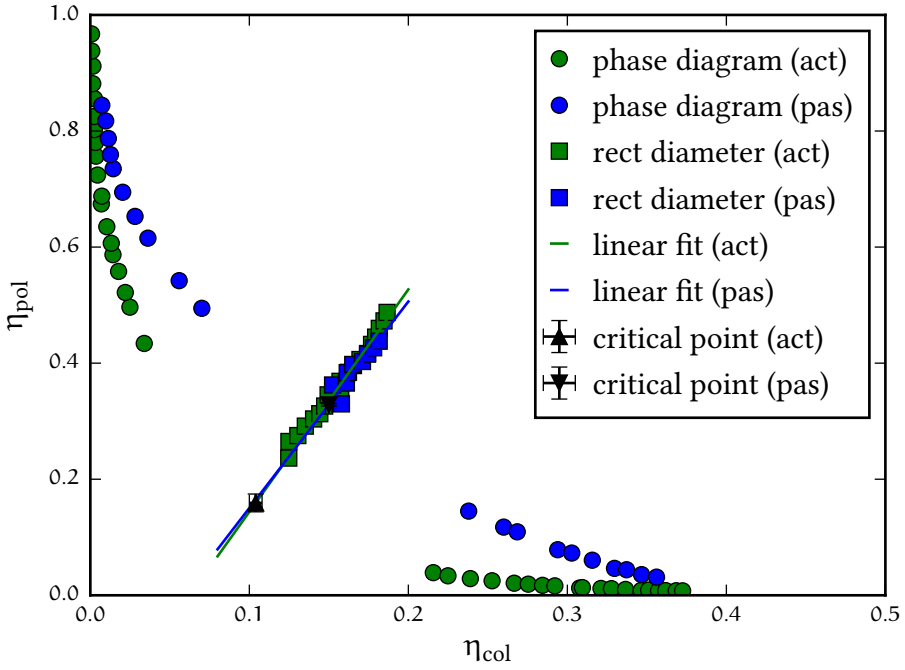

Figure 7.5: Comparison of the rectilinear diameter of the active and passive system. The data for the passive system (pas) is shown in blue, the critical point of the passive system is represented as a black downwards pointing triangle. The data for the active system (act) is shown in green, the critical point of the active system is represented as a black upwards pointing triangle. The slopes of the fitted data are comparable. The critical point of the passive system falls onto the linear fit.

7.2 CORRECTIONS TO THE CRITICAL POINT

From the simulations along the rectilinear diameter of the system we can extract further information. Not only can we calculate the cumulant for the colloids as done previously, but the cumulant of the polymers can be determined analogously. If the system followed the law of rectilinear diameter, both cumulants would intersect for the same simulated state point. However, even if this is not the case, we can extract valuable information from this crossing.

In [84] Rovere et al. have shown for a Lennard-Jones system that the cumulant crossing of the temperature is to some degree independent from the density of the system, thus T_c and ρ_c can, to a degree, be determined independently. In the active model this corresponds to η_{col}^{crit} and η_{pol}^{crit}. We can determine both from the same data as we can treat the simulation as a colloid gas-liquid phase transition and a polymer gas-liquid phase transition and the rectilinear diameter which we simulated can be projected onto either. The crossing of the cumulants for the colloid system is shown in Figure 7.3, the same data is analysed for the polymer system in Figure 7.6. The intersection corresponds to the critical packing fraction. Note that in Figure 7.6 all subboxes, except for the biggest subbox considered

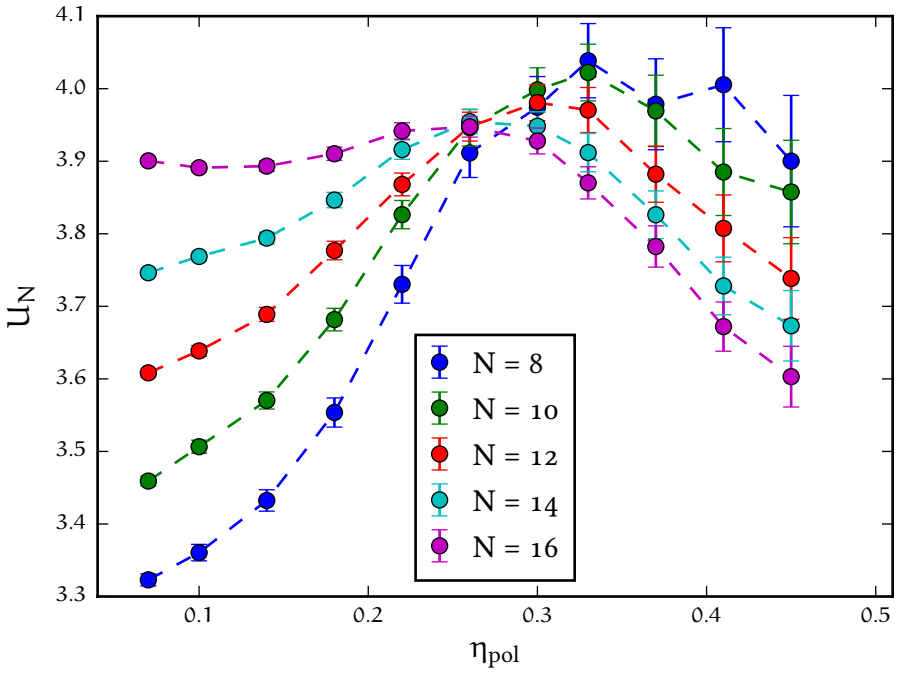

Figure 7.6: Estimation for the critical packing fraction of the polymers η_{pol}^{crit} from the cumulant intersections from the same data as used in Figure 7.3. From the ten crossings we estimate $\eta_{pol}^{crit} = 0.278(8)$.

($N = 8$), cross nearly in a single point. However, due to the slope of the estimated rectilinear diameter, the resolution of the polymer packing fraction is worse than for the colloid packing fractions from before. The cumulants do not separate fully after the crossing, as the estimated statistical error is big. This is due to the high density at which the crossing occurs and thus worse statistics compared to the points at low density. Also, the value of the cumulant is big and one observes large fluctuations in the moments.

In Figure 7.7 the critical packing fractions are shown on the estimated rectilinear diameter. From both an estimate for the actual critical point can be extracted. Note that we assume that we simulate reasonably close to the actual value and thus do not change the result. This is most likely true for η_{col}^{crit}, where the difference of both values corresponds to a difference in the density of $\Delta\rho = 0.06$ and $\Delta\rho/\rho \approx 23\%$ and is thus comparable to [84]. However, for η_{pol}^{crit}, the difference is huge ($\Delta\rho = 0.44$ and $\Delta\rho/\rho \approx 45\%$). Thus, we have to determine the critical packing fraction for the polymers in another way. At this point we conclude that the active system does not follow the law of rectilinear diameter as the passive system would.

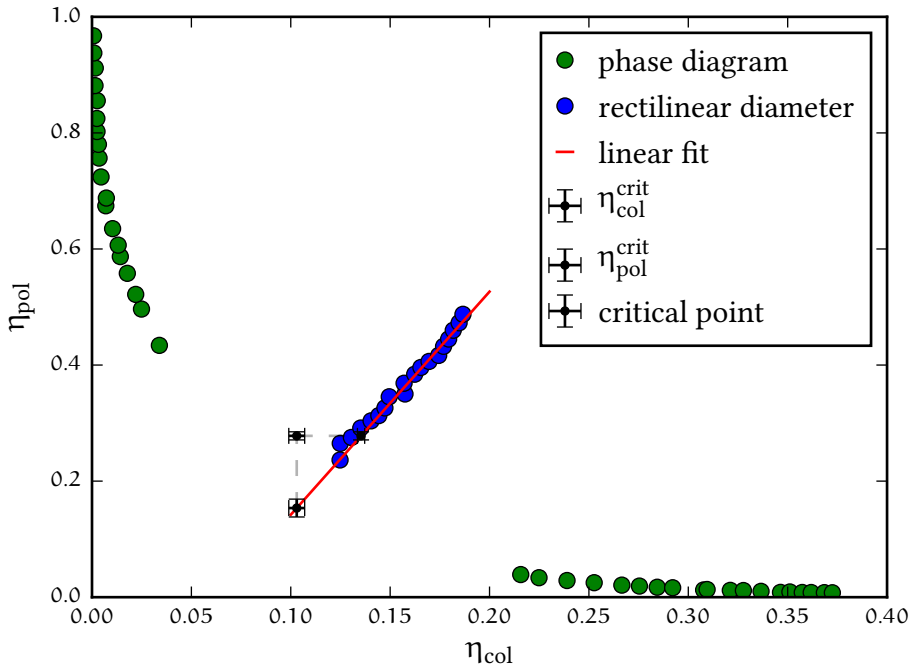

Figure 7.7: Determination of the critical point from the "independent" cumulant intersections of the colloids and polymers. For η_{col}^{crit} the x error is estimated from the cumulant intersection, while the y error is estimated from the uncertainty of the rectilinear diameter fit and vice versa for η_{pol}^{crit}. The estimated critical point inherits then both uncertainties of the respective cumulant intersections.

7.3 EXTRAPOLATING FROM THE HOMOGENEOUS PHASE

7.3.1 Maximal Q_L

In the previous section the critical packing fractions were determined from the same set of data. While the colloid packing fractions are reasonably close to each other, this is not true for the polymer packing fractions. Thus, an alternative way to determine the critical polymer packing fraction is needed.

We take a look at the phase diagram and determine the slopes of pairs of points representing coexistence states in the phase diagram. These slopes correspond to the constant temperature simulations we have performed for the Lennard-Jones system in Section 6.2. Therefore, we expect a simulation along such a slope to yield the coexistence packing fractions. Since in the case of the active model the slopes change due to the curvature of the phase diagram, we extrapolate the determined slopes to the estimated critical colloid packing fraction and find $m \approx -2$. We simulate various state points of the active system on

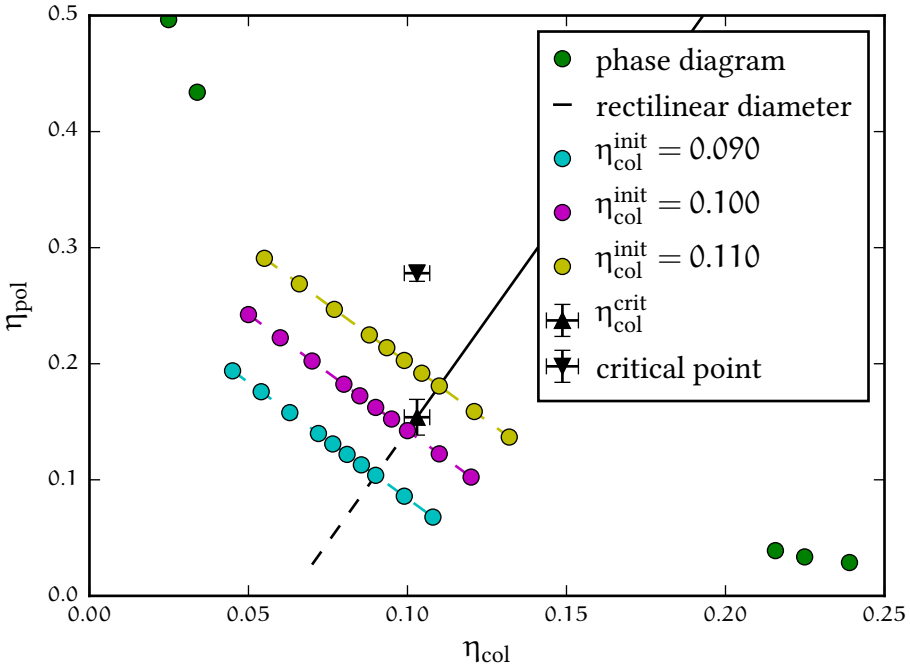

Figure 7.8: Magnified phase diagram of the active system around the critical point. The black line is the rectilinear diameter as determined before. The dashed black line is the elongation thereof into the one phase region. For several points on this line we simulate along a fixed slope of $m = -2.0$ to determine the order parameter. Exemplary, the simulated data points for $\eta_{col}^{init} = 0.090$ (cyan), $\eta_{col}^{init} = 0.100$ (magenta) and $\eta_{col}^{init} = 0.110$ (yellow) are shown.

lines in the one phase region in the vicinity of the critical point with the slope $m = -2$. Note, that it is an assumption that the slope in the vicinity of the critical point is not changing. However, the variation is probably small as the slopes cannot cross each other. The crossing of the slopes with the rectilinear diameter (or its extension below the critical point) are used as identification of the slope and referred to as η_{col}^{init}. Three such slopes with the simulated data points are shown in Figure 7.8 exemplary. For each data point shown we simulate a cubic system with $S = 48\sigma$. These simulations are "equilibrated" for one day. The production runs take ten days per point. The results are then analysed with the block distribution method. Since the system can now only move on those lines, the point closest to the ideal η_d will be favoured. Points that are far away should still follow the already discussed trend

$$Q_L(\eta_c) \to \frac{1}{3} \begin{cases} \eta_c \gg \eta_c^{crit} \\ \eta_c \ll \eta_c^{crit} \end{cases} . \tag{7.3}$$

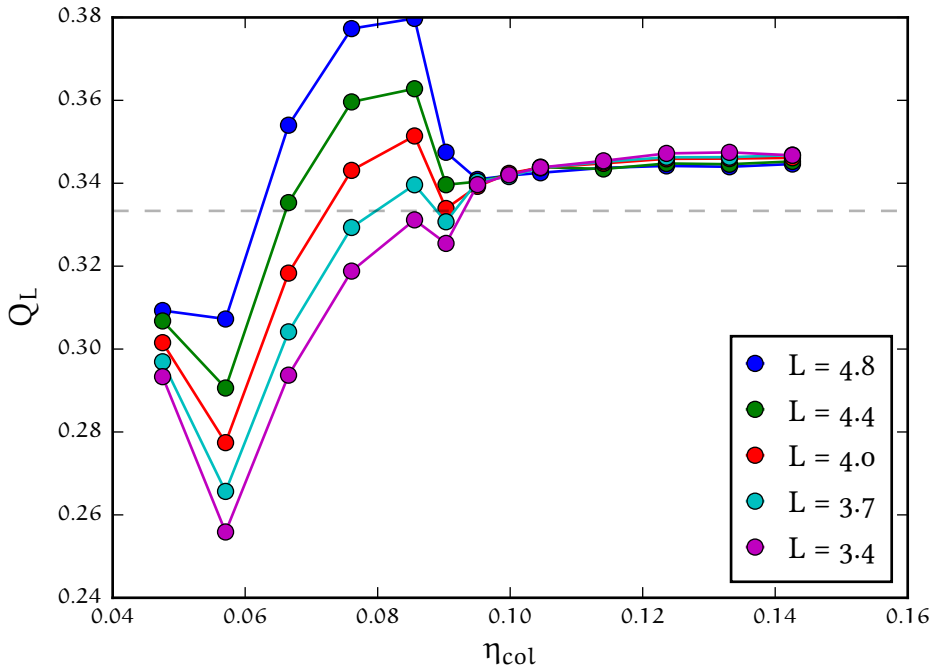

Figure 7.9: Q_L for various colloid packing fractions η_{col} on a slope with $m = -2$ in the phase diagram starting from an initial point on the elongated rectilinear diameter of (0.095/0.123). The maximum for subboxes with $N < 13$ is at $\eta_{col}^{max} = 0.090$, which corresponds to a polymer packing fraction of $\eta_{pol}^{max} = 0.133$. The maxima of smaller subboxes cannot be distinguished from the tail which is slightly above the expected value of $1/3$ shown as dashed grey line.

Analogously to Section 6.2 we can calculate Q_L and determine the coexistence packing fractions on each simulated slope. An example is shown in Figure 7.9 for an initial packing fraction of $\eta_{col}^{init} = 0.095$. Similar to Figure 6.5 the smallest subbox is below bigger subboxes for low densities and has a larger Q_L value for higher packing fractions. For simulations where the system is dilute the expected value of $Q_L = 1/3$ is not reached, while for big packing fractions the value of Q_L saturates at a value which is higher than expected. More importantly, a maximum is only reached for big subboxes when the critical point is approached. Close to the critical point we can calculate the points in the phase diagram for which Q_L reaches a maximum. Extrapolating these points to the critical colloid packing fraction, as determined by the intersection of the cumulants, results in a correction to the previously calculated critical point. Note, that this correction should be understood as indication in which direction, if at all, the critical point may have to be corrected. This is due to the fact that those simulations are very close to the critical point and thus potentially suffer from finite size effects.

In Figure 7.10 we have determined the phase points where Q_L is maximal for some values close to the critical point. For subbox sizes that still feature a maxi-

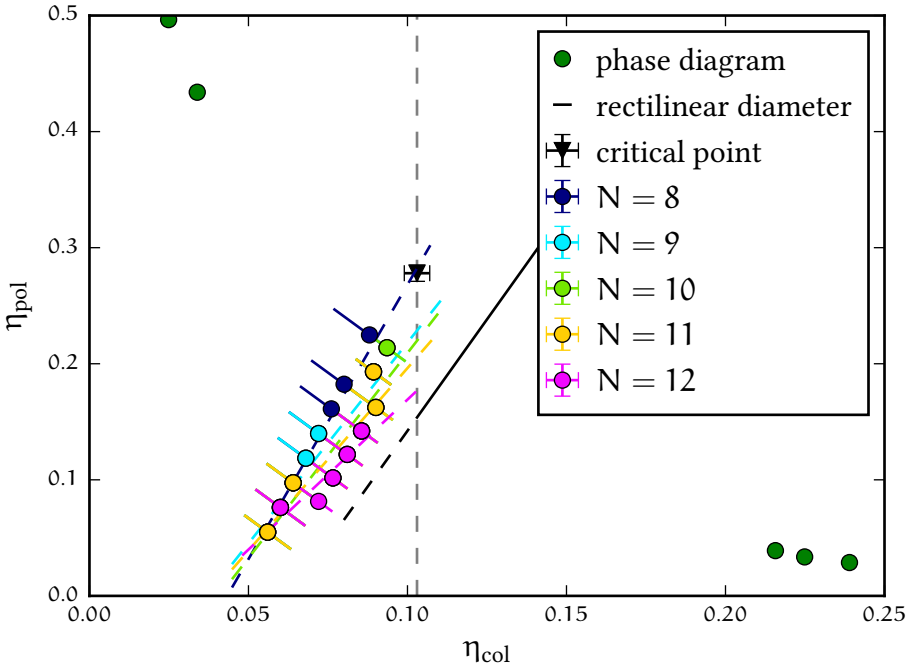

Figure 7.10: Extrapolation of the position of the maximal Q_L towards the critical colloid packing fraction (dashed grey line) for subboxes that are big enough to feature a maximum in Q_L. The dashed lines correspond to the linear fit to the data points of the same colour. From the extrapolation we estimate $\eta_{pol}^{crit} = 0.223(35)$.

mum we find a linear behaviour which differs from the rectilinear diameter as expected. These points can be extrapolated and the crossing of this slope with the previously determined critical colloid packing fraction can be computed. This results in an extrapolated critical polymer packing fraction (obtained from the average of the extrapolated lines crossing η_{col}^{crit}) of

$$\eta_{pol}^{crit;\,Q_L} = 0.223(35) \quad . \tag{7.4}$$

Note that the error bars given in Figure 7.10 are determined by the distance to the next simulated point on the same slope and are not respected in the extrapolation. Due to the big error bars the uncertainty of this extrapolation is large. However, we can still extract the general information that the critical point as determined in Section 7.1 is probably at a polymer packing fraction which is a bit lower than what we extracted from the cumulant crossing. Since the slope of the extrapolation decreases for smaller subboxes we cannot exclude finite size effects.

7.3.2 Locus of maximal susceptibility

Since the approach in the section before is prone to error due to the change in the slope and it only works for a subset of the determined subboxes, we look at an alternative way to determine the correct order parameter. For that we use the method of maximal susceptibility. Since the susceptibility in an infinite system diverges at the critical point, one can find a maximum in the susceptibility for each slope through the phase diagram that crosses the rectilinear diameter. Determining the maximum of susceptibility on a variety of such slopes results in a locus of maximal susceptibility that goes through the critical point [97–99].

In the cAO model multiple susceptibilities can be defined. In a grand canonical simulation one can extract all susceptibilities from the two dimensional probability distribution $P(N_{col}, N_{pol})$ [43]. Using the subbox distribution method this graph can be computed. In the one phase region one expects the distribution to be a bivariate Gaussian in the variables $N_{col} - \langle N_{col}\rangle$ and $N_{pol} - \langle N_{pol}\rangle$. From it we extract two different susceptibilities: the susceptibility of the colloids χ_{col} and the susceptibility of the order parameter χ_+:

- χ_{col} can be related to the two dimensional probability distribution $P(N_{col}, N_{pol})$ by determining the highest probability for a pair of particle numbers and then calculating the variance for constant N_{pol}.

  $$\chi_{col}\big|_{N_{pol}=const} = \frac{\sigma_{col}^2}{N_{tot}} = \frac{1}{N_{tot}}\left(\langle N_{col}^2\rangle - \langle N_{col}\rangle^2\right) \tag{7.5}$$

  N_{tot} is the average total number of particles in a subbox.

- χ_+ can be extracted from the half-width half-maximum (HWHM) along the main axis of the bivariate Gaussian. For that we fit the probability distribution with an ellipse where the probability to find the combination of colloids and polymers is at half the value of the maximum. The main axis of this ellipse is the HWHM of the order parameter. For the order parameter susceptibility χ_+ we use that the HWHM is proportional to the variance. In case of a Gaussian distribution, which we will not have close to the critical point, the proportionality constant would be $\text{HWHM} = \sqrt{2\ln(2)}\sigma$.

$$\chi_+ \propto \frac{(\text{HWHM})^2}{N_{\text{tot}}} \tag{7.6}$$

An example of the two dimensional probability distribution for three different state points on the same slope is shown in Figure 7.11. For each distribution an ellipse fit is performed to determine the main axis of the distribution. The most likely colloid-polymer pair $P_{\text{max}}(N_{\text{col}}, N_{\text{pol}})$ is increasing in the number of

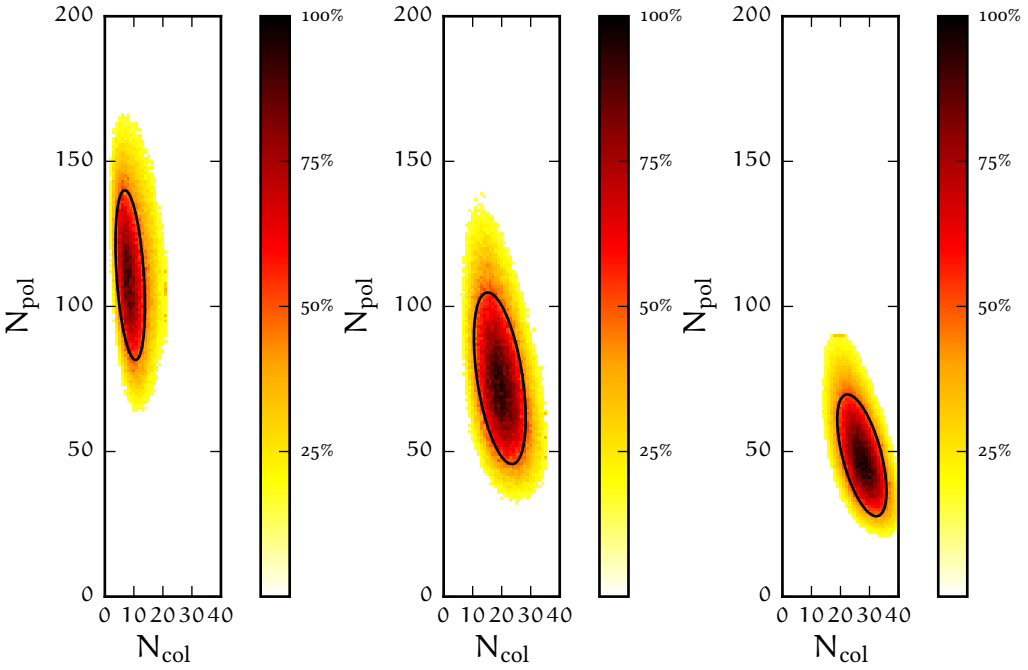

(a) $\eta_{\text{col}} = 0.055, \eta_{\text{pol}} = 0.291$ (b) $\eta_{\text{col}} = 0.099, \eta_{\text{pol}} = 0.203$ (c) $\eta_{\text{col}} = 0.132, \eta_{\text{pol}} = 0.137$

Figure 7.11: The two dimensional probability distribution $P(N_{\text{col}}, N_{\text{pol}})$, for different state points on the same slope ($\eta_{\text{col}}^{\text{init}} = 0.110$) and a subbox size of $L = 4.8$. The black line is determined by fitting $P(N_{\text{col}}, N_{\text{pol}}) = 0.5 \cdot P_{\text{max}}(N_{\text{col}}, N_{\text{pol}})$ with an ellipse. For the sake of visibility points with a probability lower than 15% of the maximum probability are not shown.

colloids and decreasing in the number of polymers when going from a low packing fraction of colloids to a higher (Figure 7.11 (a) to (c)), indicated by the black centre. Combined, this results in a decreasing average total number of particles in the subbox. But as the main axis of the ellipse, and thus the HWHM, is also shrinking continuously, the order parameter susceptibility has a maximum for intermediate packing fractions.

Figure 7.12. Since we get hysteresis effects in the vicinity of the critical point, and due to the finite size of our system, we will get a one phase region even if we are already in the two phase region. Therefore, the analysis could be done around the critical point in both phases. However, the simulations are getting slower close to the critical point due to critical slowing down and due to the increased density of the system.

For both susceptibilities we can determine the maximal susceptibility on each slope. Analogously to the previous section, these values, for which we know the colloid and polymer packing fraction, can be extrapolated to the critical colloid packing fraction.

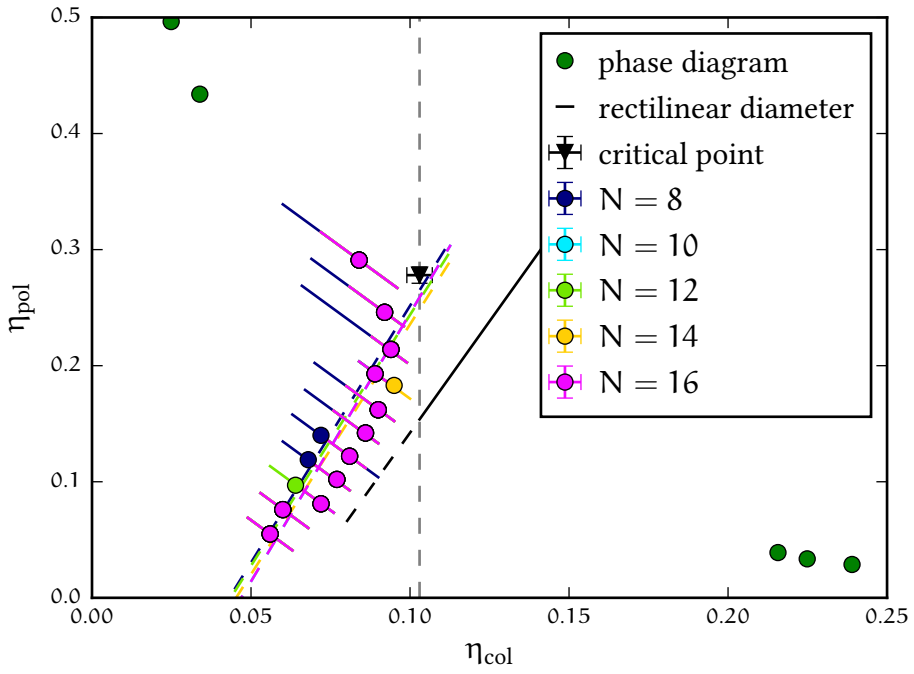

Figure 7.12: Extrapolation of the maximum $\chi_{col}(L)$ towards the critical colloid packing fraction (dashed grey line). The error bars are given by the distance to the next simulated point on the same slope but are not respected in the extrapolation. The dashed lines correspond to the linear fit to the data points of the same colour. The critical polymer packing fraction is determined as $\eta_{pol}^{crit;\,\chi_{col}} = 0.258(5)$.

For χ_{col} this has been done in Unlike for Q_L this works for every considered subbox size. Close to the critical point a divergence from the linear behaviour can be observed, which is most likely due to critical slowing down of the simulation. The extrapolation suggests that the critical polymer packing fraction is higher than determined by extrapolating Q_L but lower than the one determined by the cumulant crossing. It is important to note that we do not observe a dependence of the susceptibilities to the size of the subbox. Instead, the fitted slopes are similar to each other and in no particular order.

If we extrapolate the order parameter susceptibility instead, we are very close to the estimated critical point as can be seen in Figure 7.13. All crossings have the critical polymer packing fraction, determined from the cumulant intersection, in their respective error bar, but tend to lie slightly below. With this method a better estimate of the critical point can be achieved. However, it should be noted that since an additional fit is necessary to determine χ_+, the method has a higher uncertainty than simply calculating χ_{col}. The error of the fit could be reduced by fitting multiple ellipses to the probability distribution and using the

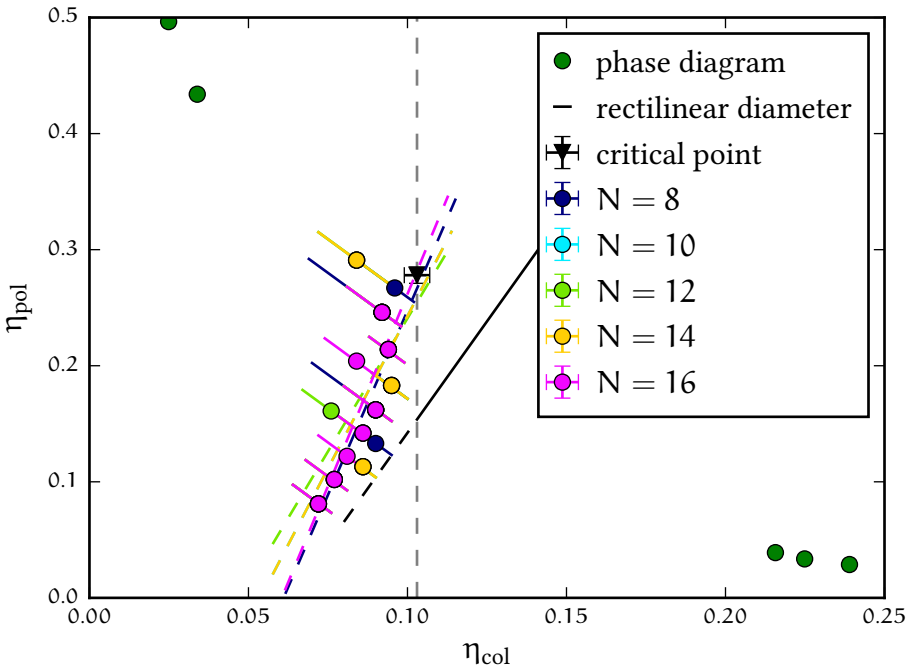

Figure 7.13: Extrapolation of the maximum $\chi_+(L)$, as defined in Equation 7.6, towards the critical colloid packing fraction (dashed grey line). The error bars are given by the distance to the next simulated point on the same slope but are not considered in the extrapolation. The dashed lines correspond to the linear fit to the data points of the same colour. The critical polymer packing fraction is determined as $\eta_{pol}^{crit;\,\chi_+} = 0.264(10)$.

mean HWHM. With this approach more points from the distribution would be considered and the statistical accuracy could be improved.

In the following we use

$$\begin{aligned} \eta_{\text{col}}^{\text{crit}} &= 0.103(4) \\ \eta_{\text{pol}}^{\text{crit}} &= 0.264(10) \end{aligned} \tag{7.7}$$

as our estimate for the critical point. As indicated before, $\eta_{\text{col}}^{\text{crit}}$ is obtained from the crossing of the cumulants, whereas $\eta_{\text{pol}}^{\text{crit}}$ is obtained from the arithmetic mean of the finite-size χ_+ estimates. Note that this estimate for $\eta_{\text{pol}}^{\text{crit}}$ is consistent with the result obtained from the cumulant crossing ($\eta_{\text{pol}}^{\text{crit}} = 0.278(8)$) and from the extrapolation of χ_{col} ($\eta_{\text{pol}}^{\text{crit}} = 0.258(5)$). The extrapolation of Q_L only worked for a subset of subboxes and showed a trend following the sizes of the subboxes.

7.4 CONSTANT CRITICAL COLLOID PACKING FRACTION

Another independent method to determine the critical polymer packing fraction is to simulate the system at a constant colloid packing fraction $\eta_{\text{col}}^{\text{crit}}$. Compared to Section 7.2 this has two advantages: The simulation includes the critical point, and is not just close to it, and the simulations are faster compared to the same polymer packing fractions from before because the colloid packing fractions are lower in the two phase region. From this simulations we can calculate the cumulant for the polymers $U_L(\eta_{\text{pol}})$ and compute their intersection point. This has been done in Figure 7.14. We find that $\eta_{\text{pol}}^{\text{crit}} = 0.268(8)$ which is slightly below the previously determined value ($\eta_{\text{pol}} = 0.278(8)$), although the error bars still overlap. Compared with the results from the extrapolations from the homogeneous phase, where we find that $\eta_{\text{pol}}^{\text{crit}} = 0.264(10)$ we get a nice agreement. A similar analysis could now be done for a constant critical polymer packing fraction, where an intersection at the critical colloid packing fraction is expected. This will be addressed in future studies.

So far, we have motivated the use of $\eta_{\text{col}}^{\text{crit}} = 0.103(4)$ as the correct colloid packing fraction because of the relatively small divergence of the two intersection points of the cumulant method from each other. Of course, we can now revisit the extrapolation from Section 7.2 and extrapolate the susceptibilities χ_{col} and χ_+ to the here determined critical polymer packing fraction $\eta_{\text{pol}}^{\text{crit}} = 0.268(8)$. With this we find that our initial assumption was correct, as we estimate $\eta_{\text{col}}^{\text{crit};\,\chi_{\text{col}}} = 0.105(2)$ and $\eta_{\text{col}}^{\text{crit};\,\chi_+} = 0.104(2)$. In this estimate we neglected the error in $\eta_{\text{pol}}^{\text{crit}}$, thus the given error for the extrapolated η_{col} is too low. But since we already have a good agreement with the cumulant

intersection a better estimate for the error is not needed. Note, that this determination is done with completely independent data compared to the crossing of the cumulants in Section 7.1.

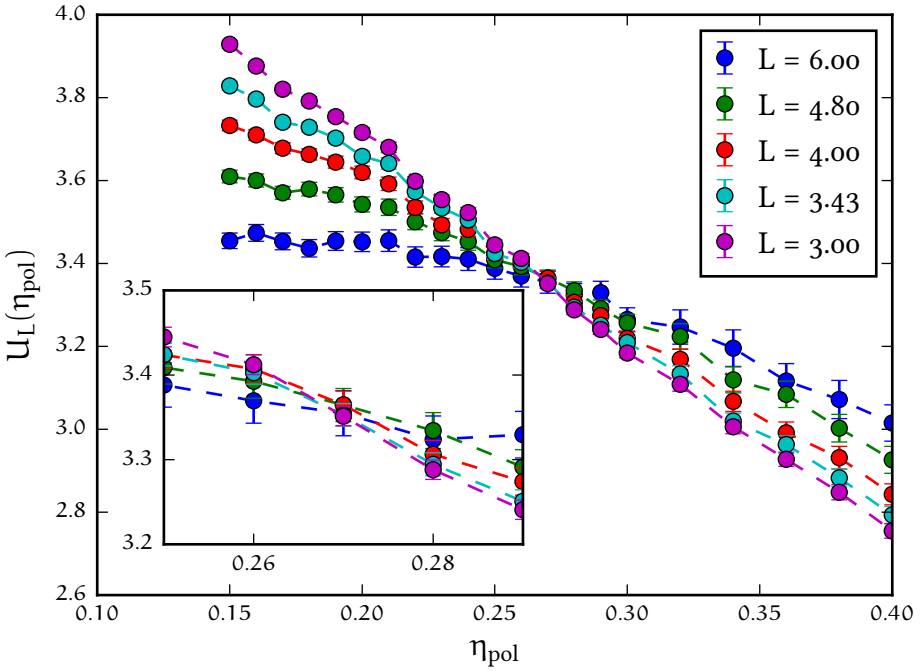

Figure 7.14: Cumulant intersection for a simulation at constant colloid packing fraction $\eta_{col} = 0.103$. The cumulant behaviour shows the expected steady change of the polymer cumulant compared to the behaviour in Figure 7.6. The inset show the intersection region magnified. The dashed lines are guide to the eye. From the intersection one extracts $\eta_{pol}^{crit} = 0.268(8)$.

7.5 COUPLING OF THE ACTIVITY AND THE ORDER PARAMETER

We have seen that the system deviates from the rectilinear diameter determined from the phase diagram. In this section a possible explanation for this behaviour is discussed. It is possible that the activity of the system couples to the order parameter. In the classical Vicsek model the order parameter is defined similarly to Equation 7.8 [28].

$$\varphi = \frac{\left| \sum_{i=1}^{N} \vec{v}_i \right|}{\sum_{i=1}^{N} |\vec{v}_i|} \tag{7.8}$$

This order parameter thus indicates if the velocities of the colloids in the system are fully aligned ($\varphi = 1$) or if the direction of motion is random ($\varphi = 0$).

In the two phase region of our model φ should change along the slope of the order parameter, as more colloids in the system account for a larger colloid-rich phase and thus more aligned velocities. In the one phase region, this dependence should not exist. For state points far from the critical point we have already shown in Section 4.2.3 that this is the case. However, getting close to the critical point means that the dependency has to change and approach the two phase behaviour. For all simulations along the slope of $m = -2$ we find that this is the case. φ is rising constantly with rising colloid numbers and approaches one for the most extreme cases simulated. Thus, there already exists a system wide velocity correlation of the colloids before a phase separation is observed.

η_c	φ	η_c	φ	η_c	φ
0.048	0.07	0.090	0.78	0.114	0.88
0.057	0.51	0.095	0.81	0.124	0.91
0.067	0.62	0.100	0.83	0.133	0.93
0.076	0.70	0.105	0.85	0.143	0.95
0.086	0.76				

Table 7.1: φ for various colloid packing fractions η_c on a slope with $m = -2$ in the phase diagram starting from an initial point on the elongated rectilinear diameter of (0.095/0.123).

In Table 7.1 φ is shown exemplary for the simulation with $\eta_{col}^{init} = 0.095$. Note the enormous jump between the first two measured values in the table where φ changes from 0.07 to 0.51. As can be seen for high colloid packing fractions φ goes to one, indicating that all velocities are aligned. Therefore, the activity might influence the order parameter in this model. Such a coupling cannot be reproduced by a mapping to a passive system, as this is a purely non-equilibrium effect.

7.6 GIANT NUMBER FLUCTUATION

It has been shown in experiments, simulations and theory [100–102] that in active systems the fluctuation of the particle number of the active constituents behaves differently than in a system in equilibrium. The fluctuation can be expressed as

$$\langle \Delta N \rangle = \sqrt{\langle N^2 \rangle - \langle N \rangle^2} \propto \langle N \rangle^{\alpha_p} \quad , \tag{7.9}$$

where α_p describes the fluctuation. In an equilibrium system one expects, far from the critical point, that the exponent in Equation 7.9 is $\alpha_p = \frac{1}{2}$, due to

the law of large numbers. However, in close vicinity to the critical point, this exponent will increase because of percolating structures.

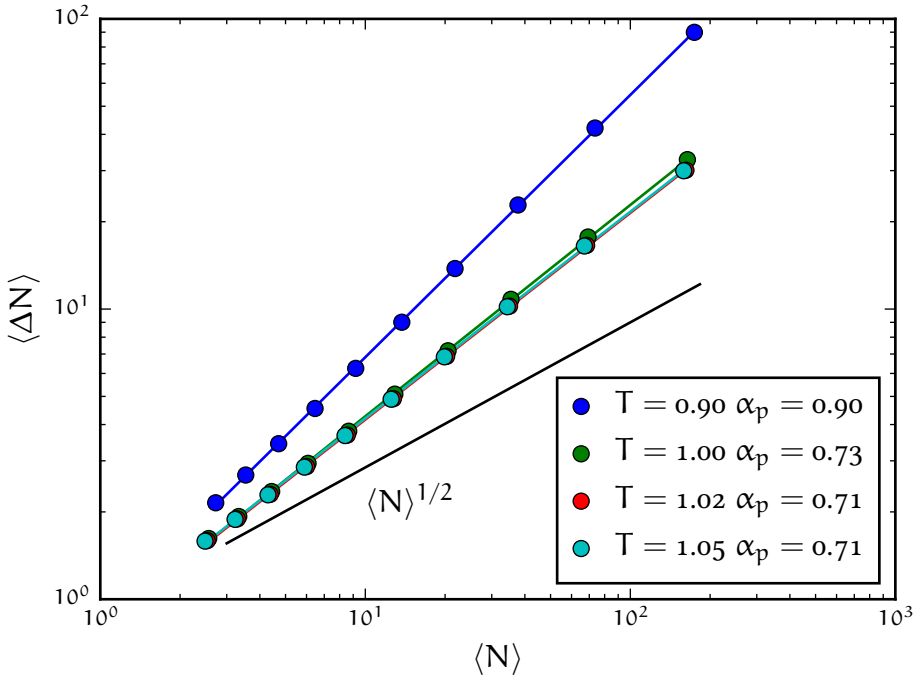

Figure 7.15: Giant number fluctuation in the passive Lennard-Jones system with $S = 24$ close to the critical point. All possible subboxes between $L = 2.0$ and $L = 8.0$ are analysed. The lines correspond to the fitted exponents and agree nicely with all subbox sizes. The exponent α_p is decreasing for higher temperature as expected, but is clearly above $\alpha_p = 0.5$ (black line) for a temperature that already shows a single peak in the density distribution Figure 6.2(b).

In our case this fluctuation can be computed with the block distribution method. An example is shown in Figure 7.15 for the passive Lennard-Jones test system studied earlier. For that we analyse the long trajectories from Section 6.1 and compute

$$\langle N \rangle = \rho_{col} \cdot L^3 \tag{7.10}$$

$$\langle \Delta N \rangle = \sqrt{\frac{1}{N_{sub}} \sum_i^{N_{sub}} (N_{col;i} - \langle N \rangle)^2} \quad , \tag{7.11}$$

where $N_{sub} = S^3/L^3$ is the total number of subboxes the system is divided into and $N_{col;i}$ is the number of colloids in the ith subbox.
For all temperatures shown in Figure 7.15 the exponent $\alpha_p > 0.5$, even though the density distribution in Figure 6.2(b) looks already Gaussian. This means that in our case the distinction between giant number fluctuations due to the activity

and due to the vicinity to the critical point cannot be made. However, we report that even for systems far away from the critical point we see an exponent $\alpha_p > 0.5$. As an example we show the results for different state points in Figure 7.16.

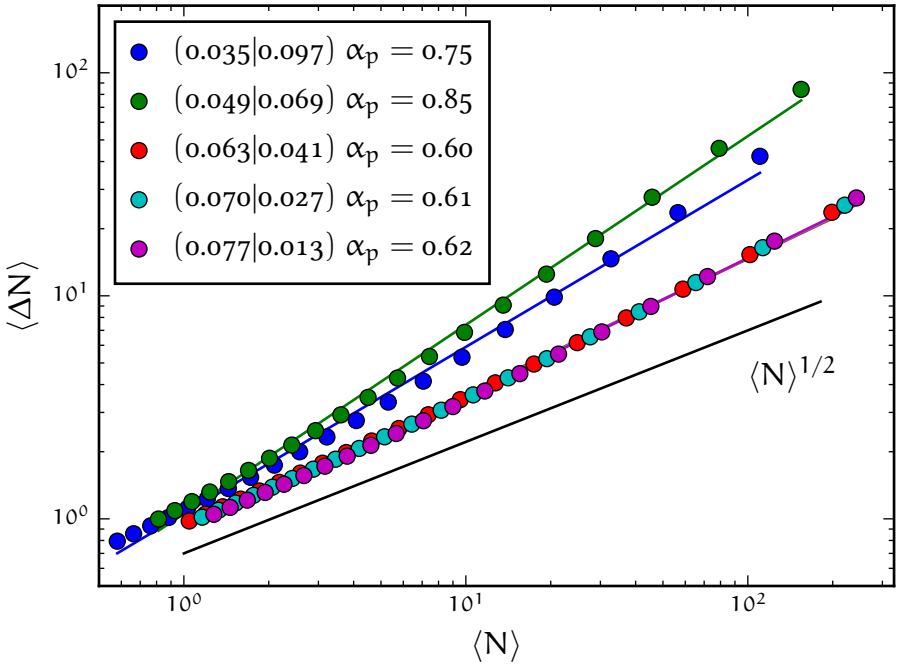

Figure 7.16: Giant number fluctuation in the active Vicsek model for different colloid and polymer packing fractions. The simulated state points are mentioned in the legend, denoted as point pairs $(\eta_{col}|\eta_{pol})$. The cubic NVT system has a length $S = 48$. The data points correspond to all possible subbox sizes between $L = 2.1$ and $L = 16.0$. The black line corresponds to an exponent $\alpha_p = 0.5$. The coloured lines are the fitted exponents of the data point of the same colour and it has to be appreciated that the scaling works for all subboxes considered.

We plan to further study this phenomenon in the future. For that we will look at different fluctuations, in order to separate the effects introduced by activity and those introduced by the critical point. A prime candidate is the velocity. As we have seen already in Figure 4.10(a) the velocity distribution has a much higher amplitude compared to a passive system. This indicates that one can use the velocity components to analyse the fluctuations induced by an active system. For that we could separate the velocity into components parallel and perpendicular to the mean velocity.

$$\langle \Delta v_{\parallel} \rangle = \sqrt{\langle \Delta v_{\parallel}^2 \rangle - \langle \Delta v_{\parallel} \rangle^2} \propto < N >^{\alpha_1} \tag{7.12}$$

$$\langle \Delta v_{\perp} \rangle = \sqrt{\langle \Delta v_{\perp}^2 \rangle - \langle \Delta v_{\perp} \rangle^2} \propto < N >^{\alpha_2} \tag{7.13}$$

One would expect that $\alpha_1 \neq \alpha_2$ for the active system, while the passive system would always fulfil $\alpha_1 = \alpha_2$ as there is no preferred direction of motion. Similar order parameters have been discussed by Toner et al. [103–105].

8 UNIVERSALITY?

The Ising universality class is probably one of the best studied universality classes and it has been shown that a lot of different systems share it. One of those systems is the continuous Asakura-Oosawa (cAO) model [43] which we used as a basis for our active model.

The classical Vicsek model on the other hand is, due to its minimal character, a candidate for a universality class for active particles itself [92, 106]. The critical exponents for the 2D classical Vicsek model [106, 107] differ from the 2D Ising exponents [38].

Since the phase transition of our active model is also present in the passive case we assume that for small active forces f_A we recover the 3D Ising universality class. However, for larger values of f_A a divergence from those exponents is possible. In the following we will try to determine two critical exponents for our active system with $f_A = 10$. It should be noted that those exponents are extremely dependent on the value of the critical point, and thus should only be regarded as first estimation until the critical point is known with higher accuracy. For now we use $\eta_{col}^{crit} = 0.103(4)$ and $\eta_{col}^{crit} = 0.268(8)$ as the critical point of the active system as determined in Chapter 7.

8.1 DETERMINATION OF THE CRITICAL EXPONENT β

With the critical point and the phase diagram we can now calculate the critical exponent β. In Equation 2.23 the critical exponent was introduced as

$$M = M_0 \varepsilon^{\beta} \quad . \tag{2.23}$$

In this model M is the distance between a pair of points $\left(\eta_{col}^{gas} \middle| \eta_{pol}^{gas}\right)$ and $\left(\eta_{col}^{liquid} \middle| \eta_{pol}^{liquid}\right)$ in the phase diagram, and thus

$$M = \sqrt{\left(\eta_{col}^{liquid} - \eta_{col}^{gas}\right)^2 + \left(\eta_{pol}^{liquid} - \eta_{pol}^{gas}\right)^2} \quad , \tag{8.1}$$

while ε will be the shortest distance to the critical point

$$\varepsilon = \frac{\sqrt{\left(\frac{1}{2}\left(\eta_{col}^{liquid} + \eta_{col}^{gas}\right) - \eta_{col}^{crit}\right)^2 + \left(\frac{1}{2}\left(\eta_{pol}^{liquid} + \eta_{pol}^{gas}\right) - \eta_{pol}^{crit}\right)^2}}{\sqrt{\left(\eta_{col}^{crit}\right)^2 + \left(\eta_{pol}^{crit}\right)^2}} \quad . \tag{8.2}$$

In Figure 8.1 M, calculated from the phase diagrams in Figure 4.2, is plotted against ε which was determined with the respective critical points (for the passive case we use the literature value from [43]) in a log-log plot. For the passive case we recover the 3D Ising value $\beta = 0.32(1)$ [108], which is to be expected as the passive model belongs to the Ising universality class [96]. The active case has a value of $\beta = 0.30(3)$ and is thus close to the value of the 3D Ising universality class as well. Even though the fit in Figure 8.1 matches the data points nicely, we have to assign a big uncertainty to the critical exponent for the active system. This is due to the error bars of the critical point, which in turn affects the determination of ε. In order to account for that, we have calculated ε for various critical points (within the error bars) and repeated the fit. We then choose the error for β in a way that it contains all possible slopes. To get a better estimation of the critical exponent β we have to determine the critical point with higher precision first. For bigger ε we get a divergence from the linear behaviour, and we thus do not account for them in the fit. But we expect the system to follow this power law only for small ε anyway.

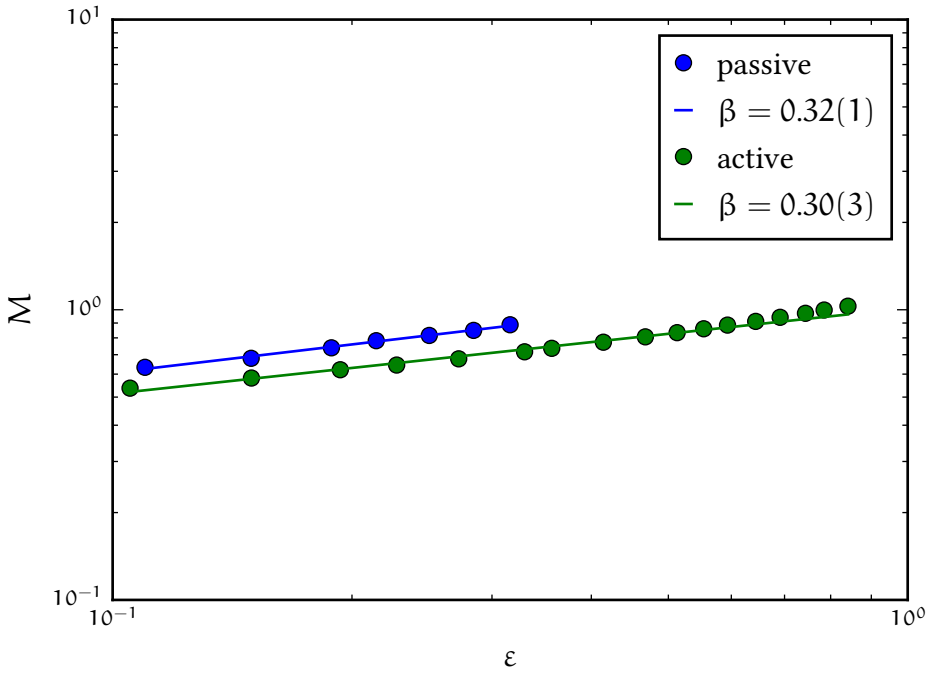

Figure 8.1: Comparison of the critical exponent β of the active and the passive model. The points are the respective values as extracted from the phase diagrams in Figure 4.2, while the line represents a fit from which the critical exponent β is determined.

8.2 DETERMINATION OF THE CRITICAL EXPONENT ν

To determine the critical exponent ν we use the cumulant intersection of the colloids. The slope of the cumulants at the critical point can be extracted from Figure 7.3. It is expected that $\frac{dU_L}{d\eta_{col}}$ scales with L as [109]

$$\frac{dU_L}{d\eta_{col}} \propto L^{\frac{1}{\nu}} \quad . \tag{8.3}$$

The slope around the critical point does not change rapidly. Therefore, we assume that the error we make by determining the slope numerically is small. However, the slope in Figure 7.3 is negative. Therefore, we rewrite Equation 8.3 by using the definition of Q_L (Equation 6.6) to

$$\begin{aligned} \frac{dQ_L}{d\eta_{col}} &\propto L^{-\frac{1}{\nu}} \\ \nu \cdot \ln\left(\frac{dQ_L}{d\eta_{col}}\right) &\propto \ln\left(\frac{1}{L}\right) \quad . \end{aligned} \tag{8.4}$$

The critical exponent ν can now be determined by a fit. This is done in Figure 8.2.

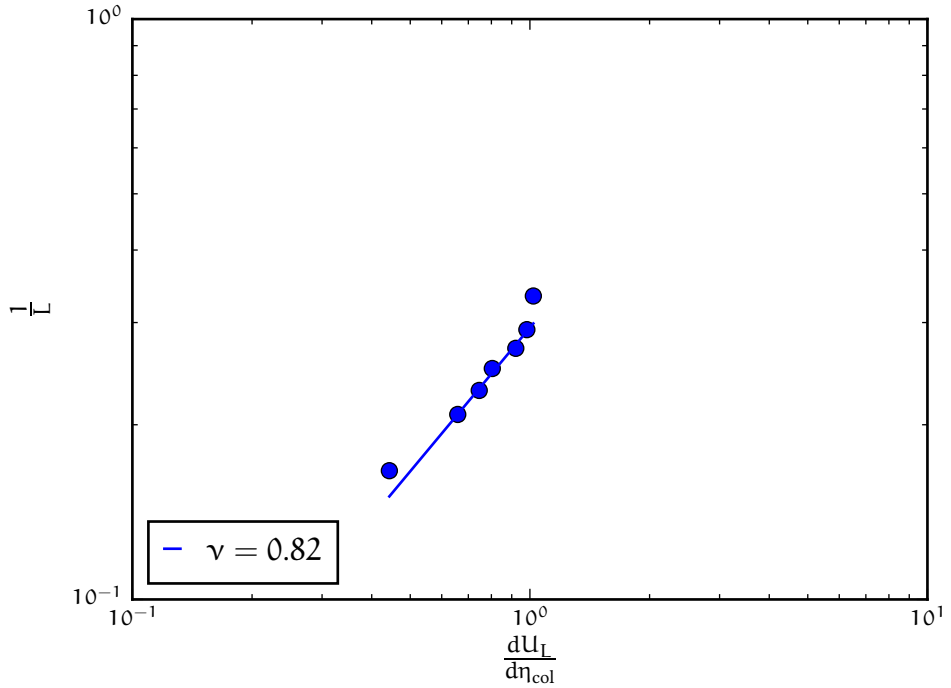

Figure 8.2: Fit of the critical exponent ν of the active model. The points are the respective values for the subboxes $N = 8, 10, 11, 12, 13, 14, 16$, while the line represents a fit from which the critical exponent ν is determined. The subboxes $N = 8$ and $N = 16$ are not accounted for in the fit as they clearly differ from the power law.

We find $\nu = 0.82$, which differs from the 3D Ising value of $\nu_{\text{Ising}} = 0.63$ [39]. However, we have to leave out the subboxes $N = 8$ and $N = 16$ as they do not follow the linear behaviour in the log-log plot. Instead only the intermediate subbox sizes $N = 10$ to $N = 14$ are fitted.

The critical exponent ν can be used to rescale the cumulants for different system sizes and project them onto a single master curve around the critical point. This is done by changing the x-axis in Figure 7.3 from η_{col} to $(\eta_{\text{col}} - \eta_{\text{col}}^{\text{crit}}) \cdot L^{\frac{1}{\nu}}$. Such

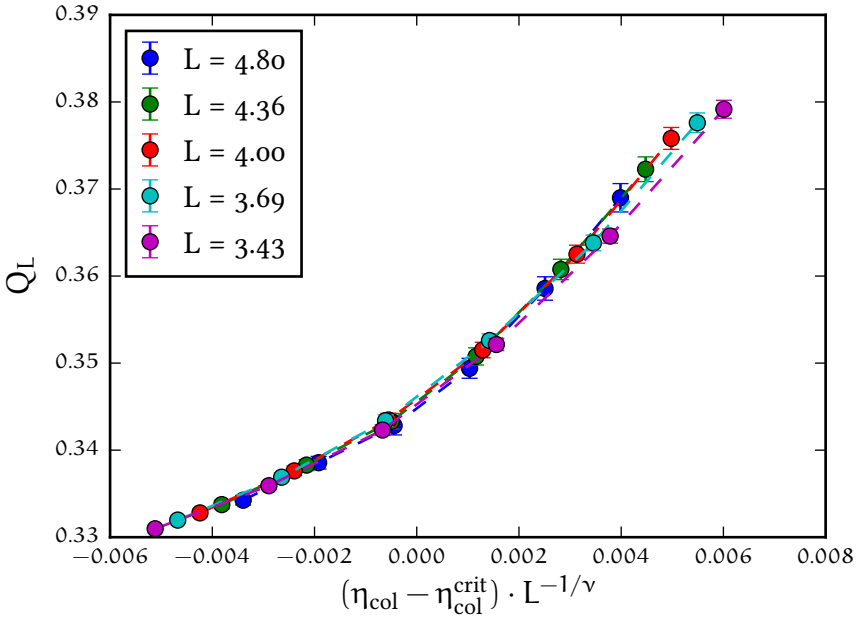

Figure 8.3: Collapse of the cumulant intersection from Figure 7.3 onto a master curve using the critical exponent $\nu = 0.82$ as determined in Figure 8.2.

a collapse has been done in Figure 8.3. While the cumulants fall nicely onto one curve it should be stated that the same collapse for the Ising value of ν does not appear to be significantly worse. This collapse is shown in Figure 8.4. Therefore, we cannot conclude that the active system does not belong to the Ising universality. To answer this question more simulations around the critical point have to be performed and the statistical error has to be reduced further.

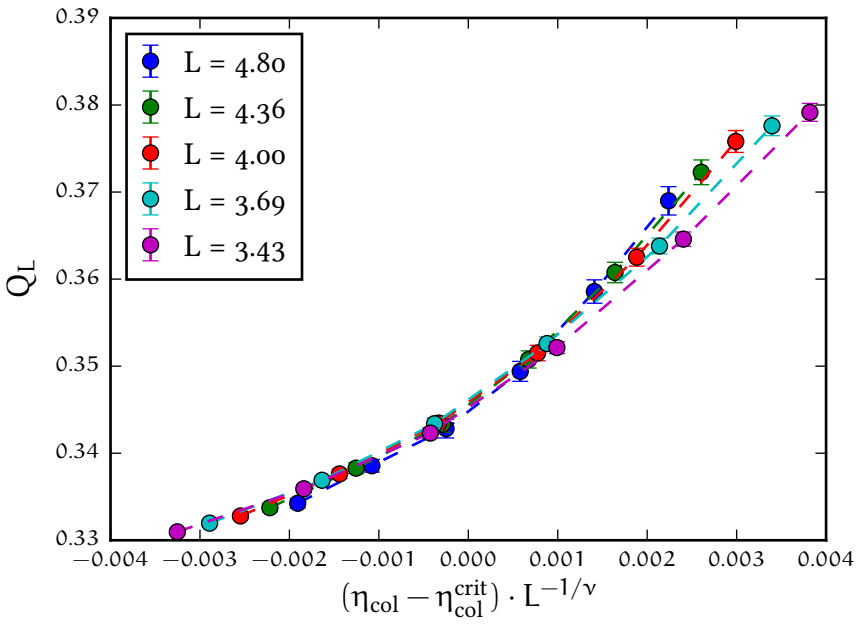

Figure 8.4: Collapse of the cumulant intersection from Figure 7.3 onto a master curve using the critical exponent $\nu_{Ising} = 0.63$.

9 CONCLUSION AND OUTLOOK

We have introduced a model of activity to study the non-equilibrium effects on the phase behaviour with computer simulations. For that a passive model that already features a phase separation is used as a basis. The active model is then imposed onto the passive and care has been taken to ensure that the passive model is obtained as one limit of the active model. By doing so, it is guaranteed that we understand the phase separation in the limit of infinitesimal small activity.

The active model proposed in this thesis features an enhanced phase separation compared to the original equilibrium model. This is due to the alignment force of the Vicsek model, which induces a velocity correlation in the active specimen and thus leads to the formation of clusters. This correlation leads to large amplitudes in the mean velocity for a system in the homogeneous phase, whereas the active particles in the phase separated system align their velocities perpendicular to the interface and thus reduce the interaction with the passive polymers.

We have shown in Chapter 4 that the active force f_A can be used to control the enhancement of phase separation and that the original phase diagram can be obtained in the limit of $f_A = 0$.

In Section 4.4 it has been shown that the active model has to be defined with a specific thermostat to handle the constant energy input into the system. In the current form, one can therefore not study the effect of hydrodynamic interactions, at least not in the proposed way by using a Maxwell-Boltzmann thermostat. A possible solution has been presented in Section 4.1.5 by changing the active model from self-propelled particles to non-propelled but keeping the alignment rule. The system would still be out of equilibrium, but we have found indications that the enhancement in phase separation might not be preserved. Future studies are planned, in which we will look at a temperature dependent phase transition, like for example in the Lennard-Jones model, and use only the orthogonal component of the active force. To keep the temperature constant one might need to rescale the active velocity afterwards as mentioned in the general remark.

We have seen that the active system features an interesting temperature profile, if one respects the local mean velocity. The clustered active particles carry only

slightly more heat than the surrounding polymer bath. However, at the interface where active and passive particles interact, heat is generated. This friction, induced by the fast moving active particles close to the slow passive ones, can explain the enhanced phase separation as it is entropically favourable to separate the two different speeds. Additionally, this friction could lead to a higher "interfacial tension", since it would reduce the area where active and passive particles interact. This could also explain why we did not observe any finite-size structures for high active forces except for the slab configuration. The question of interfacial tension will be researched separately in the future.

Together with collaborators we have seen that a mapping of the active model to the passive one works to some extent. With integral equation theory (IET) we have been able to correctly reproduce the colloid-rich branch of the phase diagram. The mapping and the simulated polymer-rich branch do not agree, which is most likely due to the structural difference of the polymer-polymer interaction, which has not been mapped. The dynamic properties can, of course, not be included in such a mapping. This is why one would only expect a partial agreement between the mapped and the real system in the first place.

We have given a description how the critical point of a system can be determined in a canonical (NVT) simulation by analysing fluctuations in subboxes of varying sizes. This recipe is tested on an equilibrium system and the critical point has been determined with good agreement compared to grand canonical (μVT) simulations. It should once again be emphasised that this method is general, and thus is expected to work for any active (or passive) system that features a second order phase transition. With this method we have determined the critical point of our active system. For that we have simulated a large system with a constant particle number, volume and temperature and have divided it in many smaller systems of the same volume. In these small systems the particle number can fluctuate and a quasi grand canonical system is sampled. These simulations have been analysed using multiple well-known methods from equilibrium physics which have been discussed and tested on a test system first. We have argued that the colloid packing fraction we have determined from the cumulant intersection of state points close to the critical point is the correct critical colloid packing fraction. The critical polymer packing fraction has been improved iteratively. With the independent data and the correct critical polymer packing fraction we could subsequently show that the critical colloid packing fraction has been determined correctly. Thus we have gotten consistent results for the critical point of the active system and have found that there is a deviation from the passive model, as the law of rectilinear diameter is not followed in the vicinity of the critical point. Instead we assume that a coupling between the order

parameter of the passive system and the activity occurs, which in turn shifts the critical point. We have proposed the order parameter of the original Vicsek model as one way to explain this coupling. In future studies we will test other order parameters as well, a prime candidate is the velocity fluctuation in direction of the mean velocity compared to the fluctuation perpendicular to it. This order parameter is unique to the active system, whereas we have seen that the particle number fluctuation can also be induced by the critical point.

Finally, we have determined two critical exponents β and ν. The active and passive system might share the same value for β. This is an indication that the active system is still in the same universality class as the passive one, which is 3D Ising. However, ν deviates from the 3D Ising value. At this point we cannot definitely state whether or not the active system belongs to the 3D Ising universality class. For that we will have to investigate all critical exponents in the future and determine the critical point with higher accuracy still. This will be a challenge, as a lot more simulations will be necessary, e. g. to determine the critical exponent of the susceptibility γ one would have to very accurately determine the maximum in the susceptibility. The data we have measured in Section 7.3.2 is not detailed enough to determine γ reliably. This is due to the sharp peak in the susceptibility, which induces a big error in the actual value of χ. However, the position of the maximum can be determined with good accuracy.

We have seen that the critical point in active systems can be determined and formulated a generic approach that can be used for other models as well. Currently, Jonathan Siebert is working with the same methods in order to determine the critical point for an ABP model and the preliminary results look promising.

Knowing the critical point of a system provides interesting insight. First it shows that one indeed has a second order phase transition. It also allows us to classify the active system, as we can now compute the critical exponents and thus test to which, if any, universality class the system belongs. Of course, there is still more work to be done, but other non-equilibrium systems have shown that there are universality classes specific to their activity [110]. It would be of great interest if such an universality class could also be found for self-propelled particles. Also, this could lead to better models to study active systems further as one could then construct a simple model for self-propelled particles that has the same universality class, similar to the Ising model for equilibrium soft matter.

APPENDIX

A.1 TEMPERATURE DISTRIBUTION

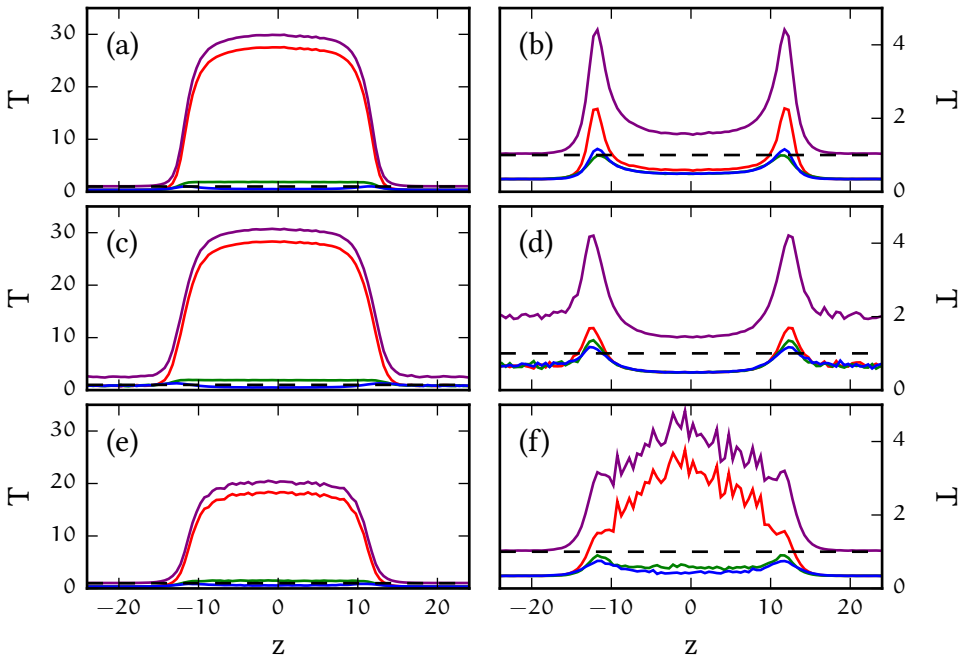

Figure A.1: Temperature distribution for a steady state with $\eta_{col} = 0.15$ and $\eta_{pol} = 0.30$ in a system with $L_x = L_y = 12\sigma$ and $L_z = 48\sigma$. The initial temperature $T_{init} = 1$ is shown by the dashed black line in all plots. The red line shows the results for the x axis, green the y axis, blue the z axis. The purple line is the total temperature distribution. (a) and (b) show the same results as in Figures 4.15 and 4.16. (c) is the global, (d) the local temperature distribution for the colloids only, while in (e) the global and (f) the local temperature distribution for the polymers are shown. The colloids carry most of the heat in the system, and do not cool down to the initial temperature independent of the analysis method we use. Interestingly (d) indicates that the colloids are cooler if clustered together than in the gas phase. The polymers have the initial temperature in their dense phase, but are dragged along in the colloid rich phase. To improve the polymer statistics in (f) we would have to analyse much larger trajectories as the number of polymers in the colloid rich phase is only small.

A.2 EFFECTIVE POTENTIAL

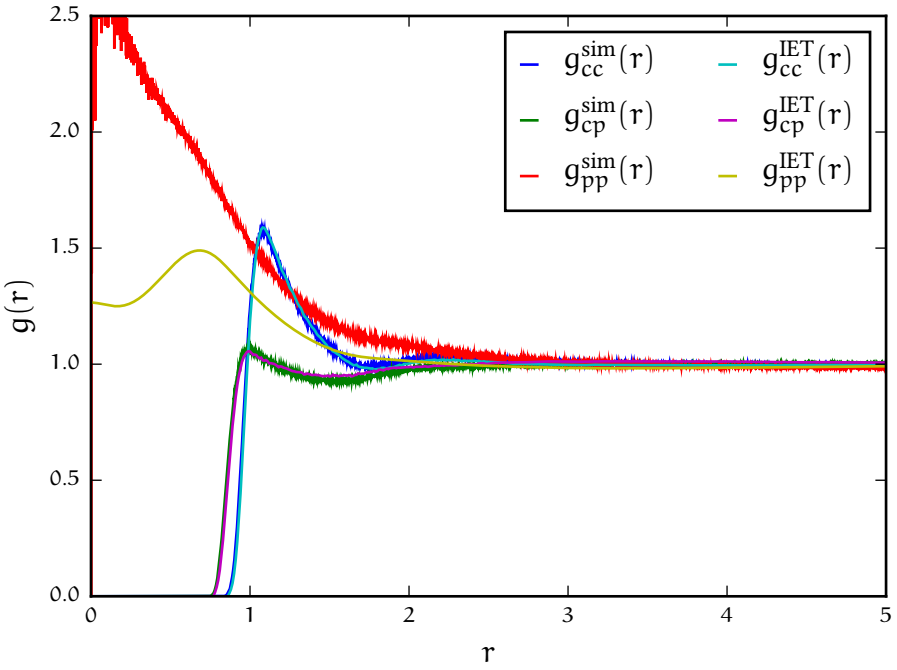

Figure A.2: The radial distribution function $g(r)$ for a state point with $\eta_{col} = 0.15$ and $\eta_{pol} = 0.05$ as measured by simulating the active system (sim) and as estimated by IET calculations (IET) for the colloid-colloid (cc), colloid-polymer (cp) and polymer-polymer (pp) interaction.

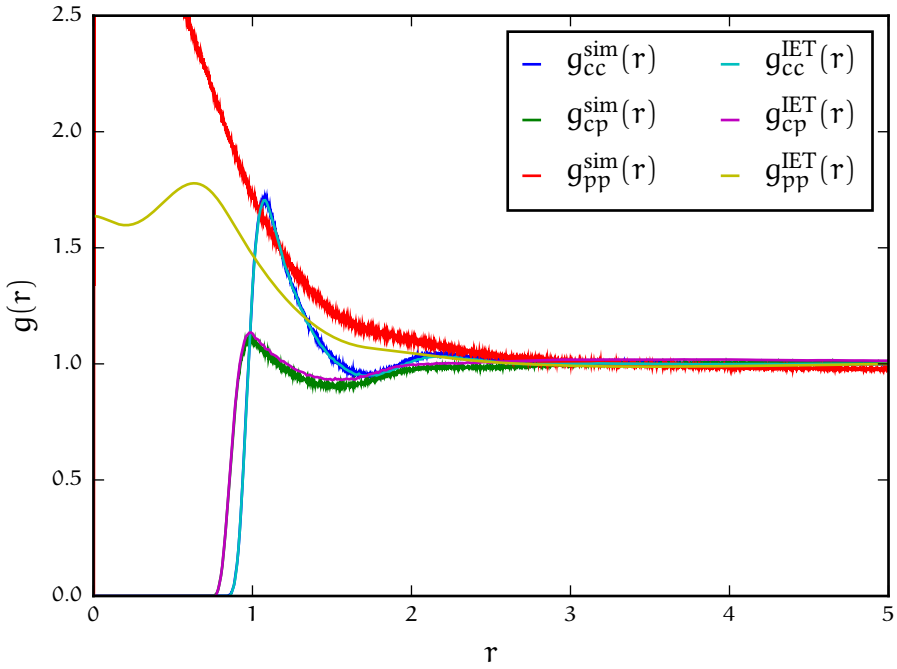

Figure A.3: The radial distribution function $g(r)$ for a state point with $\eta_{col} = 0.20$ and $\eta_{pol} = 0.05$ as measured by simulating the active system (sim) and as estimated by IET calculations (IET) for the colloid-colloid (cc), colloid-polymer (cp) and polymer-polymer (pp) interaction.

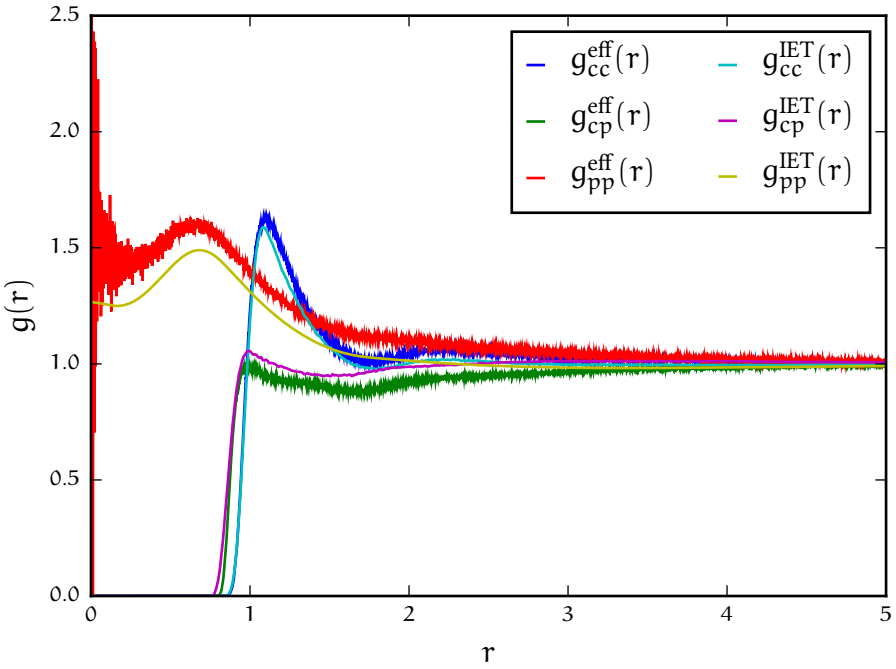

Figure A.4: The radial distribution function $g(r)$ for a state point with $\eta_{col} = 0.15$ and $\eta_{pol} = 0.05$ as measured by simulating with the effective potentials (eff) and the active model (sim) for the colloid-colloid (cc), colloid-polymer (cp) and polymer-polymer (pp) interaction.

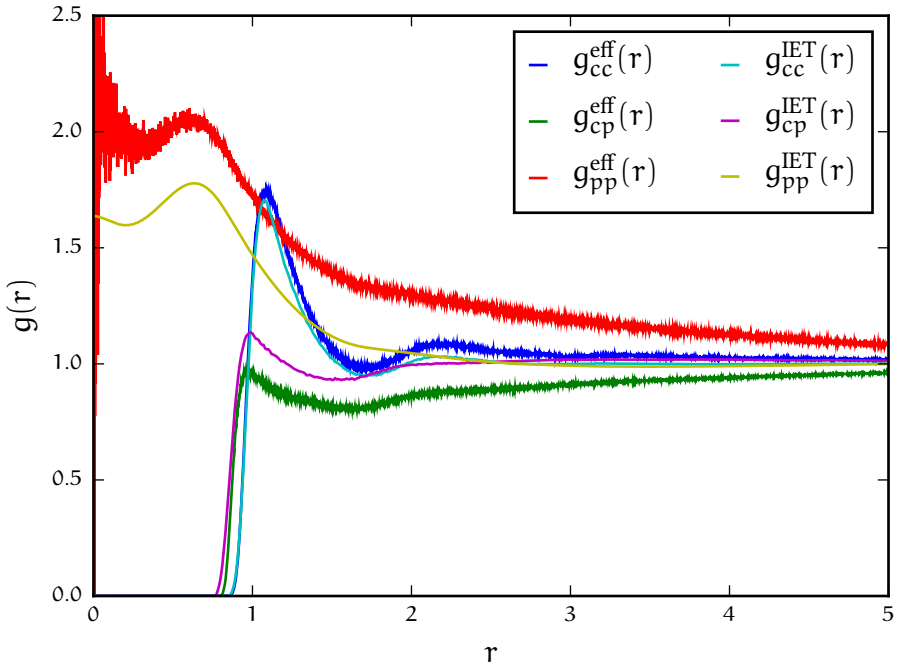

Figure A.5: The radial distribution function $g(r)$ for a state point with $\eta_{col} = 0.20$ and $\eta_{pol} = 0.05$ as measured by simulating with the effective potentials (eff) and the active model (sim) for the colloid-colloid (cc), colloid-polymer (cp) and polymer-polymer (pp) interaction.

BIBLIOGRAPHY

[1] B. Trefz, J. Siebert, and P. Virnau, "How molecular knots can pass through each other", Proceedings of the National Academy of Sciences **111**, 7948 (2014).

[2] S. K. Das, S. A. Egorov, B. Trefz, P. Virnau, and K. Binder, "Phase Behavior of Active Swimmers in Depletants: Molecular Dynamics and Integral Equation Theory", Phys. Rev. Lett. **112**, 198301 (2014).

[3] B. Trefz and P. Virnau, "Scaling behavior of topologically constrained polymer rings in a melt", Journal of Physics: Condensed Matter **27**, 354110 (2015).

[4] B. Trefz, S. K. Das, S. A. Egorov, P. Virnau, and K. Binder, "Activity mediated phase separation: Can we understand phase behavior of the nonequilibrium problem from an equilibrium approach?", The Journal of Chemical Physics **144**, 144902 (2016).

[5] H. Nishimori and G. Ortiz, *Elements of phase transitions and critical phenomena* (OUP Oxford, 2010).

[6] H. E. Stanley, *Introduction to Phase Transitions and Critical Phenomena* (Oxford University Press, 1987).

[7] O. G. Mouritsen, *Computer studies of phase transitions and critical phenomena* (Springer Berlin etc., 1984).

[8] N. Vandewalle, P. Boveroux, A. Minguet, and M. Ausloos, "The crash of October 1987 seen as a phase transition: amplitude and universality", Physica A: Statistical Mechanics and its Applications **255**, 201 (1998).

[9] M. Levy, "Social phase transitions", Journal of Economic Behavior & Organization **57**, 71 (2005).

[10] M. Ballerini, N. Cabibbo, R. Candelier, A. Cavagna, E. Cisbani, I. Giardina, V. Lecomte, A. Orlandi, G. Parisi, A. Procaccini, et al., "Interaction ruling animal collective behavior depends on topological rather than metric distance: Evidence from a field study", Proceedings of the national academy of sciences **105**, 1232 (2008).

[11] Y. Katz, K. Tunstrøm, C. C. Ioannou, C. Huepe, and I. D. Couzin, "Inferring the structure and dynamics of interactions in schooling fish", Proceedings of the National Academy of Sciences **108**, 18720 (2011).

[12] A. Bricard, J.-B. Caussin, N. Desreumaux, O. Dauchot, and D. Bartolo, "Emergence of macroscopic directed motion in populations of motile colloids", Nature **503**, 95 (2013).

[13] G. Quincke, "Ueber rotationen im constanten electrischen felde", Annalen der Physik **295**, 417 (1896).

[14] V. Narayan, N. Menon, and S. Ramaswamy, "Nonequilibrium steady states in a vibrated-rod monolayer: tetratic, nematic, and smectic correlations", Journal of Statistical Mechanics: Theory and Experiment **2006**, P01005 (2006).

[15] J. Deseigne, O. Dauchot, and H. Chaté, "Collective Motion of Vibrated Polar Disks", Phys. Rev. Lett. **105**, 098001 (2010).

[16] M. Ibele, T. E. Mallouk, and A. Sen, "Schooling Behavior of Light-Powered Autonomous Micromotors in Water", Angewandte Chemie **121**, 3358 (2009).

[17] V. Schaller, C. Weber, C. Semmrich, E. Frey, and A. R. Bausch, "Polar patterns of driven filaments", Nature **467**, 73 (2010).

[18] Y. Sumino, K. H. Nagai, Y. Shitaka, D. Tanaka, K. Yoshikawa, H. Chaté, and K. Oiwa, "Large-scale vortex lattice emerging from collectively moving microtubules", Nature **483**, 448 (2012).

[19] M. E. Cates, D. Marenduzzo, I. Pagonabarraga, and J. Tailleur, "Arrested phase separation in reproducing bacteria creates a generic route to pattern formation", Proceedings of the National Academy of Sciences **107**, 11715 (2010).

[20] H. P. Zhang, A. Be'er, E.-. L. Florin, and H. L. Swinney, "Collective motion and density fluctuations in bacterial colonies", Proceedings of the National Academy of Sciences **107**, 13626 (2010).

[21] R. Dreyfus, J. Baudry, M. L. Roper, M. Fermigier, H. A. Stone, and J. Bibette, "Microscopic artificial swimmers", Nature **437**, 862 (2005).

[22] H.-R. Jiang, N. Yoshinaga, and M. Sano, "Active Motion of a Janus Particle by Self-Thermophoresis in a Defocused Laser Beam", Phys. Rev. Lett. **105**, 268302 (2010).

[23] I. Buttinoni, G. Volpe, F. Kümmel, G. Volpe, and C. Bechinger, "Active Brownian motion tunable by light", Journal of Physics: Condensed Matter **24**, 284129 (2012).

[24] J. Palacci, S. Sacanna, A. P. Steinberg, D. J. Pine, and P. M. Chaikin, "Living Crystals of Light-Activated Colloidal Surfers", Science **339**, 936 (2013).

[25] J. R. Howse, R. A. L. Jones, A. J. Ryan, T. Gough, R. Vafabakhsh, and R. Golestanian, "Self-Motile Colloidal Particles: From Directed Propulsion to Random Walk", Phys. Rev. Lett. **99**, 048102 (2007).

[26] H. Ke, S. Ye, R. L. Carroll, and K. Showalter, "Motion Analysis of Self-Propelled Pt-Silica Particles in Hydrogen Peroxide Solutions", J. Phys. Chem. A **114**, 5462 (2010).

[27] J. Palacci, C. Cottin-Bizonne, C. Ybert, and L. Bocquet, "Sedimentation and Effective Temperature of Active Colloidal Suspensions", Phys. Rev. Lett. **105**, 088304 (2010).

[28] T. Vicsek, A. Czirók, E. Ben-Jacob, I. Cohen, and O. Shochet, "Novel Type of Phase Transition in a System of Self-Driven Particles", Phys. Rev. Lett. **75**, 1226 (1995).

[29] J. Bialké, T. Speck, and H. Löwen, "Crystallization in a Dense Suspension of Self-Propelled Particles", Phys. Rev. Lett. **108**, 168301 (2012).

[30] F. D. C. Farrell, M. C. Marchetti, D. Marenduzzo, and J. Tailleur, "Pattern Formation in Self-Propelled Particles with Density-Dependent Motility", Phys. Rev. Lett. **108**, 248101 (2012).

[31] Julian Bialké and Thomas Speck and Hartmut Löwen, "Active colloidal suspensions: Clustering and phase behavior", Journal of Non-Crystalline Solids **407**, 7th IDMRCS: Relaxation in Complex Systems, 367 (2015).

[32] D. Grossman, I. S. Aranson, and E. B. Jacob, "Emergence of agent swarm migration and vortex formation through inelastic collisions", New Journal of Physics **10**, 023036 (2008).

[33] M. E. Cates and J. Tailleur, "Motility-Induced Phase Separation", Annu. Rev. Condens. Matter Phys. **6**, 219 (2015).

[34] S. Wang and P. G. Wolynes, "Communication: Effective temperature and glassy dynamics of active matter", The Journal of Chemical Physics **135**, 051101 (2011).

[35] D. Loi, S. Mossa, and L. F. Cugliandolo, "Effective temperature of active complex matter", Soft Matter **7**, 3726 (2011).

[36] D. Frenkel and B. Smit, *Understanding molecular simulation: from algorithms to applications*, Vol. 1 (Academic press, 2001).

[37] D. P. Landau and K. Binder, *A guide to Monte Carlo simulations in statistical physics* (Cambridge university press, 2014).

[38] L. Onsager, "Crystal Statistics. I. A Two-Dimensional Model with an Order-Disorder Transition", Phys. Rev. **65**, 117 (1944).

[39] M. Hasenbusch, "Finite size scaling study of lattice models in the three-dimensional Ising universality class", Phys. Rev. B **82**, 174433 (2010).

[40] M. E. Fisher, "The renormalization group in the theory of critical behavior", Rev. Mod. Phys. **46**, 597 (1974).

[41] K. Binder, "Finite size scaling analysis of Ising model block distribution functions", Zeitschrift für Physik B Condensed Matter **43**, 119 (1981).

[42] S. Asakura and F. Oosawa, "Interaction between particles suspended in solutions of macromolecules", Journal of Polymer Science **33**, 183 (1958).

[43] J. Zausch, P. Virnau, K. Binder, J. Horbach, and R. L. Vink, "Statics and dynamics of colloid-polymer mixtures near their critical point of phase separation: A computer simulation study of a continuous Asakura-Oosawa model", The Journal of Chemical Physics **130**, 064906 (2009).

[44] J. D. Weeks, "Role of Repulsive Forces in Determining the Equilibrium Structure of Simple Liquids", The Journal of Chemical Physics **54**, 5237 (1971).

[45] J. A. Barker and D. Henderson, "Perturbation Theory and Equation of State for Fluids. II. A Successful Theory of Liquids", The Journal of Chemical Physics **47**, 4714 (1967).

[46] H. N. W. Lekkerkerker, W. C.-K. Poon, P. N. Pusey, A. Stroobants, and P. B. Warren, "Phase Behaviour of Colloid + Polymer Mixtures", EPL (Europhysics Letters) **20**, 559 (1992).

[47] R. L. C. Vink and J. Horbach, "Grand canonical Monte Carlo simulation of a model colloid–polymer mixture: Coexistence line, critical behavior, and interfacial tension", The Journal of Chemical Physics **121**, 3253 (2004).

[48] R. L. C. Vink and J. Horbach, "Critical behaviour and interfacial fluctuations in a phase-separating model colloid–polymer mixture: grand canonical Monte Carlo simulations", Journal of Physics: Condensed Matter **16**, S3807 (2004).

[49] D. Deb, A. Winkler, P. Virnau, and K. Binder, "Simulation of fluid-solid coexistence in finite volumes: A method to study the properties of wall-attached crystalline nuclei", The Journal of chemical physics **136**, 134710 (2012).

[50] A. Brünger, C. L. Brooks, and M. Karplus, "Stochastic boundary conditions for molecular dynamics simulations of ST2 water", Chemical Physics Letters **105**, 495 (1984).

[51] T. Schlick, *Molecular modeling and simulation: an interdisciplinary guide*, Vol. 21 (Springer Science & Business Media, 2010).

[52] A. Czirók and T. Vicsek, "Collective behavior of interacting self-propelled particles", Physica A: Statistical Mechanics and its Applications **281**, 17 (2000).

[53] C. Valeriani, M. Li, J. Novosel, J. Arlt, and D. Marenduzzo, "Colloids in a bacterial bath: simulations and experiments", Soft Matter **7**, 5228 (2011).

[54] G. Gonnella, D. Marenduzzo, A. Suma, and A. Tiribocchi, "Motility-induced phase separation and coarsening in active matter", Comptes Rendus Physique **16**, 316 (2015).

[55] J. Schwarz-Linek, C. Valeriani, A. Cacciuto, M. E. Cates, D. Marenduzzo, A. N. Morozov, and W. C. K. Poon, "Phase separation and rotor self-assembly in active particle suspensions", Proceedings of the National Academy of Sciences **109**, 4052 (2012).

[56] U. Erdmann, W. Ebeling, and A. S. Mikhailov, "Noise-induced transition from translational to rotational motion of swarms", Phys. Rev. E **71**, 051904 (2005).

[57] M. P. Allen and D. J. Tildesley, *Computer Simulation of Liquids (Oxford Science Publications)*, Reprint, Oxford science publications (Oxford University Press, June 1989).

[58] O. G. Jepps, G. Ayton, and D. J. Evans, "Microscopic expressions for the thermodynamic temperature", Phys. Rev. E **62**, 4757 (2000).

[59] G. Ayton, O. G. Jepps, and D. J. Evans, "On the validity of Fourier's law in systems with spatially varying strain rates", Molecular Physics **96**, 915 (1999).

[60] C. P. Lowe, "An alternative approach to dissipative particle dynamics", Europhysics Letters (EPL) **47**, 145 (1999).

[61] C. Huang, A. Chatterji, G. Sutmann, G. Gompper, and R. Winkler, "Cell-level canonical sampling by velocity scaling for multiparticle collision dynamics simulations", Journal of Computational Physics **229**, 168 (2010).

[62] A. Malevanets and R. Kapral, "Solute molecular dynamics in a mesoscale solvent", The Journal of Chemical Physics **112**, 7260 (2000).

[63] H. J. Berendsen, J. P. M. Postma, W. F. van Gunsteren, A. DiNola, and J. Haak, "Molecular dynamics with coupling to an external bath", The Journal of chemical physics **81**, 3684 (1984).

[64] H. C. Andersen, "Molecular dynamics simulations at constant pressure and/or temperature", The Journal of chemical physics **72**, 2384 (1980).

[65] H. A. Posch, W. G. Hoover, and F. J. Vesely, "Canonical dynamics of the Nosé oscillator: Stability, order, and chaos", Phys. Rev. A **33**, 4253 (1986).

[66] T. Soddemann, B. Dünweg, and K. Kremer, "Dissipative particle dynamics: A useful thermostat for equilibrium and nonequilibrium molecular dynamics simulations", Phys. Rev. E **68**, 046702 (2003).

[67] V. Lobaskin and M. Romenskyy, "Collective dynamics in systems of active Brownian particles with dissipative interactions", Physical Review E **87**, 052135 (2013).

[68] A. Zöttl and H. Stark, "Hydrodynamics Determines Collective Motion and Phase Behavior of Active Colloids in Quasi-Two-Dimensional Confinement", Phys. Rev. Lett. **112**, 118101 (2014).

[69] D. Richard and T. Speck, "The role of shear in crystallization kinetics: From suppression to enhancement", Scientific Reports **5**, 14610 (2015).

[70] A. Wysocki, R. G. Winkler, and G. Gompper, "Cooperative motion of active Brownian spheres in three-dimensional dense suspensions", EPL (Europhysics Letters) **105**, 48004 (2014).

[71] A. P. Solon, J. Stenhammar, R. Wittkowski, M. Kardar, Y. Kafri, M. E. Cates, and J. Tailleur, "Pressure and Phase Equilibria in Interacting Active Brownian Spheres", Phys. Rev. Lett. **114**, 198301 (2015).

[72] J. Bialké, J. T. Siebert, H. Löwen, and T. Speck, "Negative Interfacial Tension in Phase-Separated Active Brownian Particles", Phys. Rev. Lett. **115**, 098301 (2015).

[73] S. C. Harvey, R. K.-Z. Tan, and T. E. Cheatham, "The flying ice cube: Velocity rescaling in molecular dynamics leads to violation of energy equipartition", Journal of Computational Chemistry **19**, 726 (1998).

[74] G. S. Redner, A. Baskaran, and M. F. Hagan, "Reentrant phase behavior in active colloids with attraction", Physical Review E **88**, 012305 (2013).

[75] J. P. Hansen and I. R. McDonald, "Theory of simple liquids", (1986).

[76] H. Frisch and J. Lebowitz, *The Equilibrium Theory of Classical Fluids: A Lecture Note and Reprint Volume*, Frontiers in Physics: Lecture note and reprint series, A (W.A. Benjamin, 1964).

[77] J. K. Percus and G. J. Yevick, "Analysis of Classical Statistical Mechanics by Means of Collective Coordinates", Phys. Rev. **110**, 1 (1958).

[78] Y. Rosenfeld and N. W. Ashcroft, "Theory of simple classical fluids: Universality in the short-range structure", Phys. Rev. A **20**, 1208 (1979).

[79] D. Reith, M. Pütz, and F. Müller-Plathe, "Deriving effective mesoscale potentials from atomistic simulations", Journal of computational chemistry **24**, 1624 (2003).

[80] T. C. Moore, C. R. Iacovella, and C. McCabe, "Derivation of coarse-grained potentials via multistate iterative Boltzmann inversion", The Journal of Chemical Physics **140**, 224104 (2014).

[81] F. J. Rogers and D. A. Young, "New, thermodynamically consistent, integral equation for simple fluids", Phys. Rev. A **30**, 999 (1984).

[82] K. Kaski, K. Binder, and J. D. Gunton, "Study of cell distribution functions of the three-dimensional Ising model", Phys. Rev. B **29**, 3996 (1984).

[83] M. Rovere, D. W. Hermann, and K. Binder, "Block Density Distribution Function Analysis of Two-Dimensional Lennard-Jones Fluids", Europhysics Letters (EPL) **6**, 585 (1988).

[84] M. Rovere, P. Nielaba, and K. Binder, "Simulation studies of gas-liquid transitions in two dimensions via a subsystem-block-density distribution analysis", Z. Physik B - Condensed Matter **90**, 215 (1993).

[85] H. Watanabe, N. Ito, and C.-K. Hu, "Phase diagram and universality of the Lennard-Jones gas-liquid system", The Journal of Chemical Physics **136**, 204102 (2012).

[86] P. Virnau, "Monte-Carlo-Simulationen zum Phasen- und Keimbildungsverhalten von Polymerlösungen", PhD thesis (Johannes Gutenberg University Mainz, 2003).

[87] W. Selke, "Critical Binder cumulant of two-dimensional Ising models", The European Physical Journal B-Condensed Matter and Complex Systems **51**, 223 (2006).

[88] Y. C. Kim, M. E. Fisher, and E. Luijten, "Precise Simulation of Near-Critical Fluid Coexistence", Phys. Rev. Lett. **91**, 065701 (2003).

[89] A. Onuki and K. Kawasaki, "Nonequilibrium steady state of critical fluids under shear flow: A renormalization group approach", Annals of Physics **121**, 456 (1979).

[90] D. Beysens, M. Gbadamassi, and B. Moncef-Bouanz, "New developments in the study of binary fluids under shear flow", Phys. Rev. A **28**, 2491 (1983).

[91] A. Czirók, H. E. Stanley, and T. Vicsek, "Spontaneously ordered motion of self-propelled particles", Journal of Physics A: Mathematical and General **30**, 1375 (1997).

[92] G. Grégoire and H. Chaté, "Onset of Collective and Cohesive Motion", Phys. Rev. Lett. **92**, 025702 (2004).

[93] M. Nagy, I. Daruka, and T. Vicsek, "New aspects of the continuous phase transition in the scalar noise model (SNM) of collective motion", Physica A: Statistical Mechanics and its Applications **373**, 445 (2007).

[94] M. Aldana, V. Dossetti, C. Huepe, V. M. Kenkre, and H. Larralde, "Phase Transitions in Systems of Self-Propelled Agents and Related Network Models", Phys. Rev. Lett. **98**, 095702 (2007).

[95] A. P. Solon and J. Tailleur, "Flocking with discrete symmetry: The two-dimensional active Ising model", Phys. Rev. E **92**, 042119 (2015).

[96] R. L. C. Vink, J. Horbach, and K. Binder, "Critical phenomena in colloid-polymer mixtures: Interfacial tension, order parameter, susceptibility, and coexistence diameter", Phys. Rev. E **71**, 011401 (2005).

[97] K. Binder and D. P. Landau, "Finite-size scaling at first-order phase transitions", Phys. Rev. B **30**, 1477 (1984).

[98] G. Orkoulas, M. E. Fisher, and A. Z. Panagiotopoulos, "Precise simulation of criticality in asymmetric fluids", Phys. Rev. E **63**, 051507 (2001).

[99] Y. C. Kim, M. E. Fisher, and G. Orkoulas, "Asymmetric fluid criticality. I. Scaling with pressure mixing", Phys. Rev. E **67**, 061506 (2003).

[100] S. Ramaswamy, R. A. Simha, and J. Toner, "Active nematics on a substrate: Giant number fluctuations and long-time tails", EPL (Europhysics Letters) **62**, 196 (2003).

[101] H. Chaté, F. Ginelli, and R. Montagne, "Simple Model for Active Nematics: Quasi-Long-Range Order and Giant Fluctuations", Phys. Rev. Lett. **96**, 180602 (2006).

[102] F. Peruani, J. Starruß, V. Jakovljevic, L. Søgaard-Andersen, A. Deutsch, and M. Bär, "Collective Motion and Nonequilibrium Cluster Formation in Colonies of Gliding Bacteria", Phys. Rev. Lett. **108**, 098102 (2012).

[103] J. Toner and Y. Tu, "Long-Range Order in a Two-Dimensional Dynamical XY Model: How Birds Fly Together", Phys. Rev. Lett. **75**, 4326 (1995).

[104] J. Toner and Y. Tu, "Flocks, herds, and schools: A quantitative theory of flocking", Phys. Rev. E **58**, 4828 (1998).

[105] Y. Tu, J. Toner, and M. Ulm, "Sound Waves and the Absence of Galilean Invariance in Flocks", Phys. Rev. Lett. **80**, 4819 (1998).

[106] G. Baglietto and E. V. Albano, "Finite-size scaling analysis and dynamic study of the critical behavior of a model for the collective displacement of self-driven individuals", Physical Review E **78**, 021125 (2008).

[107] G. Baglietto and E. V. Albano, "Computer simulations of the collective displacement of self-propelled agents", Computer Physics Communications **180**, 527 (2009).

[108] A. L. Talapov and H. W. J. Blöte, "The magnetization of the 3D Ising model", Journal of Physics A: Mathematical and General **29**, 5727 (1996).

[109] R. L. C. Vink, K. Binder, and J. Horbach, "Critical behavior of a colloid-polymer mixture confined between walls", Phys. Rev. E **73**, 056118 (2006).

[110] M. Rossi, R. Pastor-Satorras, and A. Vespignani, "Universality Class of Absorbing Phase Transitions with a Conserved Field", Phys. Rev. Lett. **85**, 1803 (2000).